INVESTIGATION OF POOL BOILING HEAT TRANSFER FROM ROUGH SURFACE AND MICROCHANNEL GEOMETRY UNDER VARIABLE HEAT SUPPLY

Thesis

Submitted in partial fulfillment of the requirements for the Degree of

DOCTOR OF PHILOSOPHY

by

WALUNJ AVDHOOT ASHOK

(ME15F18)

DEPARTMENT OF MECHANICAL ENGINEERING

NATIONAL INSTITUTE OF TECHNOLOGY KARNATAKA

SURATHKAL, MANGALURU – 575025

JANUARY, 2019

INVESTIGATION OF POOL BOILING HEAT TRANSFER FROM ROUGH SURFACE AND MICROCHANNEL GEOMETRY UNDER VARIABLE HEAT SUPPLY

Thesis

Submitted in partial fulfillment of the requirements for the degree of

DOCTOR OF PHILOSOPHY

By

WALUNJ AVDHOOT ASHOK

(ME15F18)

Under the guidance of

Dr. (Mrs.) A. SATHYABHAMA

Associate Professor

DEPARTMENT OF MECHANICAL ENGINEERING

NATIONAL INSTITUTE OF TECHNOLOGY KARNATAKA

SURATHKAL, MANGALURU – 575025

JANUARY, 2019

D E C L A R A T I O N

by the Ph.D. Research Scholar

I hereby *declare* that the Research Thesis entitled **'Investigation of Pool Boiling Heat Transfer from Rough Surface and Microchannel Geometry Under Variable Heat Supply'** which is being submitted to the National Institute of Technology Karnataka, Surathkal in partial fulfillment of the requirements for the award of the Degree of Doctor of Philosophy in **Mechanical Engineering** is a *bonafide report of the research work carried out by me*. The material contained in this Research Thesis has not been submitted to any University or Institution for the award of any degree.

Mr. Walunj Avdhoot Ashok

Register Number- 155043ME15F18

(Name & Signature of the Research Scholar)

Department of Mechanical Engineering

Place: NITK-Surathkal
Date: 01/01/2019

C E R T I F I C A T E

This is to certify that the Research Thesis entitled **'Investigation of Pool Boiling Heat Transfer from Rough Surface and Microchannel Geometry Under Variable Heat Supply'** submitted by **Mr. Walunj Avdhoot Ashok**, (Register Number: **155043ME15F18**) as the record of the research work carried out by him, is accepted as the *Research Thesis submission* in partial fulfillment of the requirements for the award of degree of **Doctor of Philosophy.**

Dr. (Mrs.) A. Sathyabhama
Research Guide
Date:

Dr. Narendranath S.
Chairman- DRPC
Date:

A C K N O W L E D G E M E N T

I take this opportunity to thank all the people who have guided, supported and encouraged me to complete my research work.

Indeed the words of my command are not adequate to convey the deep sense of gratitude to my supervisor **Dr. A. Sathyabhama** for her unwavering support, collegiality, mentorship, magnanimous attitude right from the first day, constant encouragement, enormous help and constructive criticism throughout my research work. For generous guidance and useful suggestions, special thanks are tendered to my committee members **Dr. M. R. Ramesh** and **Dr. Nagendrappa H.** I am also thankful to **Dr. K. V. Gangadharan**, former Head of Mechanical Department and **Dr. Narendranath S.**, Professor and Head, Department of Mechanical Engineering for their support.

I express my heartfelt gratitude to my colleagues Suhas, Sreejith, Anil, Harsha, Tipeshswamy, Hargovind, Balu, Madhu, Jayapal and Raghavendra for furnishing necessary aids and for their co-operation throughout the period of research work. As thank and appreciation does not value in friendship, I would just remember Narendran, Vishweshwara and Kiran, the dynamic and empathetic personalities I ever met.

To My Family

ABSTRACT

Enormous amount of heat is generated in the Economic Simplified Boiling Water Reactor (ESBWR) due to exponential heat generation from the fuel rod. A core melt accident occurs when the heat generated in the nuclear reactor exceeds the heat removed by the coolant to the point where at least one nuclear fuel element exceeds its melting point temperature. Critical Heat Flux (CHF) is the phase of boiling after which heat transfer coefficient drops resulting in the rapid increase in temperature of core. Hence, understanding the mechanism of CHF is important to control loss of coolant accident (LOCA). CHF enhancement may retard the LOCA in ESBWR. Passive enhancement techniques are the most suitable for the nuclear reactor application. In view of the facts discussed above, the CHF enhancement by two passive techniques namely, rough surfaces and microchannel geometries is investigated. The transient CHF enhancement is compared with the steady-state CHF upto 10 bar pressure.

The experimental setup is designed to study the pool boiling of water at 1 bar, 5 bar and 10 bar pressures. The pool boiling experiments are conducted on the thick copper sample of 20 mm diameter at saturated condition of distilled water. The unidirectional scratches are made on the sample to obtain wide range of surface roughness varying from R_a=0.106 μm to R_a=4.03 μm. It is found that steady-state CHF increases with increase in the R_a. Improved wettability and increased nucleation site density resulted in the CHF enhancement by rough surface. The microchannel geometries namely, square (SM-1.0), parabolic (PM-1.6) and stepped (SM-1.6) were fabricated by VMC machining. The improved liquid supply through the channel space and significant bubble growth resulted in the CHF enhancement by the microchannel geometry. The CHF enhancement by SM-1.6 is highest among all the microchannel geometries.

The experimental setup is commissioned with programmable power supply to compare the CHF of water during pool boiling on rough surface and microchannel geometry under steady-state and exponential heat supply. The time constant (γ) of exponential heat supply is varied from 1 to 6. It is found that both, rough surfaces and microchannel geometries enhance the transient CHF. However, transient CHF gradually decreased

with increase in γ due to liquid-vapor instability during exponential heat supply. CHF increased with increase in the pressure at both the condition viz. steady and transient. Steady-state CHF for R_a=4.03 μm and SM-1.6 at P=10 bar is found to be 71.43% and 47.37% higher compared to the CHF at P=1 bar, respectively.

The correlation for heat transfer coefficient is developed for prediction of transient boiling performance which includes the non-dimensional time constant γ. Present correlation predicts the experimental values of transient HTC with MAE of 14.91%. CHF model for rough surface, based on force balance approach, is developed incorporating the effect of time constant, bubble angle and roughness parameter viz. R_a, S_m to predict the boiling crisis during pool boiling. It predicts the experimental transient CHF with MAE of 11.89%.

Boiling videos are recorded at 1000 fps using high speed camera during the experiments to study the bubble dynamics during pool boiling on rough surface and microchannel geometries upto 10 bar pressure. Bubble dynamics during pool boiling of saturated water is significantly affected by the surface characteristics i.e. surface roughness and microchannel. Prolonged nucleated boiling regime is noticed for rough surface at high pressure due to the capillary wicking in the unidirectional scratches which retards the horizontal coalescence. Forces acting vertically on the growing bubble are considered to predict the bubble departure diameter. The MAE between measured and predicted bubble departure diameter for the rough surface and microchannel geometries at all pressure is 17.09% and 13.30%, respectively.

Keywords: critical heat flux, heat transfer coefficient, wettability, capillary wicking, bubble dynamics

LIST OF CONTENT

LIST OF TABLE……..……. v

LIST OF FIGURE……..…….…….. vi

NOMENCLATURE……..……. xiii

1 INTRODUCTION……...…….……01

1.1 BACKGROUND……...…….……01

1.2 CORE MELT ACCIDENT.....02

1.3 TRANSIENT POOL BOILING HEAT TRANSFER.....03

1.4 HEAT TRANSFER ENHANCEMENT TECHNIQUE.....04

1.5 PASSIVE TECHNIQUES FOR POOL BOILING HEAT TRANSFER ENHANCEMENT……..…….…….05

1.6 ORGANIZATION OF THE THESIS……...…….07

2 LITERATURE REVIEW……...……..09

2.1 POOL BOILING ON MICROCHANNEL GEOMETRY……..……..…..09

2.2 POOL BOILING ON ROUGH SURFACE……...…….….13

2.3 TRANSIENT POOL BOILING HEAT TRANSFER……....…….17

2.4 CHF MODEL……..21

2.5 BUBBLE DYNAMICS……..……...……..22

2.6 NEED FOR FURTHER RESEARCH……..…..……23

2.7 OBJECTIVES OF THE PRESENT RESEARCH WORK……..…….25

3 EXPERIMENTATION……...…….....27

3.1 PREPARATION OF TEST SAMPLES …….27

3.2 CHARACTERIZATION…….……...…….……...27

3.3 EXPERIMENTAL SETUP……..……..……30

3.4 TEST SECTION…….……...……31

3.5 EXPERIMENTAL PROCEDURE……..….….…….…...…33

3.6 DATA REDUCTION……...……..……...…35

3.7 VISUALIZATION OF BOILING…….……....36

3.8 UNCERTAINTY…….……..…..….....38

3.9 REPEATABILITY……..…….…….……39

3.10 HYSTERESIS…….…….....…….40

4 RESULTS AND DISCUSSION...……..……..……41

4.1 SELECTION OF ROUGHNESS PARAMETER…….…….....……41

4.2 EFFECT OF UNIDIRECTIONAL SCRATCHES ON THE WETTABILITY…….……...42

4.3 VALIDATION OF EXPERIMENTAL RESULTS……..…….44

4.4 EFFECT OF STATE OF HEATING ON POOL BOILING HEAT TRANSFER…….…….....47

4.5 EFFECT OF SURFACE MODIFICATION ON POOL BOILING HEAT TRANSFER……..……...…..……48

4.6 EFFECT OF TIME CONSTANT ON TRANSIENT POOL BOILING HEAT TRANSFER……...……52

4.7 EFFECT OF PRESSURE ON POOL BOILING HEAT TRANSFER……...53

4.8 ONSET OF NUCLEATE BOILING AND OVERSHOOT TEMPERATURE ……...55

4.9 VARIATION IN TRANSIENT HTC WITH TRANSIENT HEAT FLUX ……...59

4.10 CRITICAL HEAT FLUX…….……. 61

4.11 TRANSIENT MAXIMUM HEAT TRANSFER COEFFICIENT…….66

5 CHF MODEL……...……73

5.1 PRESENT MODEL……...…….75

6 BUBBLE DYNAMICS……..…….....83

6.1 VISUALIZATION OF POOL BOILING ON MICROCHANNEL GEOMETRIES……...……..83

6.1.1 Mechanism of bubble growth……...……83

6.1.2 Effect of microchannel profile on bubble departure diameter…..…...86

6.1.3 Effect of microchannel profile on bubble frequency……...….87

6.2 MODELING OF BUBBLE DEPARTURE DIAMETER……...…….88

6.2.1 Force Balance……..…….88

6.2.2 Verification of the model……..……...91

6.3 VISUALIZATION POOL BOILING ON ROUGH SURFACE……...92

6.3.1 Mechanism of bubble growth……..…….....92

6.3.2 Bubble departure diameter……..……94

6.3.3 Correlation for bubble departure diameter……..…….…....98

6.3.4 Bubble frequency……..……...…..…...101

6.3.5 Correlation for bubble frequency…….……...……..103

7 CONCLUSION AND SCOPE FOR FUTURE WORK……..…….109

7.1 CONCLUSIONS……...……..…....109

7.2 SCOPE FOR FUTURE WORK……111

REFERENCES……..…….113

APPENDIX A: UNCERTAINTY……..…….……...……...123

APPENDIX B: POOL BOILING HEAT TRANSFER FROM ROUGH SURFACE AND MICROCHANNEL GEOMETRY……..……...…….125

B.1 VALIDATION OF EXPERIMENTAL RESULTS……...…….125

B.2 POOL BOILING CURVE FOR ROUGH SURFACE AND MICROCHANNEL GEOMETRY……...…….….……127

B.3 TRANSIENT POOL BOILING HEAT TRANSFER COEFFICIENT FOR ROUGH SURFACE……..……..…….140

B.4 TRANSIENT CRITICAL HEAT FLUX…….……..…….147

PUBLICATION……..……...…….....149

BIO-DATA……..……...…….151

LIST OF TABLE

Table No.	Title of Table	Page No.
2.1	Details of the studies available in the literature related to microchannel geometries	12
2.2	Details of the studies available in the literature related to rough surface	16
2.3	Summary of the experimental conditions used in the literature during transient pool boiling studies	20
3.1	Roughness parameters in μm	28
3.2	Dimensions of microchannel geometries	30
3.3	Operating conditions in the present experiment	32
3.4	Instruments and equipment used in the present experiment	33
4.1	Existing correlation for HTC	44
4.2	Comparison between experimental and predicted HTC	45
6.1	Bubble growth study at q=160-175 kW/m^2	84
6.2	Boiling phases for R_a=4.03 μm at different pressures	93
6.3	MAE between predicted and measured bubble departure diameter	98
A.1	Uncertainty values for heat flux, HTC and surface temperature of the test sample of R_a=4.03 μm at 10 bar pressure	123
A.2	Uncertainty in the measurement of bubble departure diameter and bubble frequency for the sample of R_a=4.03 μm at 10 bar pressure	124

LIST OF FIGURE

Fig. No.	Title of Figure	Page No.
1.1	ESBWR core design	02
1.2	Pool boiling curve	04
1.3	Passive techniques for pool boiling heat transfer enhancement	06
3.1	Unidirectional scratches on the samples	28
3.2	Contact angle measurement	29
3.3	Microchannel geometries	30
3.4	Schematic diagram of experimental setup	31
3.5	Test Section	32
3.6	Temperature distribution along the length of sample	36
3.7	Measurement of bubble departure diameter	37
3.8	Repeatability of the experimental data	39
3.9	Hysteresis	40
4.1	Variation of static contact angle with R_a	42
4.2	Contact angle measurement for the sample of R_a=3.17 μm	43
4.3	SEM of the polished surfaces after boiling	43
4.4	Validation of experimental results of R_a=0.106 μm at P=10 bar	45
4.5	Validation of experimental results of R_a=3.17 μm at P=5 bar	46
4.6	Boiling curves at steady-state heat supply, quasi-steady (γ=1) and rapid (γ=6) exponential heat supply	47
4.7	Effect of surface roughness on pool boiling heat transfer during steady-state heat supply	49
4.8	Effect of surface roughness on pool boiling heat transfer during exponential heat supply	50
4.9	Boiling curve of microchannel geometries during steady-state heat supply	51
4.10	Boiling curve of microchannel geometries during exponential heat supply	51
4.11	Boiling curves of the sample of R_a=1.87 μm at P=1 bar for different γ	52

Fig. No.	Title of Figure	Page No.
4.12	Boiling curves of SM-1.6 at P=5 bar for different γ	53
4.13	Boiling curves of the sample R_a=0.106 μm at (a) steady-state and (b) γ=1 at different pressures	55
4.14	Influence of state of heating on ONB temperature	56
4.15	Variation in ΔT_{onb} with γ and R_a at P=1 bar	57
4.16	Time trace of the surface temperature of R_a=3.17 μm at P=1 bar	58
4.17	Variation in $q''_{ONB,ts}$ with γ	58
4.18	Variation in non-dimensional h_{ts} with non-dimensional q_{ts} for different surface roughness at (a) P=1 bar, γ=3 (b) P=5 bar, γ=5 (c) P=10 bar, γ=2	60
4.19	Steady-state CHF of rough and microchannel geometries as function of pressure	62
4.20	Effect of time constant on transient CHF of rough and microchannel geometries at 5 bar pressure	63
4.21	Effect of surface roughness on steady and transient CHF at various pressures	64
4.22	Variation in transient CHF with pressure at different surface roughness	65
4.23	Contour plot of CHF for normalized R_a, γ and P	66
4.24	Effect of surface roughness on transient HTC at different time constant and pressure	67
4.25	Contour plot of h_{max} for normalized R_a, γ and P	68
4.26	Comparison of CHF predicted by Equation (4.3) with the experimental CHF at steady-state heat supply	68
4.27	Comparison of CHF predicted by Equation (4.5) with the experimental CHF at exponential heat supply	69
4.28	Comparison of HTC predicted by Equation (4.6) with the experimental HTC at exponential heat supply	70

Fig. No.	Title of Figure	Page No.
4.29	Comparison of transient HTC predicted by Equation (4.7) with the experimental HTC	71
5.1	Variation in CHF with pressure	74
5.2	Comparison of CHF predicted by model of Kim et al. (2016) with present experimental CHF	74
5.3	Schematic representation of bubble angle measurement	75
5.4	Variation in bubble angle with R_a at different pressure	76
5.5	Forces acting on the bubble parallel to the surface	77
5.6	Comparison of CHF predicted by modified Kim's model with present experimental CHF at steady-state condition	80
5.7	Comparison of experimental and predicted CHF	81
6.1	Schematic diagram of different channel profile	85
6.2	Proposed mechanism of (a) bubble growth and (b) liquid supply in the microchannel	85
6.3	Variation of bubble departure diameter with Jakob number	86
6.4	Variation of bubble frequency with Jakob number	87
6.5	Bubble growth in square microchannel	90
6.6	Comparison of bubble departure diameter of Chip 2 and 9 (Cooke and Kandlikar, 2012) with the present model	91
6.7	Comparison of predicted and experimental bubble departure diameter of microchannel geometries	92
6.8	Liquid supply through unidirectional scratches	94
6.9	Variation in the bubble departure diameter with Jakob number at (a) P=5 bar (b) P=10 bar	95
6.10	Variation in the predicted bubble departure diameter with the corresponding experimental values of R_a=0.106 μm at (a) P=1 bar (b) P=5 bar (c) P=10 bar	98
6.11	Comparison between bubble departure diameter predicted from present correlation and present experimental value	101

Fig. No.	Title of Figure	Page No.
6.12	Variation in bubble frequency with Jakob number at (a) P=1 bar (b) P=10 bar	102
6.13	Comparison of predicted fD_b^n by (a) Cole (1960) (b) Zuber (1963) (c) Jakob and Fritz (1931) with the corresponding experimental value	105
6.14	Comparison of present correlation for $fD_b{}^2$ with the experimental value	107
B.1(a)	Validation of experimental results of R_a=0.106 μm at P=1 bar	125
B.1(b)	Validation of experimental results of R_a=0.106 μm at P=5 bar	126
B. 1(c)	Validation of experimental results of R_a=4.03 μm at P=5 bar	126
B. 1(d)	Validation of experimental results of 4.03 μm at P=10 bar	127
B. 2(a)	Effect of surface roughness on pool boiling heat transfer during steady-state heat supply at 5 bar pressure	127
B. 2(b)	Effect of surface roughness on pool boiling heat transfer during steady-state heat supply at 10 bar pressure	128
B. 3(a)	Effect of surface roughness on pool boiling heat transfer during exponential heat supply at P=1, γ=1	128
B. 3(b)	Effect of surface roughness on pool boiling heat transfer during exponential heat supply at P=1, γ=3	129
B. 3(c)	Effect of surface roughness on pool boiling heat transfer during exponential heat supply at P=1, γ=4	129
B. 3(d)	Effect of surface roughness on pool boiling heat transfer during exponential heat supply at P=1, γ=5	130
B. 3(e)	Effect of surface roughness on pool boiling heat transfer during exponential heat supply at P=1, γ=6	130
B. 3(f)	Effect of surface roughness on pool boiling heat transfer during exponential heat supply at P=5, γ=1	131
B. 3(g)	Effect of surface roughness on pool boiling heat transfer during exponential heat supply at P=5, γ=2	131
B. 3(h)	Effect of surface roughness on pool boiling heat transfer during exponential heat supply at P=5, γ=3	132

Fig. No.	Title of Figure	Page No.
B. 3(i)	Effect of surface roughness on pool boiling heat transfer during exponential heat supply at P=5, γ=4	132
B. 3(j)	Effect of surface roughness on pool boiling heat transfer during exponential heat supply at P=5, γ=5	133
B. 3(k)	Effect of surface roughness on pool boiling heat transfer during exponential heat supply at P=5, γ=6	133
B. 3(l)	Effect of surface roughness on pool boiling heat transfer during exponential heat supply at P=10, γ=1	134
B. 3(m)	Effect of surface roughness on pool boiling heat transfer during exponential heat supply at P=10, γ=2	134
B. 3(n)	Effect of surface roughness on pool boiling heat transfer during exponential heat supply at P=10, γ=3	135
B. 3(o)	Effect of surface roughness on pool boiling heat transfer during exponential heat supply at P=10, γ=4	135
B. 3(p)	Effect of surface roughness on pool boiling heat transfer during exponential heat supply at P=10, γ=5	136
B. 3(q)	Effect of surface roughness on pool boiling heat transfer during exponential heat supply at P=10, γ=6	136
B. 4(a)	Effect of pressure on pool boiling heat transfer from square microchannel during steady-state heat supply	137
B. 4(b)	Effect of pressure on pool boiling heat transfer from stepped microchannel during steady-state heat supply	137
B. 4(c)	Effect of pressure on pool boiling heat transfer from parabolic microchannel during steady-state heat supply	138
B. 5(a)	Effect of time constant on pool boiling heat transfer from square microchannel during exponential heat supply at P=1 bar	138
B. 5(b)	Effect of time constant on pool boiling heat transfer from square microchannel during exponential heat supply at P=5 bar	139

Fig. No.	Title of Figure	Page No.
B. 5(c)	Effect of time constant on pool boiling heat transfer from square microchannel during exponential heat supply at P=10 bar	139
B. 6(a)	Variation in non-dimensional h_{ts} with non-dimensional q_{ts} for different surface roughness at P=1 bar, γ=2	140
B. 6(b)	Variation in non-dimensional h_{ts} with non-dimensional q_{ts} for different surface roughness at P=1 bar, γ=4	140
B. 6(c)	Variation in non-dimensional h_{ts} with non-dimensional q_{ts} for different surface roughness at P=1 bar, γ=5	141
B. 6(d)	Variation in non-dimensional h_{ts} with non-dimensional q_{ts} for different surface roughness at P=1 bar, γ=6	141
B. 6(e)	Variation in non-dimensional h_{ts} with non-dimensional q_{ts} for different surface roughness at P=5 bar, γ=1	142
B. 6(f)	Variation in non-dimensional h_{ts} with non-dimensional q_{ts} for different surface roughness at P=5 bar, γ=2	142
B. 6(g)	Variation in non-dimensional h_{ts} with non-dimensional q_{ts} for different surface roughness at P=5 bar, γ=3	143
B. 6(h)	Variation in non-dimensional h_{ts} with non-dimensional q_{ts} for different surface roughness at P=5 bar, γ=4	143
B. 6(i)	Variation in non-dimensional h_{ts} with non-dimensional q_{ts} for different surface roughness at P=5 bar, γ=6	144
B. 6(j)	Variation in non-dimensional h_{ts} with non-dimensional q_{ts} for different surface roughness at P=10 bar, γ=1	144
B. 6(k)	Variation in non-dimensional h_{ts} with non-dimensional q_{ts} for different surface roughness at P=10 bar, γ=2	145
B. 6(l)	Variation in non-dimensional h_{ts} with non-dimensional q_{ts} for different surface roughness at P=10 bar, γ=3	145
B. 6(m)	Variation in non-dimensional h_{ts} with non-dimensional q_{ts} for different surface roughness at P=10 bar, γ=4	146

Fig. No.	Title of Figure	Page No.
B. 6(n)	Variation in non-dimensional h_{ts} with non-dimensional q_{ts} for different surface roughness at P=1 bar, γ=4	146
B. 7(a)	Effect of time constant on transient CHF of rough and microchannel geometries at 1 bar pressure	147
B. 7(b)	Effect of time constant on transient CHF of rough and microchannel geometries at 10 bar pressure	147

NOMENCLATURE

A	constant	
Ar	Archimedes number	
a	exponent in the Rohsenow correlation	
Bo	Bond number	
C_d	bubble drag coefficient	
C_h	channel height	(μm)
C_L	lift coefficient	
C_p	specific heat	(J/kg K)
C_s	empirical constant in force term	
C_{sf}	coefficient in the Rohsenow correlation	
C_t	the proportionality factor	
C_w	channel width	(μm)
c_1	parameter given in Cole and Rohsenow (1969)	
D_b	diameter of bubble	(mm)
d	instantaneous bubble diameter	(mm)
F	force	(N)
f	bubble frequency	(Hz)
f_t	fin tip thickness	(μm)
g	gravity	(m/s^2)
H_b	bubble height	(mm)
h	heat transfer coefficient	(W/m^2K)
h_{fg}	latent heat	(J/kg)
Ja	Jakob number	
Ja^c	modified Jakob number	
j	number of reading	
K	term in the CHF model	
K_l	parameter defined by Chen et al. (2017)	
k_{cu}	thermal conductivity of copper	(W/mK)

m	exponent for surface roughness	
N	number of capillary tubes	
n	exponent for heat flux	
P	pressure	(bar)
P_r	reduced pressure	
Pr	Prandtl number	
Q	heat input	(W)
q''	heat flux	(W/m^2)
R	bubble departure radius	(mm)
R_a	average roughness	(μm)
R_q	root mean squared roughness	(μm)
R_z	ten-point average roughness	(μm)
r	instantaneous bubble radius	(mm)
r_c	cavity mouth radius	(mm)
S	accommodation factor	
S_m	mean spacing	(μm)
T	temperature	(°C)
t	time	(s)
t_g	growth period	(s)
t_w	waiting period	(s)
U	uncertainty	
V	volume	(m^3)
W_b	channel base width	(μm)
W_t	channel top width	(μm)
x	distance	(mm)

Greek symbols

α	thermal diffusivity	(m^2/s)
γ	time constant	
δ	thermal layer thickness	(μm)
Θ	contact angle	(^{0})

Θ_b	bubble angle	(^{0})
ΔT	wall superheat	(°C)
λ_T	Taylor unstable wavelength	(m)
μ	viscosity	(N s/m^2)
ρ	density	(kg/m^3)
σ	surface tension	(N/m)
τ	exponential period	(s)
Φ	angle of inclination	(^{0})
ω	fitting parameter	

Subscripts

0	reference
b	bubble
c	capillary
d	dry-out
g	gravity
l	liquid
M	momentum
ov	overshoot
s	surface tension
sat	saturated
suf	surface
ss	steady-state
st	surface tension
ts	transient-state
v	vapor
w	wall

Abbreviations

CHF	critical heat flux
CS	commercial surface
HI	hydrodynamic instability
HSN	heterogeneous spontaneous nucleation

HTC	heat transfer coefficient
MAE	mean absolute error
MS	mirror surface
OBD	onset of boiling driven
ONB	onset of nucleate boiling
OV	overshoot
PBHT	pool boiling heat transfer
RS	rough surface

CHAPTER 1

INTRODUCTION

1.1. BACKGROUND

- Economic Simplified Boiling Water Reactor (ESBWR)

By the end of World War II, scientists realised that the tremendous heat produced by the nuclear reaction could be tapped either for direct use or for generating electricity. In December 1951, the first nuclear reactor known as Experimental Breeder Reactor (EBR-1) was designed and operated by Argonne National Laboratory at Idaho, USA for the production of electricity. The US Department of Energy proposed the nomenclature for reactor designs and classified according to the progressive modification viz. Generation I, II, III and IV. The early prototype of power reactors, such as Shippingport, Magnox/UNGG, Fermi 1 and Dresden was entitled as Generation-I reactor. A generation-II reactor is a design classification for a nuclear reactor, and refers to the class of commercial reactors built up to the end of the 1990s. It includes the Pressurized Water Reactor (PWR), Canada Deuterium Uranium (CANDU), Boiling Water Reactor (BWR), Advanced Gas-cooled Reactor (AGR) and Water-Water Energetic Reactor (WWER). In 1996, Generation-III reactors were developed after evolutionary improvements in the design of generation-II reactors. These include improved fuel technology, superior thermal efficiency, passive nuclear safety systems and standardised design for reduced maintenance and capital costs. This generation design has achieved the longer operational life and better overall efficiency.

The Economic Simplified Boiling Water Reactor (ESBWR) is a Generation III+ reactor design derived from its predecessor, the Simplified Boiling Water Reactor (SBWR) and from the Advanced Boiling Water Reactor (ABWR). The Economic Simplified Boiling Water Reactor (ESBWR) has natural circulation system, as shown in Figure 1.1, to drive the coolant flow within the reactor pressure vessel. There are no circulation pumps or associated piping required for this design. This design of boiling water reactor ensures more design safety, integrity and reliability, while simultaneously reducing

overall reactor cost. The coolant, which absorbs the exponential heat generated in the fuel rod due to fission reaction, flows from the overhead tank and gets converted into vapour.

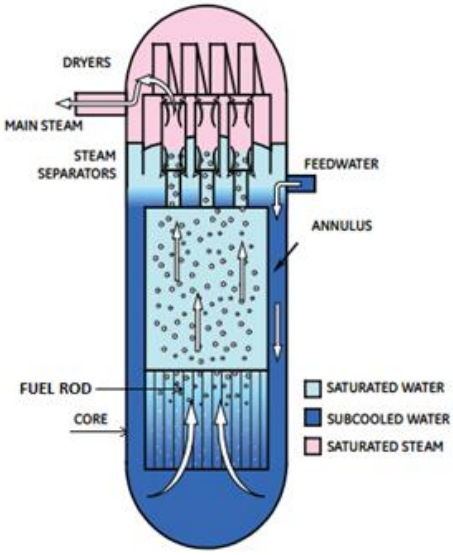

Figure 1.1 ESBWR core design (El-Genk, 2008)

1.2. CORE MELT ACCIDENT

Enormous amount of heat is generated due to exponential heat generation from the fuel rod. The heat generation rate in the fuel rod can be described as $Q \propto e^{\gamma}$, where γ, the time constant, is the ratio of heating period (t) and the exponential period (τ). In ESBWR, the heat is transferred from the fuel rod to the naturally circulated water by natural convection in the initial phase of heat generation. As the fuel rod temperature exceeds the saturation temperature of water, heterogeneous boiling of water commences. Thus, heat transfer from the fuel rod takes place by pool boiling of water. A core melt accident occurs when the heat generated in the nuclear reactor exceeds the heat removed by the coolant to the point where at least one nuclear fuel element exceeds its melting point temperature. A meltdown may be caused by loss of coolant accident (LOCA), loss of coolant pressure, or the result of a critical power excursion in which the reactor is operated at a power level that exceeds its design limits. LOCA can be categorised as the physical loss of coolant and the failure of coolant recirculation system. The physical loss of coolant occurs at critical heat flux (CHF) due to transition

of the nucleate boiling phase to film boiling i.e. it occurs when coolant in contact with the fuel rod gets evaporated completely, forming a vapour film over the surface. CHF is the phase of boiling after which heat transfer coefficient drops resulting in the increase in temperature of core. This uncontrolled temperature rise may reach upto melting point temperature of the core. Hence, understanding the mechanism of CHF is important to control LOCA. There exists a time lag between commencement of nuclear fission reaction and onset of boiling and this phase is called as non-boiling phase. Temperature shoots up during this time lag which may lead to the meltdown of the fuel rod. Hence, onset of boiling is also a key factor to be studied so as to maintain the surface temperature below melting point. The CHF value and its time of occurrence may vary with the rate of exponential heat supply. Hence, the time trace of nucleate boiling regime, CHF and its occurrence at corresponding time constant of exponential heat supply should be monitored to regulate the problem of physical loss of coolant. The study of bubble parameter like bubble departure diameter, bubble frequency and bubble coalescence is also important to estimate the transition of nucleate boiling regime. Reduction in boiling incipient temperature, extension of the fully developed nucleate boiling regime and enhancement in the CHF value may resolve the problem of LOCA and increase the thermal efficiency of the ESBWR.

1.3. TRANSIENT POOL BOILING HEAT TRANSFER

Since 1957, researchers are focusing their study on the transient boiling phenomenon. Noticeable variations between steady and transient state pool boiling curves were observed. The regimes like natural convection, nucleate boiling and film boiling during steady-state conditions are shortened and degraded during transient state of pool boiling as shown in Figure 1.2. The onset of boiling (ONB) as well as transition to film boiling varies with the rate of transient i.e. quasi-steady to rapid transient period. Incipient boiling can be a result of either homogeneous or heterogeneous nucleation. The first nucleated bubble may be the consequence of growth from either a pre-existing nucleus or a newly formed nucleus. The quasi-steady heat transfer takes place through the adjacent liquid layer until the onset of boiling i.e. during conduction or convection regime.

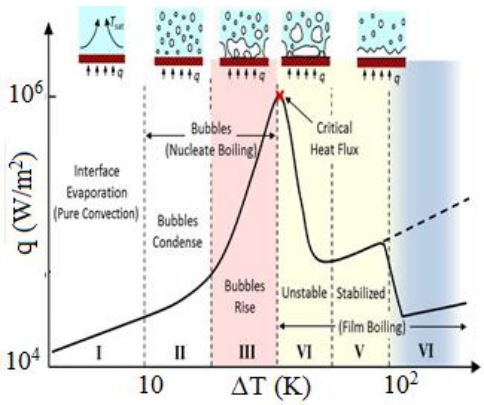

(a) Steady state
(http://www.putnamlabs.com)

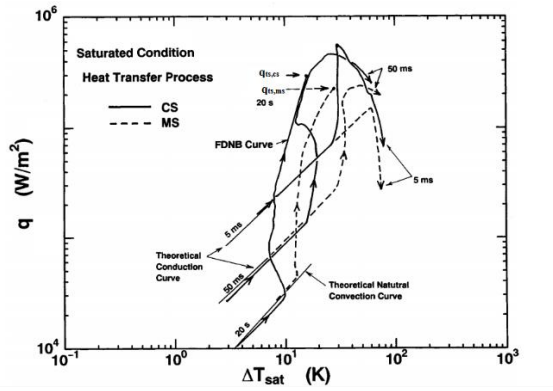

(b) Transient State (Fukuda et al., 2000)

Figure 1.2 Pool boiling Curve

1.4. HEAT TRANSFER ENHANCEMENT TECHNIQUE

Several enhancement techniques are utilized in order to improve the heat transfer or thermal performance. The goal of the heat transfer enhancement is to achieve high heat fluxes or heat transfer coefficient at low surface temperature. The enhancement techniques used in the appliances depend on the application and the requirement of cooling capacity. Generally, heat transfer enhancement techniques can be classified into passive, active and compound techniques. The passive techniques like extended surfaces, rough surfaces, additives, coiled tubes and swirl flow devices are preferred since no additional external power is required to drive the system. This technique is widely preferred in heating equipment due to their low-price, noiseless and trouble free operations. A keen survey is important for tracing the opportunity to implement the highly efficient, cheap and less complex modifications. The detailed study on the effect of geometrical variables like height, width, length, surface area, roughness etc. on the heat flux can help in the selection of best combinations. Active technique has proved the potential to stand against high heat duty application. It requires external power supply to drive the system and hence system becomes bulky which limits the use in heating equipment. Recently, combined approach of passive and active system so-called compound system has attracted many researchers because of its highly efficient

performance. However, part of active system involved in compound technique limits the application in nuclear reactor.

1.5. PASSIVE TECHNIQUES FOR POOL BOILING HEAT TRANSFER ENHANCEMENT

Since last two decades, many scientist-engineers have contributed for the development of the pool boiling heat transfer (PBHT) enhancement techniques. Specifically, boiling requires a different approach for selection of heat transfer intensifiers. Techniques of natural convection heat transfer augmentation generally involve increase in surface area of the passive device by any means. But this leads to the bulky design which may not be feasible. The boiling curve has short span of convection regime. Hence, increase in wetted surface area for PBHT enhancement seems to be insignificant. The nucleation sites, bubble size, bubble frequency and mostly, rewetting characteristics greatly contribute to the latent heat transfer during pool boiling. Attempts are made to increase the pool boiling heat transfer by using various nano/micro/mini structured passive components like porous foam, sintered coating, roughness, re-entrant cavities, micro-studs, layer of wire mesh, carbon nanotubes (CNT), microgrooves of various cross-section and orientations, graphene oxide layer and chemically treated surfaces, etc. Few such techniques used in the literature are shown in Figure 1.3. The reduction in the boiling incipience temperature is the consequence of increase in the nucleation sites. Bubble population directly depends on the active nucleation sites. An optimum nucleation sites should be maintained as increased bubble density may lead to early formation of vapour layer due to horizontal coalescence. Liquid rewetting characteristics can be improved by various methods like porous layer, rough surface or chemical treatment. As the affinity of liquid towards the hydrophilic surface is high, the horizontal bubble coalescence can be retarded. Hence, fully developed nucleate boiling regime can be prolonged. Significant liquid replenishment due to improved wettability may also increase the bubble frequency. The bubble dynamics in passive structured surface like microchannel seems to be complex since horizontal coalescence may take place due to larger bubble diameter which adversely affects the pool boiling heat transfer. The optimised design of structured surface may result in the heat transfer enhancement. The extended surfaces like micro pin-fin, microgrooves, and dots have

the ability to enhance heat transfer by the virtue of selective nucleation sites and the optimum bubble parameter which prolongs the fully developed nucleate boiling phase.

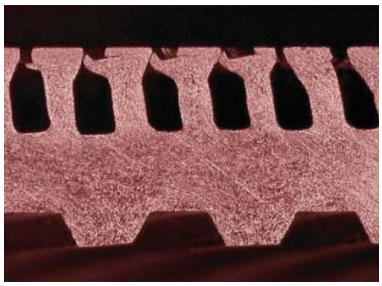

Re-entrant cavities (Kedzierski and Fick, 2015)

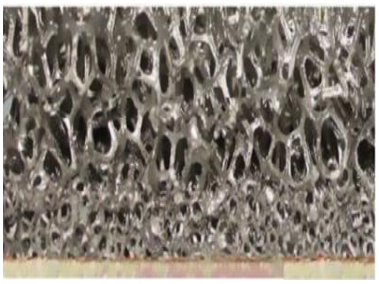

Porous surface

(Xu and Zhao, 2015)

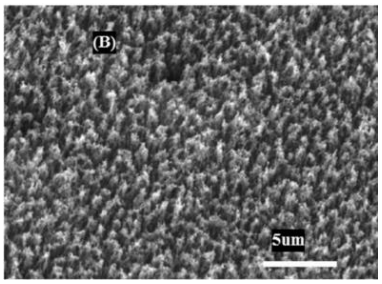

CNT

(Dharmendra et al., 2016)

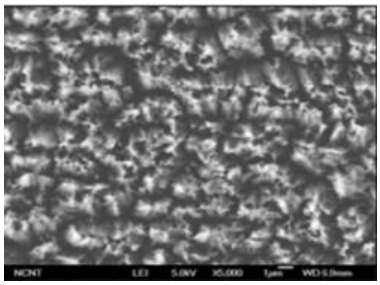

Chemical treatment

(Ahn et al., 2010)

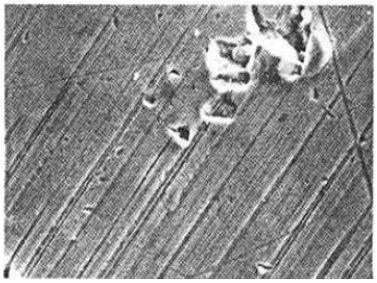

Rough surface

(Anderson and Mudwar, 1989)

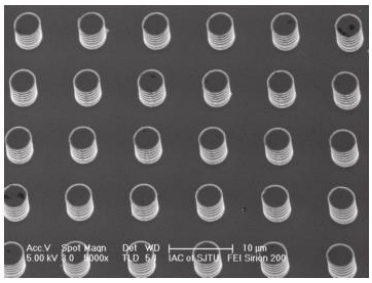

Micro-studs

(Dong et al., 2014)

Figure 1.3 Passive techniques for pool boiling heat transfer enhancement

As discussed earlier, CHF enhancement may retard the LOCA in ESBWR. Thermal efficiency of the reactor may also increase with increase in CHF. Passive techniques of pool boiling heat transfer enhancement are the most suitable for the nuclear reactor application. The reduction in temperature overshoot during non-boiling phase and prolonged fully developed nucleate boiling regime due to passive methods may result in the overall improvement of pool boiling mechanism during exponential heat supply. Thus, the investigation of pool boiling heat transfer and CHF enhancement by passive techniques during exponential heat supply becomes important. In view of the facts

discussed above, present study aims to determine the CHF for water at different rate of exponential heat supply. The literature will be reviewed to understand the experimental results of various passive techniques and thereafter, steady and transient CHF enhancement by the most feasible passive technique with different geometrical aspects will be studied in the present work. Study will also be focused on the bubble dynamics in pool boiling to understand the mechanism of CHF enhancement.

1.6. ORGANIZATION OF THE THESIS

This thesis consists of eight chapters namely introduction, literature review, experimentation, results and discussion, CHF model, bubble dynamics, conclusions and scope for future work. Bibliography is followed by appendices section.

The second chapter reviews the literature on pool boiling studies using microchannel geometries and rough surfaces. It also summarizes the pool boiling study during transient heat supply. Various CHF models developed so far and bubble dynamics studies are also reported in this chapter. Summary of literature review followed by the scope and objectives are given at the end of this chapter.

The third chapter describes the details of experimentation which includes sample preparation, sample characterization, experimental setup details, experimental procedure followed by visualization, data reduction. Uncertainty estimation, repeatability and hysteresis are also given in this section.

The fourth chapter summarizes the results of the present study and its critical discussion. CHF for plain, rough surface and microchannel geometries during steady and transient heat supply is reported followed by the development of HTC correlation.

The development of CHF model considering the forces acting on the bubble in horizontal direction is given in the fifth chapter.

The bubble dynamics of water is discussed in sixth chapter. The effect of surface characteristic on the bubble parameter like bubble departure diameter and bubble

frequency is discussed. Correlation for prediction of bubble departure diameter and bubble frequency of rough surface is also presented.

Seventh chapter concludes the results obtained from the present study and gives the scope for future work.

CHAPTER 2

LITERATURE REVIEW

Literature review for this dissertation is divided into five sections. The first and second sections provide the literature on the study of pool boiling heat transfer on microchannel and rough surfaces, respectively. The experimental studies carried out under transient heat supply are reviewed in the third section. The CHF models developed in the literature are summarized in the fourth section. The fifth section describes the bubble dynamics study conducted for the modified surfaces.

2.1 POOL BOILING ON MICROCHANNEL GEOMETRY

Experimental studies have been carried out by using various types of microchannel geometries since last two decades. The details of pool boiling study using microchannel are summarized in Table 2.1. The method of fabrication, characteristics of the microchannel and the outcomes of the experiments are discussed in this section.

Chien et al. (1998) tested the tubular test surfaces having sub-surface tunnels and surface pores. A copper and transparent plastic foil was used to cover the fin tip surface so as increase the nucleation density. A suction-evaporation boiling at horizontal and vertical position of the tubes was observed over the 90% of the area. In contrast, rest of the area was covered with oscillating liquid meniscus.

Bhavani et al. (2001) observed the boiling insights over the etched commercially available structures viz. GEWA-T, Turbo-B, etc. The mouth size of the chemically etched re-entrant cavities was approximately 40 µm. The minor contribution (<16%) of latent heat over the total heat transfer indicated the dominance of convection phenomenon.

Ghiu and Joshi (2005) found the weak dependence of channel width on heat transfer performance of enhanced structure. They proved that the channel pitch has great influence on the ebullition and growth of the bubble. The existence of dynamic nature of internal evaporation was noticed by the oscillatory movement of the vapor slug over the top and bottom of the channel.

Yu and Lu (2007) studied, for the first time, the effect of area enhancement ratio on the critical heat flux (CHF). The effect of fin spacing and fin height on the heat transfer was examined. They found that closer and higher fins can offer the flow resistance to lift-off the growing bubble. Higher aspect ratio i.e. decrease in the fin spacing or increase in the fin height adversely affected the boiling performance.

Cooke and Kandlikar (2011 and 2012) used deep reactive etching method to fabricate the microchannel. They observed that wider channel provides the highest heat transfer rate because it assists the growth of bubble population. They noticed that the microchannel with channel width=375 µm, channel height=400 µm and area augmentation factor=2.30 has maximum heat transfer performance.

Qu et al. (2012) investigated the pool boiling characteristics with metallic foam in saturated water. Single and cross direction V-grooves were made over the metallic foam. Porosity was kept constant at 0.95. Effect of different directional V-grooves and its width were critically studied. Bubble escaping resistance and capillary force was estimated to account for the boiling phenomenon. Porous foam has potential to increase the nucleation density and additionally, V-grooves can accommodate the expanding volume of the bubbles. The peak heat transfer coefficient increased with increase in number of grooves at 2 mm optimal groove width.

Mehta and Kandlikar (2013) tested cylindrical tubes with rectangular circumferential microchannel and investigated the effect of the horizontal and vertical orientation of the tubes on the heat flux. Also, parametric study of the channel depth, the fin width and the channel width was performed. Heat transfer coefficient (HTC) at horizontal and vertical orientations was 129 kW/m^{2}K and 109 kW/m^{2}K, respectively at about 1093 kW/m^2 heat flux. They concluded that the microchannel geometry having wider fins of approximately 0.3 mm performed better.

Patil and Kandlikar (2014) followed the hybrid technique of enhancement with microporous coating on the fin top. Microchannel of 500 µm and 762 µm channel width with fin width=200 µm and channel height=400 µm had the best performance with CHF=3250 kW/m^2 and HTC=995 kW/m^{2}K, respectively. They found that the heat transfer rate increases with increase in the channel height. They concluded that HTC decreases up to certain value and again increases with the increasing channel width.

Jaikumar and Kandlikar (2016) conducted experiments to study the effect of channel width on pool boiling performance of sintered-throughout, sintered-fin-tops and sintered-channel configurations. They reported that heat transfer from the rectangular microchannel of sintered-fin-top is 270 % higher compared to the plain surface. They also studied the cohesive effect of the channel width and channel height on the heat transfer. They commented that wider channel provides additional liquid path-ways to feed to the nucleation sites, thus resulting in the higher CHF and HTC compared to a narrower channel.

Table 2.1 Details of the studies available in the literature related to microchannel geometries

Author	Base Material	Boiling Fluid	Characteristics	Fabrication Technique	Size/Shape/ Type of the structure	CHF	HTC
Ghiu & Joshi, 2005	Cu	PF-5060	Microchannel [C_w=65-105-360 µm, pitch=0.7 mm, C_h=0.6 mm]	Automated wafer dicing diamond saw blade	10x10 mm^2	~13 W/cm^2	-
Yu & Lu, 2007	Cu	FC-72	Rectangular fin array [S=0.5,1,2 mm; C_h= 0.5,1,2,4 mm]	EDM	10x10 mm^2	980 kW/m^2	~10 kW/m^2K
Cooke & Kandlikar, 2011	Cu	DI water	Microchannel [C_w=40,100,400µm; f_t=40,100,200µm;C_h=192,208,273µm]	DRIE	Microstructure 10x10 mm^2	~1400 kW/m^2	72.3 kW/m^2K
Cooke & Kandlikar, 2011	Cu	DI water	Microchannel [C_w=197-375-400µm; C_h=100-400-445µm, N=16,20,25]	Machining	Microstructure	2500 kW/m^2	270 kW/m^2K
Mehta & Kandlikar, 2013	Cu alloy 101	Water	Circumferential microchannel [C_h=0.25-0.3-0.41 mm; C_w=0.28-0.29-0.40 mm; f_t=0.21-0.30mm; pp=0.5,0.59,0.6,0.7]	CNC	Microstructure	q_{hor}= 1095 kW/m^2	h_{hor}=129 kW/m^2K
						q_{ver}= 1093 kW/m^2	h_{ver}=109 kW/m^2K
Mehta & Kandlikar, 2013	Cu alloy 101	Water	V-grooves and axial rectangular grooves [C_h=0.22-0.37-0.51 mm; pitch=0.39-0.54-0.70 mm;Θ=45,60°]	CNC	Microstructure	1070 kW/m^2	h=96 kW/m^2K
Patil & Kandlikar, 2014	Cu	DI water	Microchannel + microporous coating at fin top [f_w=^{a,b}200,500,1000µm; C_w=300,400,^{a}500,^{b}762µm; C_h=200,300,^{a,b}400µm]	Microchannel- CNC, microporous coating- Electrolytic process	Hybrid microstructure [10x10 mm^2]	^{a}3250 kW/m^2	^{b}995 kW/m^2K
Jaikumar & Kandlikar, 2016	Cu	DI water	Microchannel + porous fin top	Sintering, CNC	Rectangular microstructure	4200 kW/m^2	-

2.2 POOL BOILING ON ROUGH SURFACE

Several experimental studies of pool boiling heat transfer from rough surface have been presented to reveal the mechanism of heat transfer enhancement. The details of those studies is summarized in Table 2.2. The surface texture with different preparation techniques and their heat transfer performance is discussed in this section.

Anderson and Mudwar (1989) carried pool boiling experiment in FC-72 to examine the effect of rough surface on heat transfer. Rough surface of R_a = 0.6 μm -1.0 μm was prepared by 600 grit SiC sandpaper. The CHF for the rough sample was found to be 205 kW/m^2. They reported the insignificant role of surface roughness in CHF enhancement.

Benjamin and Balakrishnan (1997) conducted pool boiling experiments using rough surface in water, CCl_4, acetone, and n-hexane. They concluded that increased nucleation sites due to surface roughness resulted in the enhanced heat transfer. They developed the correlation for the nucleation site density considering only the surface material, however, the surface wettability was not considered.

Kang (2000) conducted experiments with pool-boiling on a horizontal, inclined, and vertical tube and found that the orientation effect on the HTC could be significant. The heat transfer enhancement from the rough surface was justified through nucleation site density, bubble agglomeration on the surface, intensity of liquid agitation and formation of rapid flow around the tube surface.

Jones et al. (2009) studied the effect of surface roughness on pool boiling heat transfer over a wide range of roughness values in water and FC-77. The general trend of increasing heat transfer coefficient with surface roughness was correlated using $h \alpha R^m$. The results indicate a stronger dependence on surface roughness for FC-77 with m=0.2 compared with m =0.1 for water. They found lowest error between experimental values and predicted values by Gorenflo correlation for water.

Ahn et al. (2010) performed anodization to modify the surface wettability of the Zircaloy-4. Contact angle of the bare surface reduced from 49.3^o to 0° for the treated surface whereas R_a increased from 0.15 μm to 0.32 μm. CHF of the superhydrophilic surface was found to be 1924 kW/m^2. Liquid spreadability was significantly improved

due to surface roughness. The effect of surface roughness on CHF remained unclear in their study.

McHale et al. (2010) conducted experiments on the sample of R_a=0.038 μm–10.0 μm. Rough samples were prepared by polishing and EDM. Bubble nucleation characteristics were also studied by visualisation technique. Enhancement in HTC of water was found to be 100% for the roughest surface. They commented that HTC enhancement is the consequences of increased nucleation site density whereas increased wetted surface area does not play significant role in HTC enhancement.

Hosseini et al. (2011) prepared rough copper, brass, and aluminium surfaces by polishing with sandpapers and conducted pool boiling experiments in R113. HTC for copper sample was found to be higher than that for brass and aluminium, although it had least R_a.

Dong et al. (2014) investigated the effect of the micro/nano structures like micro-pillars (MP), micro-cavities (MC), nanowires (NW) and nano-cavities (NC) on the bubble departure characteristics and nucleation density. Microstructures were fabricated by dry and wet etching. It was found that nanostructure helps to reduce the bubble departure diameter, accelerate the bubble frequency and delays the bubble coalescence. They noticed that cavity radius and wall superheat have vital role in the bubble nucleation density.

Kruse et al. (2015) fabricated multiscale structure on 304 stainless steel surface by femtosecond laser surface process (FLSP). It formed a self-organised mount like structures covered by layer of nanoparticles. The surface roughness R_a was varied from 1.4 μm to 7.8 μm. The sample of R_a =1.4 μm was found to have CHF of 1420 kW/m^2 which was higher than that of R_a =7.8 μm. However the HTC for R_a =7.8 μm was 38.68% higher than that for R_a =1.4 μm. They commented that surface wettability and its wicking ability enhance the cooling effect. Additionally it was found that boiling curves moved towards left with increase in R_a.

Saeidi et al. (2015) reported the pool boiling characteristics of the aluminised copper sample in DI water. They found that CHF of aluminised surface is 37% higher than that of untreated copper surface. The treated surface had shown higher surface roughness and contact angle compared to the untreated surface. Despite higher contact angle, CHF

for treated surface was found to be higher which suggests that CHF is not the function of contact angle only.

Li et al. (2015) examined the compound effect of nano-scale roughness, contact angle and wetted surface area on HTC. The samples were prepared by electrochemical deposition on the Ni foil and nano-cone array was obtained where R_a found to be unchanged. HTC decreased with decrease in the contact angle whereas HTC enhanced with increase in wetted surface area.

Kim et al. (2016) studied the effect of surface roughness on surface wettability for the sample of R_a varying from 0.041 μm to 2.36 μm. Wettability was found to be increased due to capillary wicking through the narrow scratches. They commented that CHF enhancement due to rough surface is the consequences of capillary wicking and reduced contact angle.

Kim et al. (2017) studied pool boiling characteristics of rough and superhydrophilic surface aluminium sample. Hot water treatment resulted in the formation of superhydrophilic nanoscale protrusions on the aluminium surface which proved significant heat transfer.

Table 2.2 Details of the studies available in the literature related to rough surface

Author	Base Material	Boiling Fluid	Characteristics	Fabrication Technique	Size/Shape/Type of the structure	CHF	HTC
Anderson and Mudwar, 1989	Cu	FC-72	Rough surface [R_a=0.6-1.0 µm]	SiC polishing	12.7x12.7 mm^2	205 kW/m^2	-
Jones et al., 2009	Al	FC-72	Smooth [R_a=0.38 µm] Rough [R_a=1.08,2.22,5.89,10 µm]	Smooth-Mechanical Polishing Rough-EDM	25.4x25.4 mm^2	~190 kW/m^2	14 kW/m^{2}K
Ahn et al., 2010	Zr-4	DI water	ψ=0-43.3°, R_a=0.15-0.32 µm	Anodization (time-0-600 s)	20x25x0.7 mm; rectangular	1924 kW/m^2	-
Dong et al., 2014	Si	Ethanol	[a]Micropillar [d=5,10,20,50,100µm; h=5,50µm] [b]Nanowire [d=0.3-0.8µm; h<1.32µm]	Micropillar-Dry etching Nanowire-wet etching ($AgNO_3$+HCL)	Microstructure	[a]~620 kW/m^2 [b]~650 kW/m^2	[b]45 kW/m^{2}K
Kruse et al., 2015	SS	DI water	Mound like microstructure [R_a=1.4,4.6,7.4,7.8]	Femtoscale laser process	Hybrid microtructure	1420 kW/m^2	67.4 kW/m^{2}K
Saeidi et al., 2015	Cu & Al alloy	DI Water	Aluminised copper surface [R_a=41nm; h=406nm; Θ =66°]	Aluminising	Coating	1227 kW/m^2	70 kW/m^{2}K
Li et al., 2015	Ni	Water	Chemically treated nano-cone array [R_a=0.027 µm -0.22 µm; Θ=90°-5°; r=1-1.45]	Electro chemical process	Foil [1x5 mm^2]	1700 kW/m^2	70 kW/m^{2}K
Kim et al., 2016	Cu	DI water	Unidirectional scratches [R_a=0.041 µm -2.36 µm]	Polishing	-	1625 kW/m^2	-
Kim et al., 2017	Al	DI water	[R_a=0.11 µm -2.93 µm]	Hot water treatment	-	2150 kW/m^2	-

2.3 TRANSIENT POOL BOILING HEAT TRANSFER

Since 1957, researchers, scientists and academician have contributed to reveal the mechanism of the pool boiling under transient heat supply. The transient system is achieved by time variant heat supply like linear, exponential, stepwise or pulse type. The details of experimental conditions are summarized in Table 2.3.

Rosenthal (1957) examined the effect of transient heating on the transient CHF at atmospheric pressure on platinum ribbon and reported that transient CHF is not influenced by the transient state of heat supply. It was observed that natural convection did not contribute to heat transfer during the non-boiling phase at short periods (<100 ms) due to rapid temperature rise. The leading heat transfer mechanism was instead conduction, for which Rosenthal proposed an analytic solution.

Johnson (1971) investigated the transient boiling heat transfer at pressure up to 13.78 MPa and commented that transient CHF for exponential heat input exceeds the steady-state CHF. They studied the variation between ONB heat flux and corresponding wall superheat at different transient of exponential heat supply.

Extensive work is carried by Sakurai and his research team to understand the transient boiling under exponential heat supply using thin elements on different wetting fluids at different pressures. Sakurai and Shiotsu (1977) carried experiments on platinum wire in pool of water and reported that incipient boiling temperature and its corresponding heat flux increases with decrease in exponential period. They have found the non-uniform trend of transient HTC with the exponential period. They commented that transient CHF increases initially, then decreases and finally increases as the exponential period decreases.

Sakurai et al. (1992) studied the non- boiling to film boiling transition in liquid nitrogen on horizontal cylinder for various transient heat supply. They reported that steady state CHF is higher than transient CHF.

Drach et al. (1996) studied the effect of surface roughness on the transient PBHT of liquid nitrogen. A wide range of surface roughness values from R_a=0.1 μm to 4.8 μm was examined. The researchers reported that the onset of nucleate boiling (ONB)

temperature exponentially drops with an increase in the surface roughness value. They also observed that the increase in transient CHF with the R_a was lower than the steady state CHF for all the transient heat inputs.

Fukuda et al. (2000) also investigated the effect of surface conditions of platinum cylinders in a pool of water on the two different surface conditions with mirror surface (MS) and a rough surface (RS) finished, however the exact surface roughness values are not reported. Marginal changes are observed in transient boiling heat transfer due to RS.

Duluc et al. (2004) studied the role of nucleation site density and the thermal inertia of the flat thick test piece during stepwise heat generation. They commented that the thermal behaviour and the associated time constants will be controlled by temperature at boiling inception during stepwise heat generation. They observed that ONB temperature in steady-state condition is lower than that in stepwise heating. They insisted that the boiling onset is more likely to result from the activation of pre-existing vapor embryos entrapped in the cavities.

Deev et al. (2007) studied the effect of heat generation in a heater on the transition from nucleate to film boiling regime. A drastic reduction in the critical time interval and transient CHF is reported in their study. They commented that transient CHF decreases significantly with increase in the initial heat load. They commented that the transition to film boiling occurs during short-term unsteady heating when the energy accumulated in the thermal boundary layer prior to boiling onset, overcomes the energy required for the formation of a stable vapor film.

Park et al. (2012) investigated the dynamic PBHT of highly wetting fluid like FC-72 from 1 mm diameter horizontal cylinder under an exponential heat supply. Two distinct mechanisms viz. hydrodynamic instability (HI) and heterogeneous spontaneous nucleation (HSN) were reported. The CHF in the steady-state condition at lower subcooling occurred due to the time lag of HI, whereas the explosive process of HSN during short period of transient in originally flooded cavities resulted in the transient CHF. A comparative heat transfer study was done between commercial surface (CS) of R_a=0.11 μm and RS of R_a=0.24 μm. The CHF of the CS was considerably lower than

that of the RS during the short period, whereas it suddenly increased with the increase in the period. This means that CHF during a short period is highly influenced by the surface roughness.

Htet et al. (2016) experimentally tested the transient boiling characteristics on CS, treated surface I (TS-I) polished by buff paper together with alumina and treated surface II (TS-II) finished by emery paper of a vertically oriented ribbon. During slow transient, the enhancement in transient CHF of TS-II was found to be 16 % and 28 % compared to the CS and the TS-I, respectively. They also reported that transient CHF are dependent on the period of transient as well as system pressure.

Su et al. (2016) studied boiling crisis on a plate heater due to exponential heating. They identified ONB, onset of the boiling driven (OBD) phase and temperature overshoot conditions for different period of exponential transient. The ONB temperature and corresponding heat flux was found to be increased with increase in the rate of exponential heating.

Balakin et al. (2017) presented experimental results on boiling of liquid nitrogen at different heating conditions. They studied the influence of pressure, heater size and type of the fluid on the boiling crisis during unsteady heating. They commented that size of the heater highly influences the extremum boiling crisis.

Table 2.3 Summary of the experimental conditions used in the literature during transient pool boiling studies

Authors	Medium	Heating Element	Element Material	Period/rate of exponential transients	Subcooling	Operating Pressure	Surface condition
Rosenthal, 1957	Water	Ribbon (0.025 mm thick, 2.5 mm wide)	Platinum and Aluminium	Exponential (τ=5-75 ms)	0-68 K	Atmospheric	-
Johnson, 1971	Water	Ribbon 0.10/0.36 mm thick 3.2 mm wide	Platinum	Exponential (τ=5 to 50 ms)	5–62 K	Ambient to 13.8 MPa	-
Sakurai and Shiotsu, 1977	Water	wire (φ=1.2 mm)	Platinum	Exponential (τ=5 ms- 10s)	25-75 K	Atmospheric	-
Sakurai et al., 1992	LN_2	Cylinder (φ=1.2 mm)	Platinum	Exponential (τ=7ms-100s), Stepwise	0-77.4 K	Atmospheric-2.047 MPa	-
Drach et al., 1996	LN_2	Film	Ni And Varnish (Sio_2)	Pulse (~0.25 s)	-	Atmospheric	R_a=0.1,1.4, 2.4, 3.6,4.8 μm
Fukuda et al., 2000	DI Water	Cylinder (Φ=1.2mm)	Platinum	Exponential (τ =2ms-20s)	0-60 K	Atmospheric-1.082 MPa	CS (R_a=0.11 μm) and RS (R_a=0.24 μm)
Duluc et al., 2004	LN_2	Thick sample (Φ=30 mm)	Copper	Stepwise	Saturated	Atmospheric	R_a = 0.06 μm and R_a = 1 μm
		Wire (Φ= 25 μm)	Bronze				
Deev et al., 2007	Water	Wire (Φ=0.1mm)	Platinum	Stepwise	Saturated	Atmospheric	-
Park et al., 2012	Ethanol and FC-72	Cylinder (Φ=1 mm)	Platinum	Exponential (τ=20ms-2s)	0-60 K	Atmospheric-1.082 MPa	CS (R_a=0.11 μm) and RS (R_a=0.24 μm)
Htet et al., 2016	Water	Ribbon 0.05 mm-0.1mm thick	Platinum	Exponential (τ=5 ms-20 ms)	0-20 K	0.1-0.297 MPa	R_a =0.04 μm, R_a =0.12 μm, R_a =0.22 μm
Su et al., 2016	Water	0.7 μm thick film	ITO/sapphire	Exponential (τ =5ms-500 ms)	0–75	Atmospheric	-
Balakin et al., 2017	LN_2	Wire (Φ=100μm)	Platinum	Pulse	-	0.1-0.4 MPa	-

2.4 CHF MODEL

Researchers have contributed to explain the CHF mechanisms by various approach viz. (i) Kelvin–Helmholtz instability between the upward flow vapor columns and downward flow liquid, (ii) dry-out of the liquid layer i.e. micro/macrolayer dry-out. The CHF model developed in the literature is given in this section.

Kutateladze (1948) and Zuber (1959) considered the Kelvin-Helmholtz instability as surface-fluid interaction fails due to relative motion between vapor column and surrounding liquid. The final form of Zuber's far field model is given in Equation (2.1).

$$q''_{CHF,Zuber} = 0.131\, h_{fg}\sqrt{\rho_v}\,[\sigma g(\rho_l - \rho_v)]^{0.25} \tag{2.1}$$

Chang (1961) considered the forces acting on the bubble during lift off from the horizontal surface and claimed that the critical velocity of the upward moving bubble is responsible for CHF. It is assumed that the vapor continues to leave the heater surface until the critical velocity is reached whereas beyond it vapor is pushed back to the heater surface. The CHF model developed by *Chang (1961)* is given in Equation (2.2).

$$q''_{CHF,Chang} = 0.098\, h_{fg}\sqrt{\rho_v}\,[\sigma g(\rho_l - \rho_v)]^{0.25} \tag{2.2}$$

Haramura and Katto **(**1983) explained the near field evaporation phenomena through the macrolayer evaporation model. They considered the microlayer as well as macrolayer evaporation underneath the growing bubble and they estimated CHF at the dry-out condition.

Pasamehmetoglu et al. (1993) and Lay and Dhir (1995) developed the theoretical model based on microlayer evaporation. Zhao et al. (2002) developed the CHF model for steady and transient heating condition. They estimated the time variant microlayer thickness and its evaporation during each bubble cycle. The initial and final bubble growth was theoretically modeled to estimate the corresponding bubble radius. They also included the macrolayer evaporation and transient conduction during entire boiling phase.

It is proved that surface properties have important role in the boiling characteristics. Hence, hydrodynamic models developed by Kirishenko and Cherniakov (1973), Wei

and Honda (2003) and Howard and Mudawar (1999) were coupled with surface-fluid properties like contact angle, surface roughness and heater orientation, respectively. The effects of boiling surface properties must be included in a robust and widely applicable CHF model.

Kandlikar (2001) for the first time developed a model by considering the role of contact angle followed by force balance approach having compatibility with different fluids. The CHF estimated from the force balance among evaporative forces, gravity and surface tension is given by Equation (2.3).

$$q''_{CHF,Kandlikar} = \left(\frac{1+cos\,\theta}{16}\right)\left\{h_{fg}{\rho_v}^{0.5}\,[\sigma g(\rho_l-\rho_v)]^{0.25}\right\}\left[\frac{2}{\pi}+\frac{\pi}{4}(1+\cos\theta)cos\phi\right]^{0.5} \tag{2.3}$$

Ahn et al. (2011) claimed the key role of wetting property of the surface. In their experiments, they observed the liquid spreading in the micro-structures and believed that CHF enhancement is a consequence of both the improved surface wettability and the liquid spreading ability of the artificial micro/nanostructures. They included capillary wicking term in the Kandlikar' model to estimate the CHF as given in Equation (2.4).

$$q''_{CHF,Ahn} = q''_{CHF,Kandlikar} + \frac{\varepsilon\delta\rho_l h_{fg}K}{A_{heat}}\frac{dA_w}{dt} \tag{2.4}$$

Quan et al. (2014) developed CHF model for micro/nanostructures, as given in Equation (2.5), based on a force balance analysis, considering the effects of contact angle, capillary wicking force, and roughness factor *r*.

$$q''_{CHF,Quan} = \left(\frac{1+cos\,\theta}{16}\right)\left\{h_{fg}{\rho_v}^{0.5}\,[\sigma g(\rho_l-\rho_v)]^{0.25}\right\}\left[\frac{2}{\pi}\left(1-\sqrt{\emptyset_s}\right)^{-0.5}\left(\frac{r+cos\theta}{1+cos\theta}\right)+\frac{\pi}{4}\left(1-\sqrt{\emptyset_s}\right)^{0.5}(1+\ cos\theta)\,cos\phi\right]^{0.5} \tag{2.5}$$

2.5 BUBBLE DYNAMICS

Sakurai et al. (2000) observed the behavior of vapor bubbles and vapor film during the transition from non-boiling regime to film boiling regime on horizontal cylinder in liquid nitrogen and in water due to exponentially increasing heat inputs. They

confirmed that the direct transitions in liquid nitrogen and in water occur due to the explosive-like heterogeneous spontaneous nucleation (HSN) in originally flooded cavities.

Cooke and Kandlikar (2011) studied the bubble dynamics over plain and enhanced microchannels at different heat flux. They found that bubble nucleate at the bottom of the channels and thereafter move to the top wall of the channel and grows. This allows for an efficient boiling process, with liquid filling the channels and vapor generated above. In case of offset strip fin configuration, they found that liquid flow to the nucleation site is not as efficient. The geometry obstructs the liquid flow to the nucleation sites in the passages.

Yeom et al. (2015) studied the bubble behaviour during pool boiling on nanoparticle-coated surfaces. They observed that presence of coating has reduced the average bubble departure volume and nucleation site density and increased bubble departure frequency.

Moita et al. (2015) studied the influence of micro-patterned pillars on bubble dynamics. They commented that the spacing between two adjacent pillars precludes horizontal coalescence and delays the formation of the vapor blanket, while allowing some liquid to flow between the pillars.

Sun et al. (2017) studied the bubble dynamics on microgrooved surfaces with reentrant cavities on copper substrate. They commented that due to the strong capillary suction of the reentrant cavities, the interface of the liquid and bubble is unstable, which induces a more chaotic flow in the microlayer under the bubble. Therefore, the bubble detaches from the cavity more easily, leading to a smaller departure diameter.

2.6 NEED FOR FURTHER RESEARCH

The study of pool boiling heat transfer from thin and lumped test sample under exponential heat supply is presented in the literature. However, the pool boiling characteristics of thick and non-lumped test sample under transient condition is less understood. The transient CHF enhancement and its mechanism is also not clear in the literature. Since it becomes important to control the LOCA in the bulky, non-lumped mass of fuel rod and to improve the thermal efficiency of ESBWR, the present study

aims to investigate the transient pool boiling heat transfer from thick and non-lumped test sample at pressure upto 10 bar. The transient CHF enhancement by passive techniques namely, rough surface and microchannel geometries, will be examined. Since water is the working fluid in ESBWR, the present study of pool boiling is carried with water.

The steady-state pool boiling study on various types of microchannel geometries is carried out in the literature using working fluid like water, FC-72 and ethanol. The literature presented above indicates that microchannel geometries have great potential in the steady-state CHF enhancement. However, the CHF enhancement by microchannel geometries during exponential heat supply is never been examined. In the present work, the comparative study of pool boiling heat transfer from different microchannel geometries like square, parabolic and stepped microchannel will be carried out for steady as well as transient heat supply. Critical study of effect of channel profile on bubble departure diameter and bubble frequency will also be presented. Bubble departure diameter will be predicted by force balance approach.

Various modes of sample preparation are adopted to achieve surface texture with different roughness value. Empirical correlations are also developed to estimate the heat transfer coefficient for rough samples. High speed visualization is also carried out to study the bubble morphology. CHF model is developed for steady-state condition considering various aspects of the pool boiling. However, wide range of surface roughness is not tested in transient pool boiling studies presented in the literature. Present study aims to examine the effect of surface roughness obtained by unidirectional scratches on PBHT under steady and transient heat supply at high pressure. Contact angle of water will be measured to understand the effect of unidirectional scratches on the wettability which will be helpful to justify the CHF enhancement. The correlation for heat transfer coefficient will be developed which will be useful to predict the transient boiling performance. The CHF model for rough surface will be developed to predict the boiling crisis during exponential heat supply. Bubble dynamics during pool boiling heat transfer will also be studied to understand the heat transfer mechanism. The bubble departure diameter and bubble frequency for rough

surface will be predicted by considering the forces acting on the bubble during vertical growth.

2.7 OBJECTIVES OF THE PRESENT RESEARCH WORK

1. To study the effect of surface roughness and microchannel profile on CHF of water during pool boiling under steady and transient heat supply.
2. To study the effect of pressure and time constant of exponential heat supply on CHF of water during pool boiling on rough surface and microchannel geometries.
3. To develop a correlation for transient heat transfer coefficient and a model for critical heat flux for rough surface.
4. To study the bubble dynamics of water during pool boiling on rough surface and microchannel geometries for steady as well as quasi-steady heat supply.
5. To predict the bubble departure diameter for rough surface and microchannel geometries by force balance approach.

CHAPTER 3

EXPERIMENTATION

3.1 PREPARATION OF TEST SAMPLES

The top surface of six samples is polished by the 2000 grit sandpaper to remove the contamination and to obtain uniform surface finishing. Later, samples of different surface roughness are prepared by polishing each sample by different grit sandpaper viz. 1200, 800, 600, 120, 80, and 60 in a single direction which forms the unidirectional scratches. The number of stroke during the polishing is gradually increased from 5 for 60 grit sandpaper to 50 for 1200 grit sandpaper. Uniform pressure and continuous distilled water supply on the polishing surface are maintained during sample preparation. After polishing, all samples are sequentially cleaned in acetone, ethanol, and distilled water. Three samples of microchannel geometry having different profiles viz. square, parabolic and stepped are fabricated on the top circular surface of the test sample by VMC machining. The square channel is modified into parabolic and stepped microchannel keeping channel base width same. The channel top width of parabolic and stepped profile is selected in such a way that the number of channels of all the geometries is same. To study the sole effect of channel profile, the depth of the channel is also maintained same.

3.2 CHARACTERIZATION

The samples are characterized by roughness and wettability measurement in two steps, namely, before and after the boiling test. The roughness parameter is measured using roughness tester (Mitutoyo). Each sample is tested at six different locations where unidirectional scratches are perpendicular to the direction of the testing probe. The evaluation length is 4 mm. The uniformity of the roughness values is ensured over the entire surface by permitting $\pm 0.1 \mu m$ variation in the readings of six different locations. The pattern of unidirectional scratches obtained after polishing by different grit sandpaper is shown in Figure 3.1. The average of roughness parameter obtained before

and after the boiling test is tabulated in Table 3.1. It is found that the roughness parameters R_a and R_q have approximately increased by 0.1 μm after the boiling experiments. The static contact angle of the 10 μl water droplet for each sample is measured using goniometer (GBX Digidrop). The contact angle is measured by positioning the unidirectional scratches parallel and perpendicular to the axis of the camera. Figure 3.2 illustrates the method of contact angle measurement. The test is conducted two times i.e. before and after the boiling experiments. Thus the average of four contact angle values corresponding to each sample is considered in the present work.

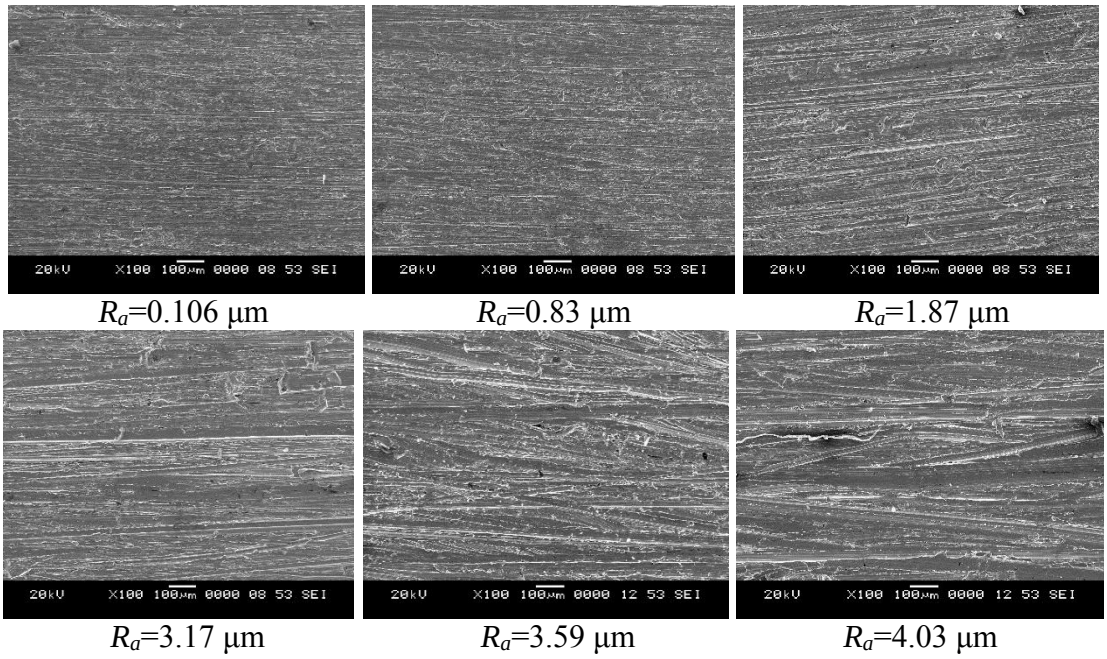

Figure 3.1 Unidirectional scratches on the samples

Table 3.1 Roughness parameters in μm

R_a	R_z	R_q	S_m
0.106	1.20	0.14	13.2
0.83	7.05	1.07	26.8
1.87	13.30	2.40	35.7
3.17	22.91	4.12	42.2
3.59	27.55	4.09	44.8
4.03	26.50	4.95	45.2

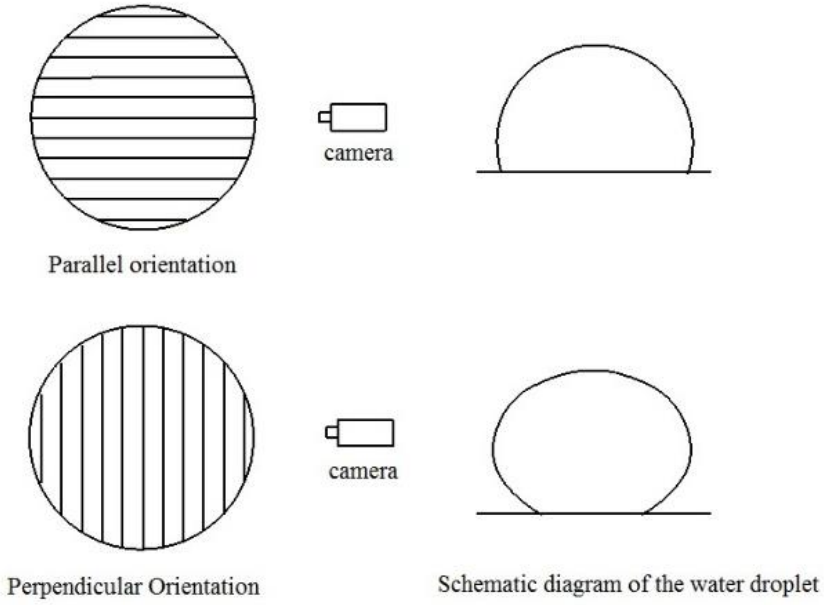

Figure 3.2 Contact angle measurement

The dimensions of the channel height, channel base width, channel top width, number of channel and fin tip thickness are tabulated in Table 3.2. The nomenclature of these microchannels (e.g. SM-1.0) is chosen so as to manifest the type of the microchannel and the geometry parameter-β. The ratio of channel top width (or channel mouth size) to channel base width (β) for the square microchannel (SM-1.0) is unity whereas parabolic (PM-1.6) and stepped microchannels (SM-1.6) are tested for β=1.6 keeping the channel height constant at 500 μm. Scanning Electron Microscope (SEM) images are shown in Figure 3.3 for better understanding of the difference in microchannel profile.

Table 3.2 Dimensions of Microchannel Geometries

Test sample	Type	Channel base width, W_b (μm)	Channel top width, W_t (μm)	Channel height, C_h (μm)	Fin tip thickness, f_t (μm)	No of channel	Ratio channel top to base width (β)
SM-1.0	Square	500	500	500	500	9	1.0
PM-1.6	Parabolic	500	800	500	200	9	1.6
SM-1.6	Stepped	500	800	500	200	9	1.6

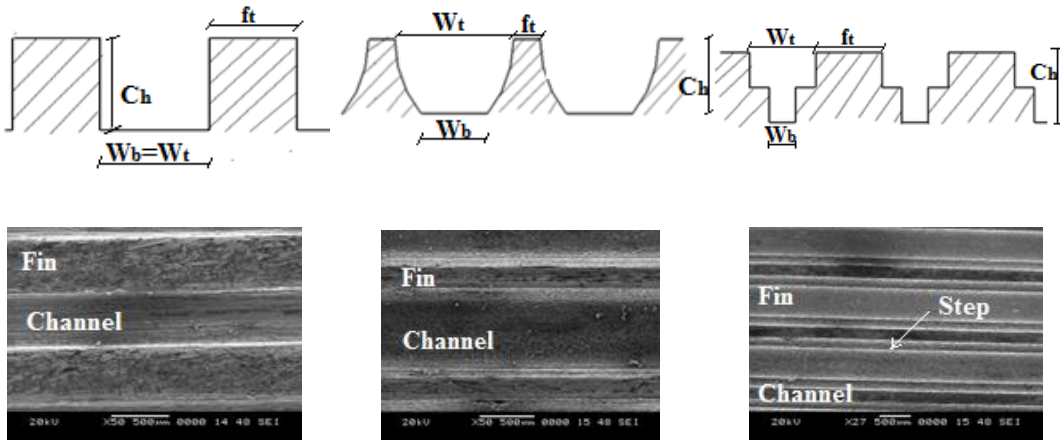

(a) Square microchannel (b) Parabolic microchannel (c) Stepped microchannel

Figure 3.3 Microchannel Geometries

3.3 EXPERIMENTAL SETUP

The experimental setup, as shown in Figure 3.4 mainly includes a boiling chamber, test section, condenser unit, and CCD camera. The rectangular chamber has removable top and bottom flanges. The condenser coil is fixed to the top flange. A K-type thermocouple and a pressure transducer are fixed to the boiling chamber to measure the bulk fluid temperature (T_f) and chamber pressure, respectively. A closed-loop system of the cooling water pump, pressure transducer and a proportional integral derivative (PID) pressure controller is used to maintain the constant pressure in the chamber. Pump circulates the cooling water through the condenser coil according to the signal of PID. The test section is inserted through the bottom flange. Auxiliary heaters of 2000W capacity are used to maintain the saturated condition of the distilled water. The transparent toughened borosilicate glass watch windows of 115 mm diameter and 15

mm thickness are provided to the wall of boiling chamber to conduct the visualization study by high speed camera. The setup is integrated with NI-9213 temperature module and NI-9264 to acquire temperature readings and to interface the computer with power supply, respectively.

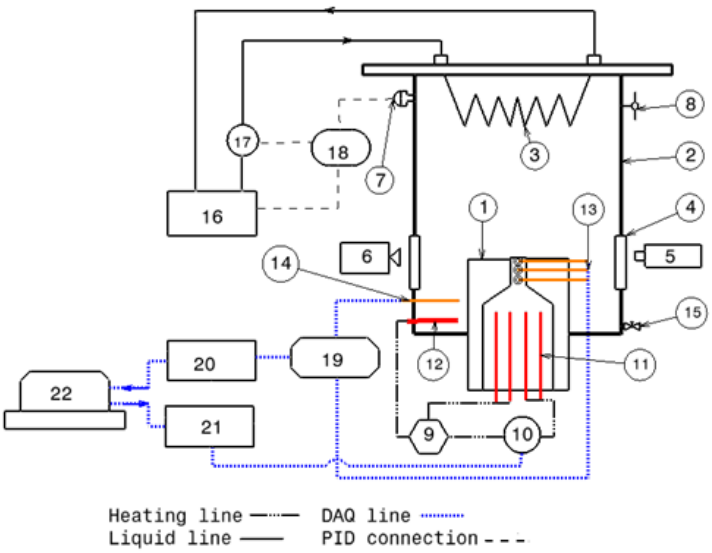

1	Test Section
2	Boiling chamber
3	Condenser coil
4	Sight glass
5	CCD camera
6	Light source
7	Pressure sensor
8	PRV
9	Mains supply
10	Programmable Power supply
11	Main cartridge heater
12	Auxiliary heater
13	Test section thermocouple
14	Bulk fluid thermocouple
15	Drain
16	Water tank
17	Pump
18	PID
19	NI 9213
20	cDaq-9178
21	NI 9264
22	Workstation

Figure 3.4 Schematic diagram of experimental setup

3.4 TEST SECTION

The details of test section assembly are given in Figure 3.5. The high density cartridge heater of 1500 W capacity is inserted in the conical copper heating block. The copper test sample of 20 mm diameter and 20 mm length is fixed on the heating block with the threaded joint. Though the sample can be fixed on the heating block with perfect surface contact, thin layer of thermal paste is applied to eliminate the air gap. The assembly of test sample and heating block is perfectly insulated with glass wool bed. Glass wool bed is covered with thick Teflon block. An O-ring and high-temperature non-corrosive RTV silicone gasket are used between the test sample and insulation block to prevent leakage and to avoid edge effect during the boiling test. K-type sheathed thermocouples of 1 mm diameter are used to measure the temperature of the test sample at different

locations. The thermocouples are implanted in the test sample at 2 mm, 6 mm, and 10 mm from the top surface and the temperatures T_{m-1}, T_m, and T_{m+1} correspond to these thermocouple readings, respectively.

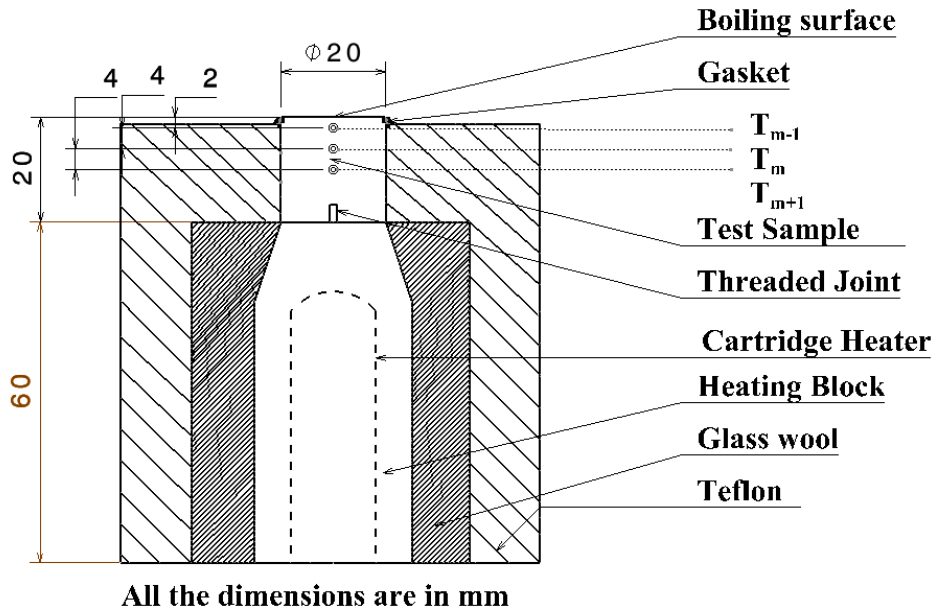

Figure 3.5 Test Section

Table 3.3 summaries the operating conditions of the present work**.** The details of instrument and equipment used in the experiment are given in Table 3.4.

Table 3.3 Operating conditions in the present experiment

Parameter	Value
Pressure (bar)	1, 5, 10
Exponential heating period (min)	10
Time constant	1, 2, 3, 4, 5, 6

Table 3.4 Instruments and equipment used in the present experiment

Instrument/Equipment	Specifications
K-type thermocouple (3 no's)	Range: -20°C to 400°C Sheath length: 20 mm Sheath diameter: 1 mm Type: Ungrounded
Main Cartridge heater (4 no's)	Diameter: 7 mm Length: 50 mm Capacity: 375 W
Auxiliary Heater (2 no's)	Diameter: 16 mm Length: 150 mm Capacity: 1000 W
Pressure transducer	Range: 1 bar to 27.4 bar Operating temperature: upto 228°C
Programmable power supply	Model: Sorenson XG series Range: 670 W to 1700 W Signal: DC voltage controlled-voltage analog programming

3.5 EXPERIMENTAL PROCEDURE

The known quantity of DI water is filled in the boiling chamber during each trial. DI water is rigorously boiled before each trial by the auxiliary heater to remove the dissolved gases. For steady-state pool boiling study, heat is supplied in incremental order. When the system reaches to the steady-state, the thermocouple readings are recorded. For transient pool boiling study, controlled analog signals are generated through NI-9264 which is monitored by LABVIEW program. Thus exponentially varying voltage controlled-current signals are supplied to the main heaters through the programmable DC power supply (Sorensen; XG series). The time-variant exponential heat is supplied where time constant varies from $\gamma=1$ to $\gamma=6$. The period of exponential transient (t) is 10 min. The time constant is calculated as $\gamma=t/\tau$ where τ is exponential period. The LABVIEW program is also designed for recording the temperatures of the

test piece at an acquisition rate of 5 samples/sec by a NI-9213 temperature module through cDaq-9178. The heat supply, temperature acquisition and the high speed camera are synchronized through workstation. The pressure in the chamber is controlled by a proportional integral derivative (PID) pressure controller. Pressure transducer synchronized with PID permits ±0.01 bar pressure variation during the trial.

The steps followed during experiments are listed below:

i. Fill 10 litres of distilled water in the boiling chamber and boil it for 30 mins before each trial.
ii. Make the connection between PID, pressure transducer and pump.
iii. Connect the pump to the water tank and thereafter, connect the condenser coil to the pump.
iv. Connect the thermocouples and programmable power supply to the data acquisition system.
v. Place the high speed camera in front of watch window and place the monochromatic light source to the opposite watch window.
vi. During steady-state experiments, supply incremental heat of 10 W at each step and observe the temperature of the sample. When steady-state is achieved in the each temperature, record the video as well as temperature readings.
vii. Repeat the procedure mentioned in step-vi for different pressures using different samples.
viii. During transient experiments, set the time constant value in the LABVIEW program. Synchronize the high speed camera with the power supply unit in such way that one button click will record the video as well as acquire the temperature readings.
ix. Clean the sample in dilute acetic acid and ethanol after each set of trial.
x. Repeat the procedure mentioned in step-viii for different time constant values and for different pressures with different samples.

3.6 DATA REDUCTION

The main heater and test sample are considered as the axisymmetric system. As the surface properties are found to be uniform during characterization, the heat flux from the top surface of the test sample is assumed to be uniform. The heat flux dissipated to the boiling fluid and the surface temperature can be estimated by the thermocouple readings. The temperature distribution along the length of the test sample of R_a=3.59 μm at P=5 bar and γ=3, shown in Figure 3.6, is obtained by thermocouples which are implanted at 2 mm, 6 mm and 10 mm from the boiling surface. Though the temperature distribution at all the time intervals are not perfectly linear ($R^2 \neq 1$), a linear fit is established. This non-linearity exists due to temperature maldistribution close to boiling surface during nucleate boiling. Gong and Cheng (2017), investigated such temperature maldistribution based on pseudo-potential liquid-vapor phase change lattice Boltzmann model. They found that the depth of penetration of such maldistribution during transition regime is three times the capillary length. The isotherm located in this depth does not appear straight horizontal indicating non-uniform temperature distribution. In the present study, temperature measurement by the thermocouple implanted at 2 mm from the boiling surface may get affected due to significant maldistribution during high pressure nucleate boiling.

The unsteady state heat flux from the top surface of the sample due to exponential heating is calculated by Equation (3.1).

$$q'' = -k_{Cu} \frac{T_{m-1} - T_{m+1}}{2\Delta x} \tag{3.1}$$

where Δx is the distance between two thermocouples.

The surface temperature of the sample is calculated by using Equation (3.2).

$$T_s = T_{m-1} - q'' \left(\frac{x_{m-1}}{k_{Cu}} \right) \tag{3.2}$$

where, x_{m-1} is the distance between the surface of a sample and the top thermocouple (T_{m-1}) and is equal to 2 mm, as shown in Figure 3.2.

Heat transfer coefficient (HTC) between the boiling surface and water is estimated by Equation (3.3).

$$h = \frac{q''}{(T_s - T_f)} \tag{3.3}$$

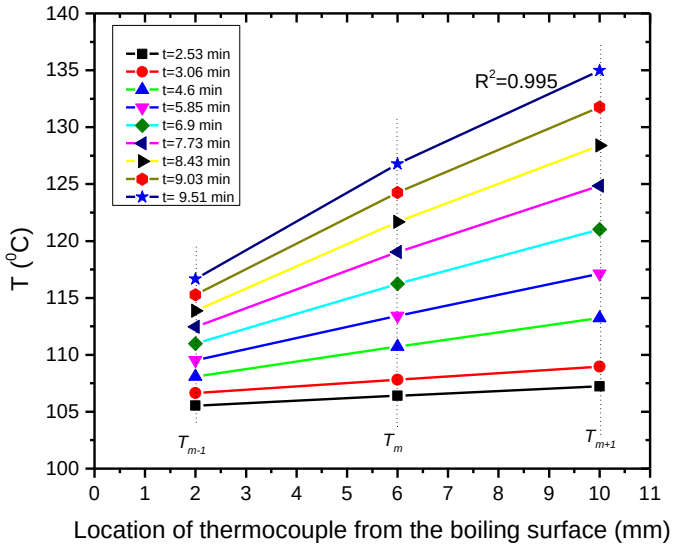

Figure 3.6 Temperature distribution along the length of sample

3.7 VISUALIZATION OF BOILING

A high speed camera (AOS Promon 501) at 1000 frames/sec with resolution of 480×240 pixel is used for visualization of pool boiling. AF NIKKOR 50mm F/1.4D lens is used. The camera is positioned in front of the sight glass. A diffused light source is placed opposite to the camera to provide uniform illumination on the test surface. Promon studio viewer software interfaces the camera with PC. This software is used to control triggering and recording the videos and it is also used to set the shutter speed, pixel size, and frame rate of the videos to be captured. These recorded sequences are marked as per the requirement and converted into images. These images are processed in MATLAB image processing tool to measure the horizontal (*a*) and vertical dimension (*b*) of the bubble meniscus in terms of pixels. The actual value of *a* and *b* is obtained, as given in Equation (3.4-a), by the knowledge known size of object and its corresponding pixels.

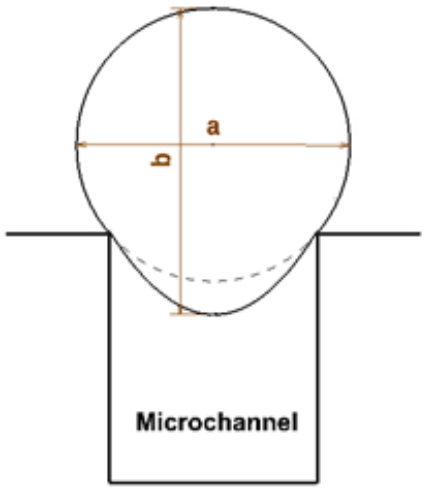

Figure 3.7 Measurement of bubble departure diameter

The spherical shape of the bubble slightly turns to elliptical profile at its bottom as shown in Figure 3.7. This bubble behaviour is identical for all type of samples viz. smooth, rough and microchannel. Thus measurement of the bubble departure diameter requires certain assumption to obtain the equivalent bubble diameter. As suggested by Siegel and Keshock (1964) the bubble departure diameter (D_b) is estimated as the arithmetic mean of *a* and *b*, as given in Equation (3.4-b).

$$\text{a or b} = \frac{\text{No.of pixels of captured image (p)} \times \text{Actual size of reference object (R)}}{\text{No.of pixels of reference object (N)}} \tag{3.4-a}$$

$$D_b = \frac{a+b}{2} \tag{3.4-b}$$

The number of bubbles generated and departed from the same nucleation site per second is called as bubble frequency. Bubble frequency (*f*), as given in Equation (3.5), is the reciprocal of sum of waiting period and growth period of the bubble.

$$f = \frac{1}{(t_w + t_g)} \tag{3.5}$$

Time taken by the bubble to grow from its nucleation to the departure is called growth period (t_g) and time taken for nucleation of the next bubble after the departure of preceding bubble from the same site is called waiting period (t_w). The representative

value of bubble departure diameter and bubble frequency is the average measurement of the 30 consecutive bubbles.

3.8 UNCERTAINTY

The uncertainty calculations are done by propagation of error method. The uncertainty in temperature and distance measurement is ±0.1°C and ±0.0001 m, respectively. The uncertainty in the contact angle measurement is ±1°. The uncertainty in pressure measurement is 0.2% (full span is 0-27.4 bar). The uncertainty in the measurement of bubble departure diameter is 0.05 mm. The maximum uncertainty in the bubble frequency is estimated to be 10.45%.

The uncertainty in the heat flux is calculated by using Equation (3.6). It is found that uncertainty in the heat flux exponentially drops with increase in the estimated heat flux value. Dividing these calculated values by the heat flux values yields the percentage uncertainty and it is found to be 3.81 % at high operating temperature.

$$U_{q''} = \left[\left(\frac{q''}{k_{Cu}} U_{k_{Cu}}\right)^2 + \left(\frac{k_{Cu}}{2\Delta x} U_{T_{m-1}}\right)^2 + \left(\frac{k_{Cu}}{2\Delta x} U_{T_{m+1}}\right)^2 + \left(\frac{q''}{\Delta x} U_{\Delta x}\right)^2\right]^{1/2} \tag{3.6}$$

The uncertainty in the surface temperature, obtained by Equation (3.7), varies from 0.41°C to 1.06°C throughout the experiments.

$$U_{T_s} = \left[\left(U_{T_{m-1}}\right)^2 + \left(\frac{x_{m-1}}{k_{Cu}} U_{q''}\right)^2 + \left(\frac{q''}{k_{Cu}} U_{x_{m-1}}\right)^2 + \left(\frac{q'' x_{m-1}}{{k_{Cu}}^2} U_{k_{Cu}}\right)^2\right]^{1/2} \tag{3.7}$$

The uncertainty in the HTC is calculated by using Equation (3.8) and it is found to be 11.95 % at higher operating temperature.

$$U_h = \left[\left(\frac{U_{q''}}{T_s - T_f}\right)^2 + \left(\frac{q''}{(T_s - T_f)^2} U_{T_s}\right)^2 + \left(\frac{q''}{(T_s - T_f)^2} U_{T_f}\right)^2\right]^{1/2} \tag{3.8}$$

The uncertainty in the bubble departure diameter is estimated by using Equation (3.9) and it is found to be 4.81% at higher operating temperature.

$$U_{D_b} = \frac{1}{\sqrt{2}} \times \left[\left(\frac{R}{N} U_p\right)^2 + \left(\frac{p}{N} U_R\right)^2 + \left(\frac{pR}{N^2} U_N\right)^2\right]^{1/2} \tag{3.9}$$

The uncertainty in the bubble frequency is estimated by using Equation (3.10) and it found to be 8.1% at higher operating temperature.

$$U_f = \left[\frac{\sqrt{2}}{(t_g + t_w)^2} U_t\right] \tag{3.10}$$

The uncertainties in heat flux, HTC, surface temperature, bubble departure diameter and bubble frequency for the sample of R_a=4.03 μm at 10 bar pressure are given in Appendix A.

3.9 REPEATABILITY

In order to examine the reproducibility and repeatability of the experimental data, three pre-experimental runs are taken with distilled water at atmospheric pressure for plain surface. HTC versus heat flux for these runs are plotted as shown in Figure 3.8 which confirm the repeatability of the experimental data.

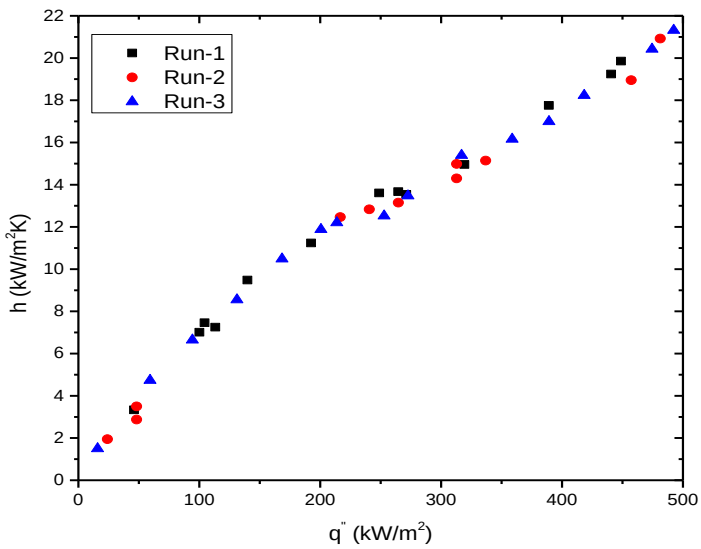

Figure 3.8 Repeatability of the experimental data

3.10 HYSTERESIS

Boiling hysteresis may exit due to activation and deactivation of nucleation sites during stages of boiling. Hysteresis effect is studied by performing boiling experiments with increasing and decreasing power supply to be called as heating and cooling, respectively. It is found in Figure 3.9 that identical boiling results are produced during heating and cooling condition.

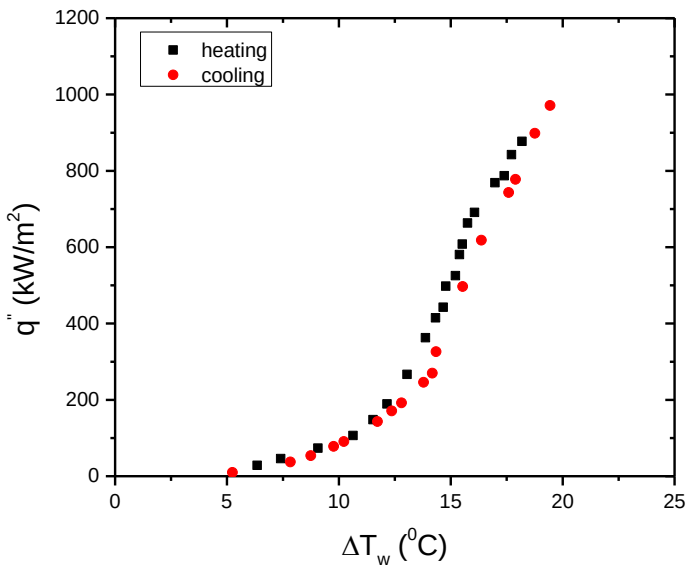

Figure 3.9 Hysteresis

CHAPTER 4

RESULTS AND DISCUSSION

Experimental results of pool boiling heat transfer (PBHT) from rough surface and microchannel geometry for steady and transient heat supply at pressure upto 10 bar are presented in this chapter. The correlation for HTC of water during exponential heat supply is developed.

4.1 SELECTION OF ROUGHNESS PARAMETER

R_a is the arithmetic average value of roughness profile, determined from the deviations of peaks and valleys about the mean line within the evaluation length. It is the integral of the absolute height of the peaks and valleys over the evaluation length. Thus R_a neutralizes the extreme peak or valley. R_z is the average of only five highest peaks and five deepest valleys within sampling length. Furthermore, the wavelength of the scratches that can be called as mean spacing between capillary tubes (S_m), is also measured. It is clear that R_a fails to distinguish between two surfaces of different topography. On the other hand, though R_z accounts to the peak to valley distance, the considered samples are just five. Thus to characterize the large flat surface, R_z does not fit as a better measure. In this work, unidirectional scratches are made on the sample where each scratch is assumed as a capillary tube. Thus equivalence between radius of the tube and R_a is considered. Further the number of capillary tubes can be related to the mean spacing S_m. Thus R_a and S_m are taken into account and their combined role in pool boiling heat transfer is discussed in the present study where the term R_a is used for classification of the tested samples. This assumption seems most suitable than considering R_z. Though R_a and S_m are considered as roughness parameters in this study, role of R_z in the pool boiling heat transfer can not be neglected.

4.2 EFFECT OF UNIDIRECTIONAL SCRATCHES ON THE WETTABILITY

The variation of the measured static contact angle with R_a before and after the boiling test by positioning unidirectional scratches parallel and perpendicular to the axis of the camera is given in Figure 4.1 and for better understanding, images captured for the test sample of R_a=3.17 μm during contact angale measurement are shown in Figure 4.2 as an example.

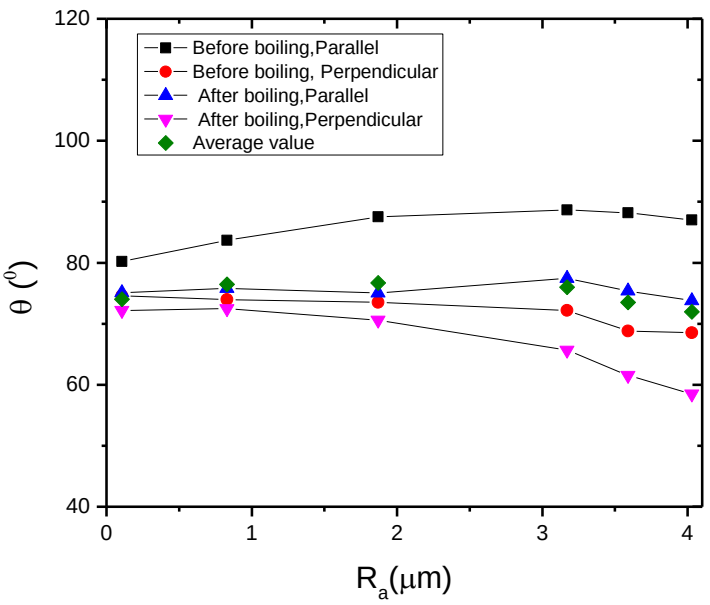

Figure 4.1 Variation of static contact angle with R_a

For both the tests, i.e. before and after boiling, the contact angle found to be decreased with increase in R_a. Capillary wicking through the unidirectional scratches becomes dominant with an increase in the surface roughness, which results in the drop in the contact angle. Bubble spreading through the scratches can be clearly observed by the perpendicular orientation of the camera with the scratches. Hence, the measured contact angle when camera is placed perpendicular to the unidirectional scratches is lower than the one measured by positioning camera parallel to the scratches. It is also noticed that mean spacing (S_m) of the scratches increases with increase in R_a. SEM images of the

samples shown in Figure 4.3 are taken to observe the modification in the surface structure after boiling test.

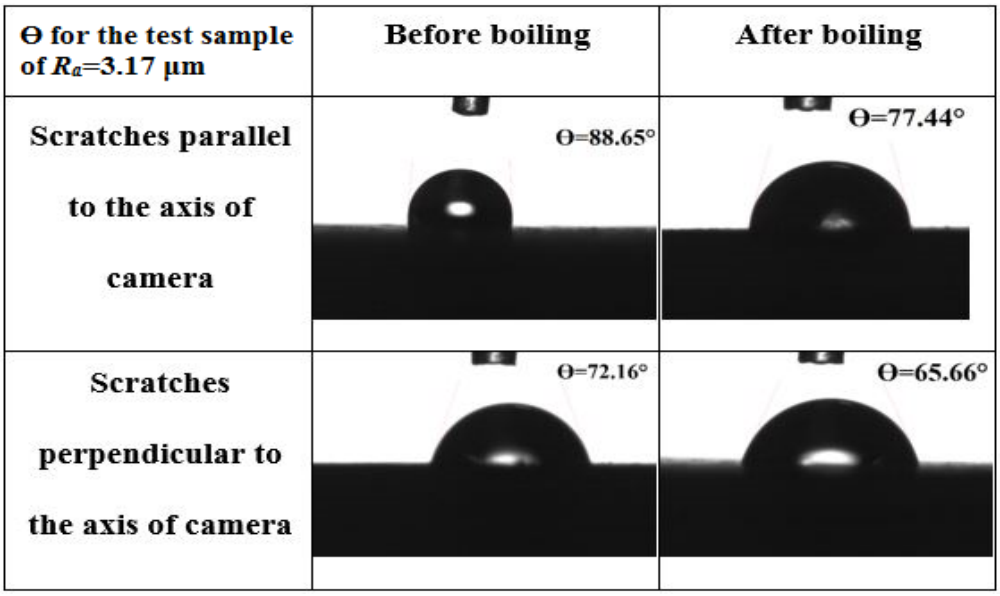

Figure 4.2 Contact angle measurement for the sample of R_a=3.17 µm

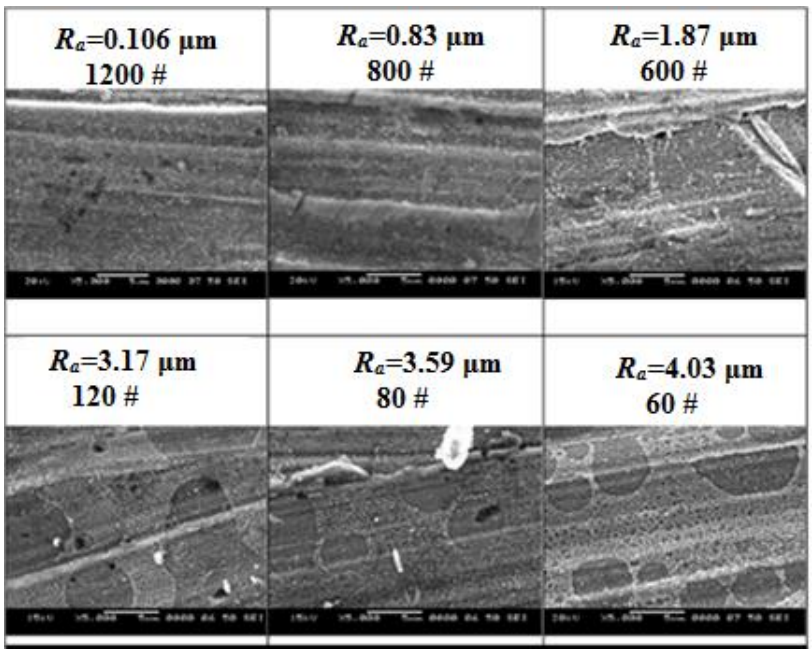

Figure 4.3 SEM of the polished surfaces after boiling

It is observed from SEM imaging that the nano-porous copper oxide layer has formed on the surface of higher roughness value (R_a ≥3.17 μm) after boiling experiments at high temperature. The identical surface oxidation of stainless steel and copper rodlets during transient heat transfer is reported by Lee et al. (2014). The entrapped air in the irregularities of highly rough surface resulted in the formation of the oxide layer. Hence, it is found that contact angle drops remarkably after boiling experiment. The average of four readings of contact angle corresponding to each surface roughness is considered for further study.

4.3 VALIDATION OF EXPERIMENTAL RESULTS

Several correlations for pool boiling HTC have been proposed over the past decades. Some of them are developed based on theoretical approach whereas few use empirical factors to account for the surface-fluid combination. Few are also based on thermo-physical properties of the working fluid and surface characteristics of the boiling surface. Typical selection of the correlation for heat transfer coefficient is done to validate the present experimental results. Correlations of Mostinski (1963), Cooper (1984), Nishikawa et al. (1982) and Gorenflo (1997) are found to be the most suitable as they do not require the experimental data as an input for the prediction of HTC. These correlation are given in Table 4.1.

Table 4.1 Existing correlation for HTC

Author	Correlation
Mostinski (1963)	$h = 0.00417 \times q^{0.7} P_c^{0.69} F_{PF}$ where, $F_{PF} = 1.8 \times P_r^{0.17} + 4 \times P_r^{1.2} + 10 \times P_r^{10}$
Cooper (1984)	$h = 55 \times p_r^{0.12-0.2\ \ln R_p} (-0.4343 \ln p_r)^{-0.55} M^{-0.5} q^{0.67}$
Nishikawa et al. (1982)	$h = \frac{31.4\, P_c^{0.2}}{M^{0.1}\, T_c^{0.9}} \left(8R_p\right)^{0.2(1-p_r)} \frac{p_r^{0.23}}{[1 - 0.99\,(p_r)]^{0.9}} q^{0.8}$
Gorenflo (1997)	$h = h' \times F_P \times F_q \times F_R$ where, $F_P = 1.73 P_r^{\ 0.27} + \left(6.1 + \frac{0.68}{1-P_r}\right) P_r^{\ 2}$; $F_q = \left(\frac{q}{q'}\right)^n$; $n = 0.9 - 0.3 P_r^{\ 0.15}$; $F_R = \left(\frac{R_a}{R_{a0}}\right)^{0.133}$

The present experimental results of HTC of water for smooth surface (R_a=0.106 μm) at P=10 bar and rough surface (R_a=3.17 μm) at pressure P=5 bar are compared with the predicted values as shown in Figure 4.4 and Figure 4.5, respectively.

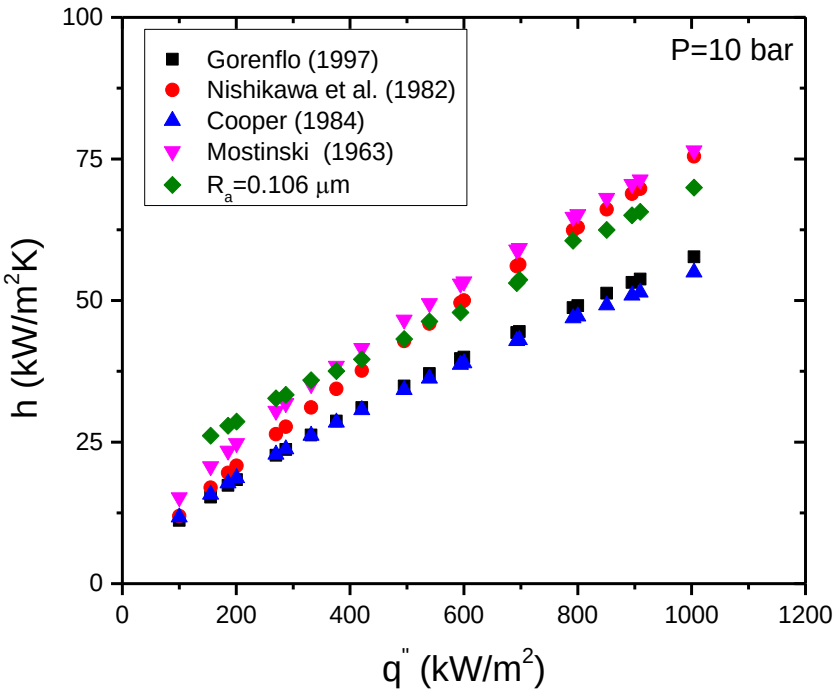

Figure 4.4 Validation of experimental results of R_a=0.106 μm at P=10 bar

Table 4.2 Comparison between experimental and predicted HTC

Correlation	MAE	
	R_a=0.106 μm, P= 10 bar	**R_a=3.17 μm, P= 5 bar**
Mostinski (1963)	8.99	36.69
Cooper (1984)	23.40	19.41
Nishikawa et al. (1982)	17.35	24.28
Gorenflo (1997)	24.59	22.90

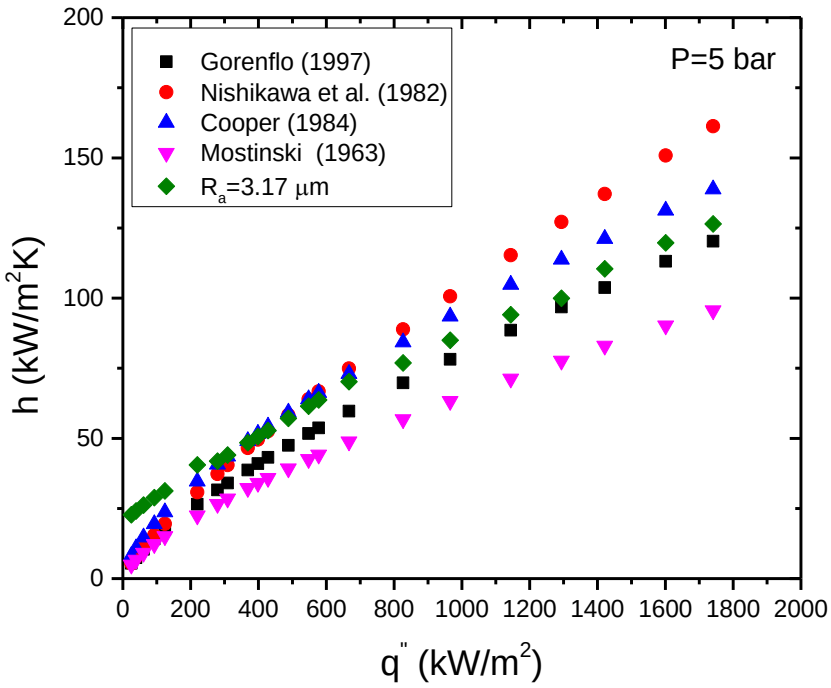

Figure 4.5 Validation of experimental results of R_a=3.17 µm at P=5 bar

$$MAE = \frac{1}{n}\sum \frac{\left|HTC_{pred} - HTC_{b_{exp}}\right|}{HTC_{exp}} \times 100 \qquad \textbf{(4.1)}$$

The mean absolute error (MAE) between the experimental HTC and predicted HTC by the correlations is calculated by Equation (4.1) and tabulated in Table 4.2. It is found that Mostinski (1963) correlation predicts the HTC in good agreement only for smooth surface even at high pressure as it does not account for the surface roughness value. Moreover, measured HTC values are in good agreement with the predicted values by Cooper (1984), Nishikawa et al. (1982) and Gorenflo (1997) correlations. The comparison between experimental and predicted HTC for the samples of different R_a upto 10 bar pressure is given in Figure B.1(a-d) of Appendix B.

4.4 EFFECT OF STATE OF HEATING ON POOL BOILING HEAT TRANSFER

The systematic study is carried out to examine the effect of state of heating viz. steady and transient on PBHT. Steady-state study comprises of an incremental heat supply at a certain time interval ensuring the steady state condition of the sample temperature. Transient state is maintained by supplying exponential heat at different rate. γ=1 and γ=6 imply quasi-steady and rapid heat supply, respectively. Figure 4.6 shows the boiling curve of the smooth surface of R_a=0.106 μm for steady, quasi-steady and rapid heat supply at P=1 bar. The mechanism of the bubble formation during steady-state heat supply is found to be progressive where nucleation sites get activated gradually with increase in the incremental heat supply. The stable bubble growth allows sufficient time for the liquid replenishment. As the mechanism of the liquid replenishment does not affect adversely, the fully developed nucleate boiling (FDNB) regime i.e. point B to point C, as shown in Figure 4.6, is found to be prolonged.

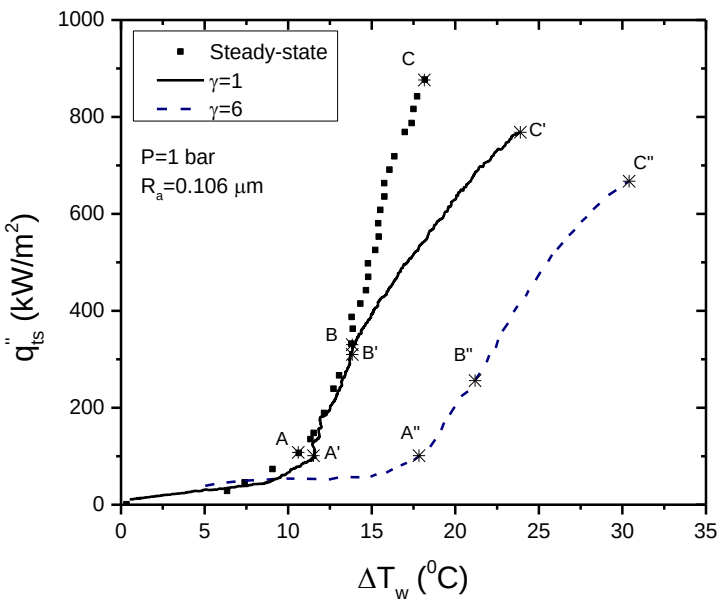

Figure 4.6 Boiling curves at steady-state heat supply, quasi-steady (γ=1) and rapid (γ=6) exponential heat supply

The boiling regime from non-boiling to the film boiling are carefully noticed during quasi-steady and rapid exponential heat supply. Non-boiling phase turns to nucleate boiling at point $A^{'}$ and point $A^{''}$ during quasi-steady and rapid exponential heat supply, respectively, as shown in Figure 4.6. It is found that the transition from non-boiling regime to boiling regime substantially depends on the rate of exponential heat supply. For quasi-steady heat supply of γ=1 which has long heating period, nucleation occurs at lower wall superheat (point $A^{'}$) compared to that for rapid heat supply of γ=6 with short period (point $A^{''}$). The boiling phase of $A^{'}$-$B^{'}$ is able to extract the heat from the sample surface as efficiently as that of steady-state and thus it follows the steady-state curve upto point $B^{'}$. The stored energy in the sample continuously increases due to exponentially increasing heat supply. The entire surface gets covered with the discrete bubble and thus FDNB phase begins at point $B^{'}$ and $B^{''}$ for quasi-steady and rapid transient, respectively. As commented by Sakurai et al. (1992), during quasi-steady heat supply, HSN occurs at less number of nucleation sites which result in the gradual levitation of the superheated liquid from the boiling surface. Small number of detached bubbles cause mixing of the superheated liquid with the bulk fluid and will activate the remaining originally flooded cavities. This entire process occurs slowly and hence wall superheat increases gradually with the increase in the heat flux during heat supply of γ=1. Rapid increase in the surface temperature during exponential heat supply leads to an instability in the liquid-vapor motion and thus, liquid supply to the dry-out area becomes inefficient. Early bubble coalescence is observed during which bubble begins to spread horizontally on the surface. This mechanism of bubble growth degrades the heat dissipation from the surface which results in the increase in the wall superheat. Finally, transition into film boiling regime occurs at point $C^{'}$ and $C^{''}$ for quasi-steady and rapid transient, respectively, where vertical and horizontal bubble coalescence forms vapor film on the entire surface.

4.5 EFFECT OF SURFACE MODIFICATION ON POOL BOILING HEAT TRANSFER

Boiling experiments are conducted on the characterized samples having a wide range of R_a with steady state and exponentially varying heat supply. The surface roughness

value of unidirectional scratches is varied from R_a=0.106 μm to R_a=4.03 μm. Program controlled quasi-steady heat is supplied at γ=1 for long period of transient whereas rapid heat is supplied at γ=6 for short period of transient, thus γ is varied from 1 to 6. The trials are conducted at 1 bar, 5 bar and 10 bar pressures. The boiling curves for the rough samples obtained during steady-state heat supply at P=1 bar are plotted in Figure 4.7. The boiling curves for the rough samples obtained at pressure upto 10 bar at steady-state condition are given in Figure B.2 (a-b) of Appendix B.

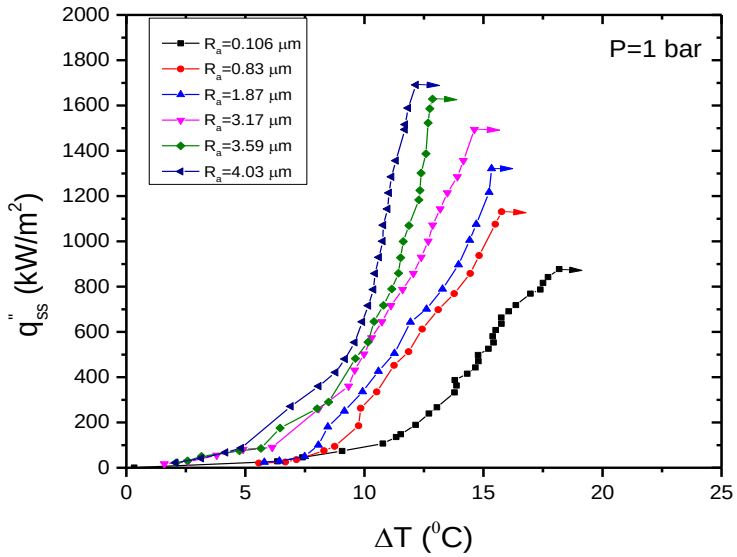

Figure 4.7 Effect of surface roughness on pool boiling heat transfer during steady-state heat supply

The variation in the pool boiling heat transfer with the wall superheat during exponential heat supply at P=1 bar and γ=2 is shown in Figure 4.8. The boiling curves for the rough samples obtained at pressure upto 10 bar at transient condition are given in Figure B.3 (a-q) of Appendix B.

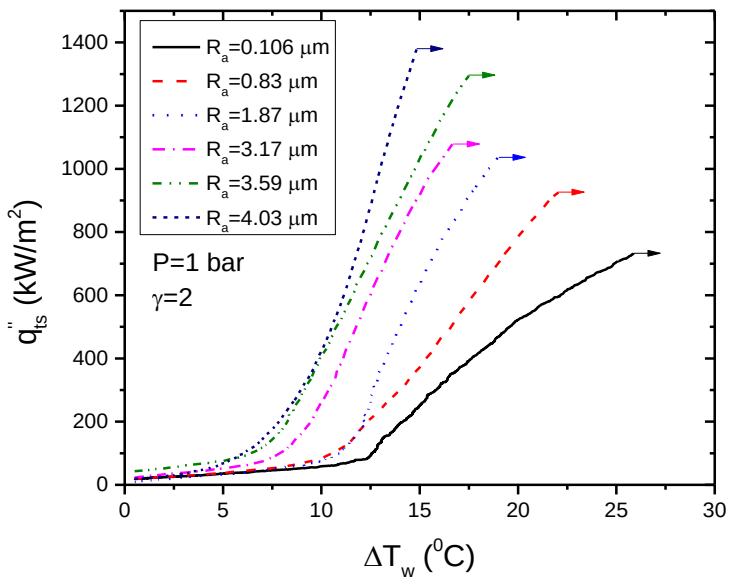

Figure 4.8 Effect of surface roughness on pool boiling heat transfer during exponential heat supply

It is clearly observed from Figure 4.7 and Figure 4.8 that boiling curve of the sample moves to the left with increase in R_a indicating enhanced heat transfer with increase in the surface roughness. The reduced wall superheat at certain heat flux value with increase in R_a also implies the increase in the heat transfer coefficient. The unidirectional scratches act as narrow passages for the liquid supply to the nucleation sites. Liquid replenishment improved due to capillary action through the scratches. The absolute depth R_z plays vital role in boiling incipience. It is observed during characterization that R_z increases with increase in R_a. Thus the increase in the cavities on the surface results in early boiling incipience. It also results in the increase in nucleation sites density. This characteristics of unidirectional scratches enhances the heat transfer. Figure 4.9 and Figure 4.10 show the comparison of boiling curves for plain surface and different microchannel geometries for steady and transient heat supply, respectively. All the tested microchannel geometries have augmented steady as well as transient heat transfer. It is observed that modification of the square channel (SM-1.0) into the parabolic (PM-1.6) and stepped channel (SM-1.6) has remarkably increased the heat transfer. The augmentation in the heat transfer may be the

consequence of enhanced microlayer evaporation, increased bubble diameter and improved bubble frequency. The boiling curves for the microchannel geometries obtained at pressure upto 10 bar are given in Figure B.4 (a-c) of Appendix B.

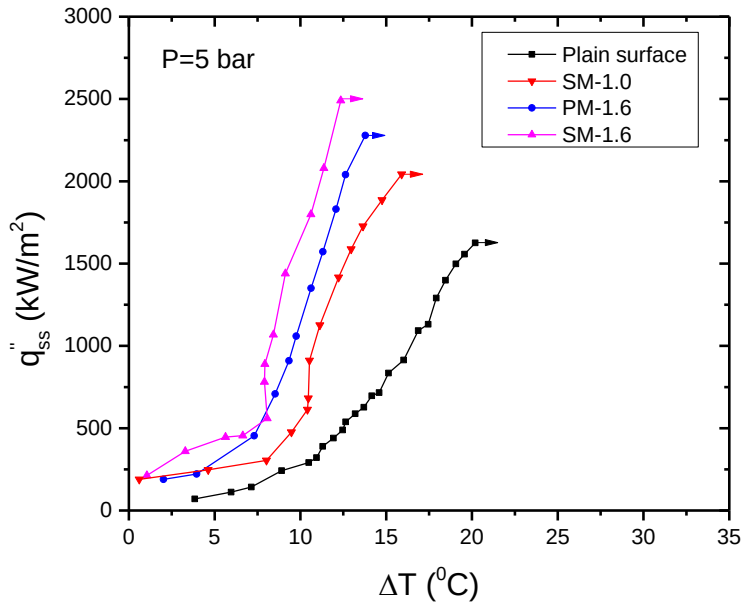

Figure 4.9 Boiling curve of microchannel geometries during steady-state heat supply

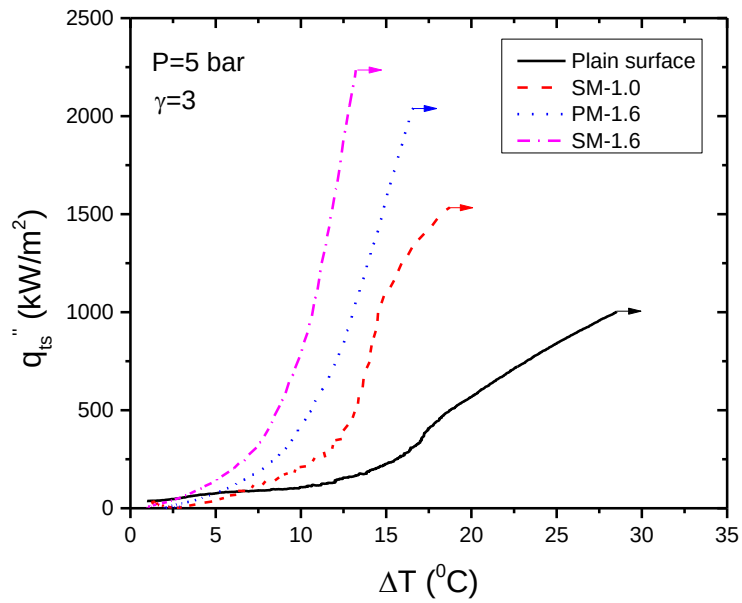

Figure 4.10 Boiling curve of microchannel geometries during exponential heat supply

4.6 EFFECT OF TIME CONSTANT ON TRANSIENT POOL BOILING HEAT TRANSFER

The exponential heat is supplied to the sample at time constant γ varying from 1 to 6 at different pressures. Figure 4.11 and Figure 4.12 depict the effect of γ on pool boiling heat transfer from rough surface and microchannel geometry, respectively. It is found that time constant γ affects the boiling process adversely irrespective of the surface characteristics and system pressure. Boiling curve shifts towards right with increase in γ which suggests that heat transfer decreases with increase in γ. The rapidly increasing heat supply during short period ($\gamma=6$) triggers the bubble nucleation. The bubble waiting period and growth period reduce remarkably. The number of complete bubble cycles that can be possible at each nucleation site reduces with increase in the rate of heating. Insufficient liquid supply to the nucleation sites leads to the horizontal spreading of the bubble. Thus the FDNB regime drastically reduces with increase in the rate of heating. Due to rapid rise in the surface temperature, wall superheat increased.

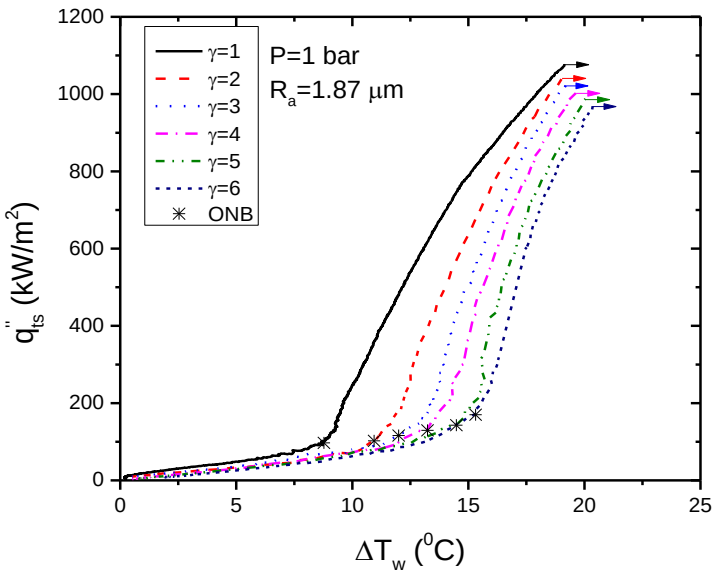

Figure 4.11 Boiling curves of the sample of R_a=1.87 μm at P=1 bar for different γ

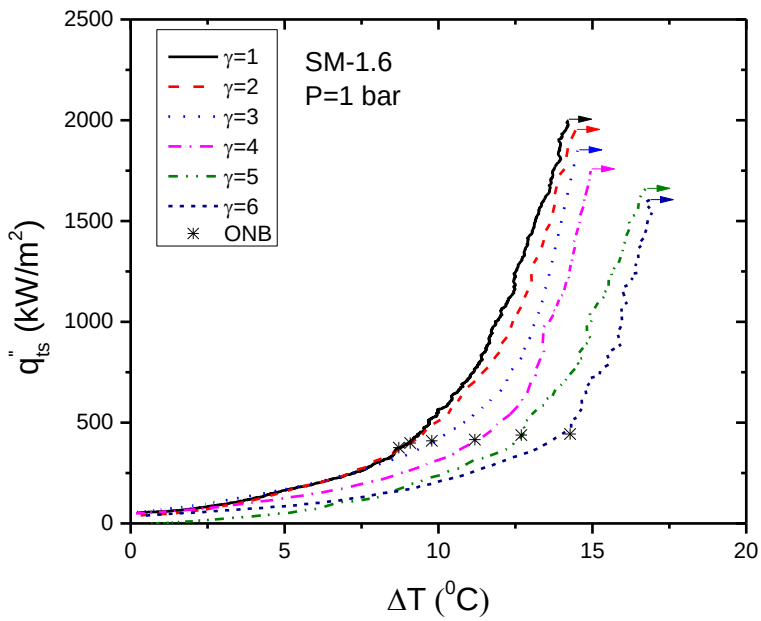

Figure 4.12 Boiling curves of SM-1.6 at P=5 bar for different γ

It is also noticed that ONB heat flux and ONB temperature increase with increase in the time constant. Similar results are reported by Sakurai et al. (2000) and Su et al. (2016). They suggested that the variation in ONB temperature can be estimated by a combination of the analytic transient conduction temperature profile in water and the Hsu's nucleation criterion. It is observed during the trial at P=1 bar on the sample of R_a=1.87 μm that ONB temperature during heat supply at γ=2, γ=3, γ=4, γ=5 and γ=6 increased by 24.34%, 34.40%, 50.51%, 64.73% and 74.18%, respectively, from that of γ=1. Boiling curves for the SM-1.0 at pressure upto 10 bar at different time constant are given in Figure B.5 (a-c) of Appendix B.

4.7 EFFECT OF PRESSURE ON POOL BOILING HEAT TRANSFER

The pool boiling tests are conducted at 1, 5 and 10 bar pressures on each sample for steady and exponential heat supply. It is found that both, steady and transient heat transfer from the sample substantially increased with increase in the pressure as shown in Figure 4.13 (a) and (b). Points A, $A^{'}$ and $A^{''}$ marked on the boiling curves represent the ONB point at P=1 bar, 5 bar and 10 bar, respectively, for steady and quasi-steady

exponential heat supply (γ=1). The ONB temperature reduced with increase in the pressure. Rate of heat transfer immediately after the spontaneous nucleation also increased with increase in the pressure. Synchronization of the high speed camera and the data acquisition system helped to identify the different regime of the boiling. The partial nucleate boiling regime turns into FDNB regime at point *B*, $B^{'}$ and $B^{''}$ at P=1 bar, 5 bar and 10 bar, respectively. It is noticed that the nucleate boiling regime extends with increase in pressure irrespective of the state of heating. The transition from boiling regime to film boiling regime is widely classified as steady, quasi-steady semi-direct and direct transitions on the basis of period of FDNB regime. The steady and direct transitions are observed in the present study for the slow and rapid exponential heat supply, respectively. The transition mechanism also varies with the system pressure. At P=1 bar and 5 bar, semi-direct transition is noticed at point *C* and $C^{'}$, respectively, whereas at P=10 bar, quasi-steady transition is noticed at point $C^{''}$. During visualization, it is found that tiny bubbles are formed and depart independently at high pressure and hence bubble coalescence is retarded resulting in drastic increase in the heat transfer compared to 1 bar pressure.

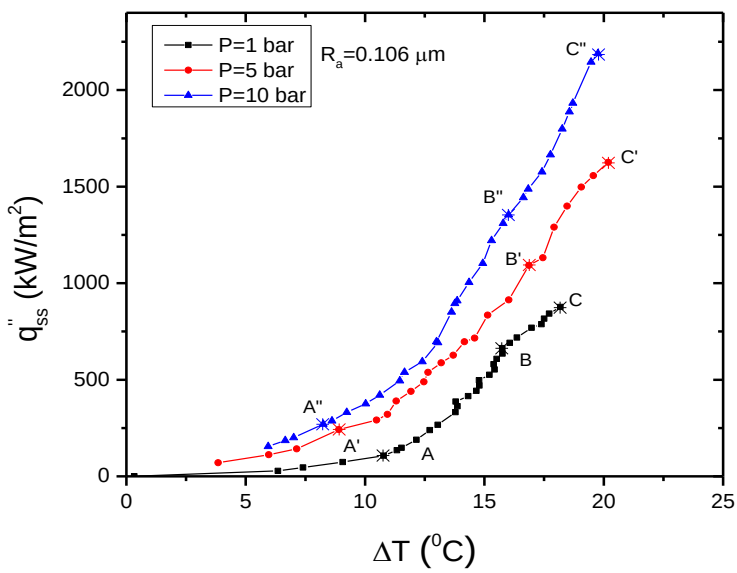

(a)

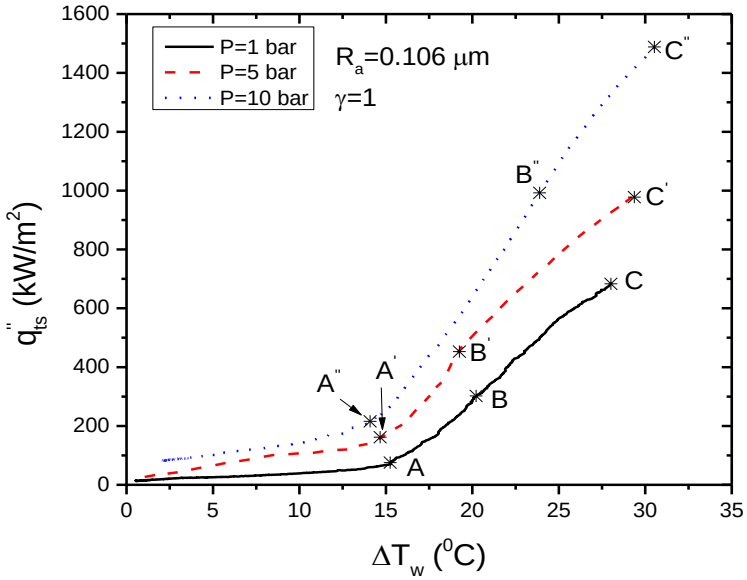

(b)

Figure 4.13 Boiling curves of the sample R_a=0.106 μm at (a) steady-state and (b) γ=1 at different pressures

4.8 ONSET OF NUCLEATE BOILING AND OVERSHOOT TEMPERATURE

High speed camera, programmable power supply and data acquisition system are synchronized with the workstation. This ensures the physical identification of the exact moment of ONB and the temperature recorded corresponding to that moment can be identified through the common platform of LABVIEW program. The influence of state of heating viz. steady and quasi-steady exponential heat supply on ONB temperature for sample of different roughness is shown in Figure 4.14. It is noticed that the ONB temperature decreases remarkably with increase in the surface roughness for both the states of heating. It is noted that the ONB temperature increased during exponential heat supply compared to that of steady-state supply. It is observed that during quasi-steady exponential heat supply (γ=1), the ONB temperature of R_a=0.106 μm, R_a=0.83 μm, R_a=1.87 μm, R_a=3.17 μm, R_a=3.59 μm and R_a=4.03 μm has increased by 3.9%, 6.9%, 17.58%, 32.4%, 24.55%, and 15.32%, respectively, from corresponding steady-state ONB temperature.

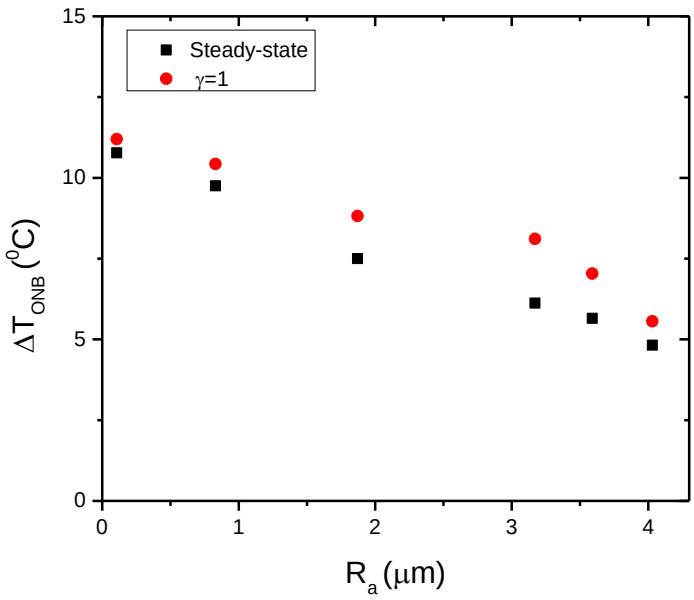

Figure 4.14 Influence of state of heating on ONB temperature

Figure 4.15 shows the variation in ONB temperature with γ as well as with R_a at P=1 bar. The ONB temperature increased with increase in the time constant, however, it decreases with increase in R_a. Even though during transient heating the nucleation takes place due to activation of the pre-existing vapor nuclei, the kinetics of the liquid-vapor meniscus i.e. thermal and mechanical non-equilibrium plays a vital role in the delay of the ONB.

The delay in the incipience of boiling results in the increase of the internal energy of the test sample. Surface roughness increases the wetted surface area which enhances heat transfer during non-boiling phase. Hence, the internal energy in the moderately rough samples during the non-boiling regime is higher compared to the highly rough surface. This energy suddenly gets released after boiling incipience and thus surface experiences a sudden drop in the temperature, a moment of so-called temperature overshoot (T_{ov}), as shown in Figure 4.16. Temperature overshoot does not appear for smooth surface as latent heat transfer by the nucleated bubble on the smooth surface are not enough to overcome the exponential heat supply. This thermal non-equilibrium also exists during rapid exponential heat supply irrespective of the surface roughness.

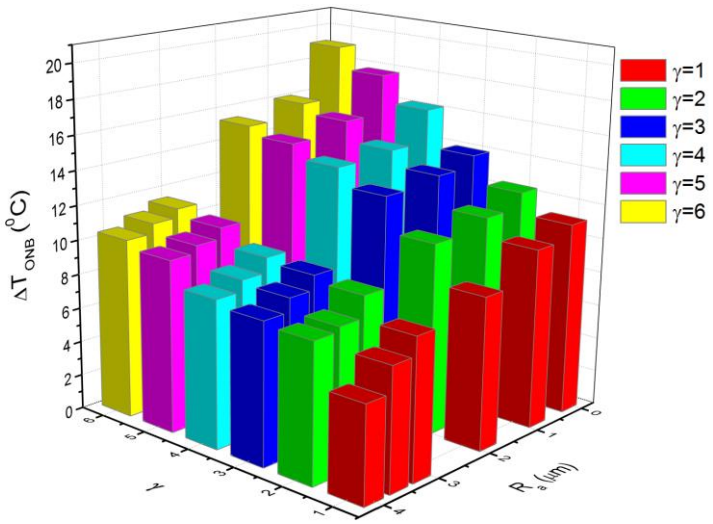

Figure 4.15 Variation in ΔT_{onb} with γ and R_a at P=1 bar

During quasi-steady exponential heat supply, two different incidents are identified immediately after boiling incipience as shown in Figure 4.16. ONB is observed in the beginning which is followed by the onset of boiling driven (OBD) phase. ONB and OBD are observed by the high speed camera. The sudden rise in the heat flux from the surface is noticed at OBD as number of bubbles considerably increase. At quasi-steady exponential heat supply, the stored energy in the sample drops due to OBD heat transfer which results in sharp fluctuation in the measured temperature immediately after OBD. This moment at which surface temperature drops is called as overshoot (OV) temperature. The ONB and OBD points coincide during the rapid transient as the explosive bubble growth is observed at the ONB. The absence of OV temperature indicates that the heat removed after ONB is not enough to reduce the rapidly increasing surface temperature.

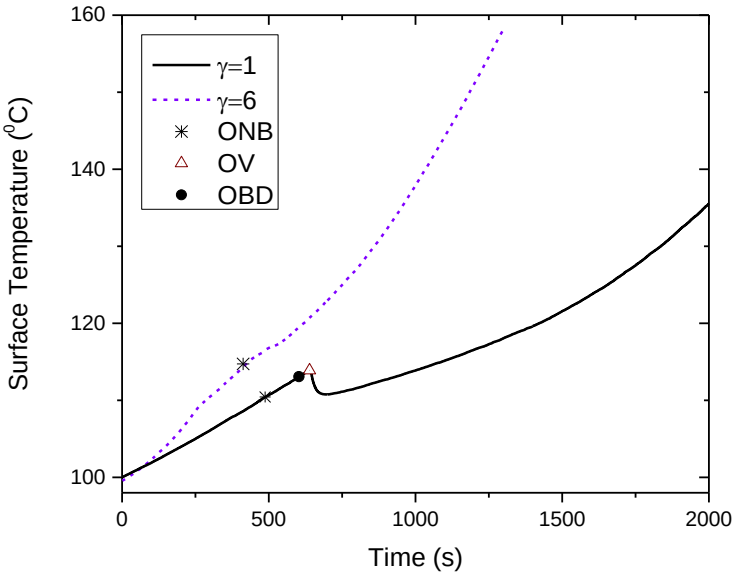

Figure 4.16 Time trace of the surface temperature of R_a=3.17 μm at P=1 bar

The variation in the incipience heat flux $q''_{ONB,ts}$ with γ is plotted for different R_a in Figure 4.17. It is observed that q_{ONB} for smooth and moderately smooth surface increases with increase in γ whereas it is almost constant for highly rough surfaces. Heat flux at ONB from surfaces of high roughness value is found to be approximately 15% of the heat flux at the transition of nucleate boiling to film boiling regime.

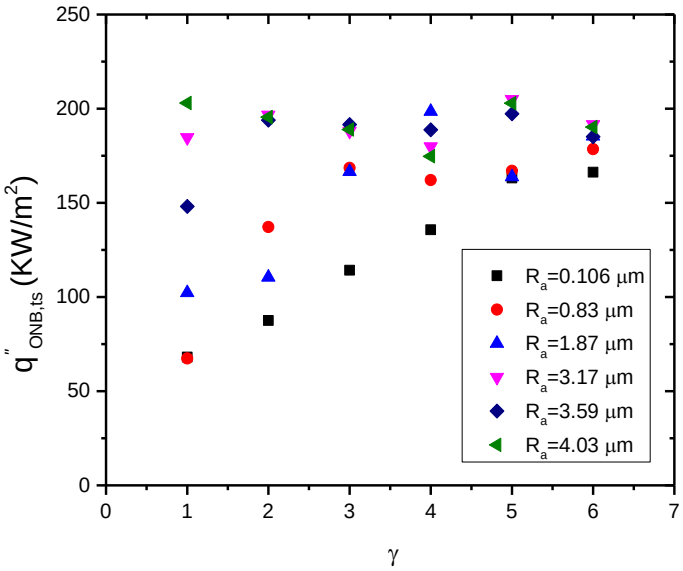

Figure 4.17 Variation in $q''_{ONB,ts}$ with γ

4.9 VARIATION IN TRANSIENT HTC WITH TRANSIENT HEAT FLUX

Non-dimensional h_{ts} and q_{ts} is derived from the reference values of h and q suggested by Kim et al. (2016), as given in Equation (4.2). The values h_0 and q_0'' are calculated from the thermo-physical properties of the saturated liquid at reference condition of 1 bar, 5 bar and 10 bar pressure. Variation in non-dimensional h_{ts} with non-dimensional q_{ts} at each pressure for different R_a is shown in Figure 4.18. The curves shift upward gradually with increase in the surface roughness at each pressure. The identical trend of the non-dimensional h_{ts} curves, as given in Figure B.6 (a-n) of Appendix B, is also observed for each time constant of exponential heat supply. It suggests the augmentation of HTC due to increase in the surface roughness and pressure.

$$h_0 = \frac{\mu_l c_{pl}}{Pr_l}\left[\frac{g(\rho_l-\rho_v)}{\sigma}\right]^{1/2} \quad ; \; q_0'' = \mu_l h_{fg}\left[\frac{g(\rho_l-\rho_v)}{\sigma}\right]^{1/2} \tag{4.2}$$

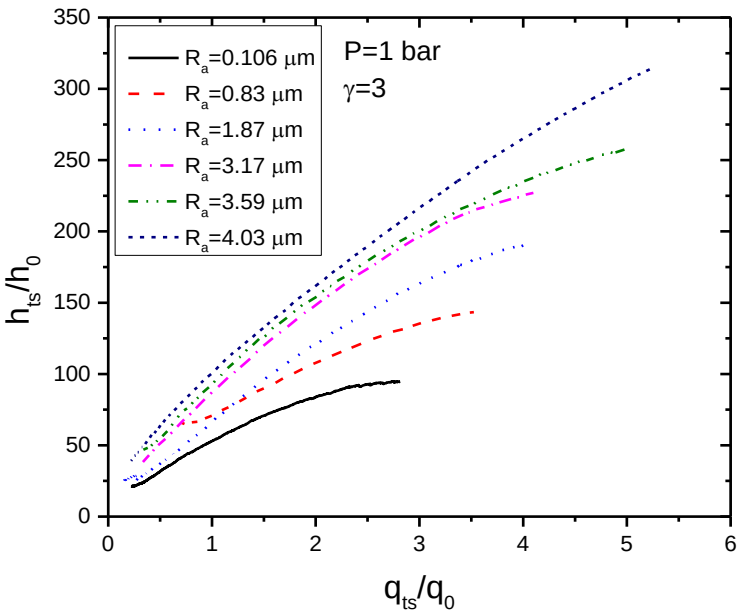

(a)

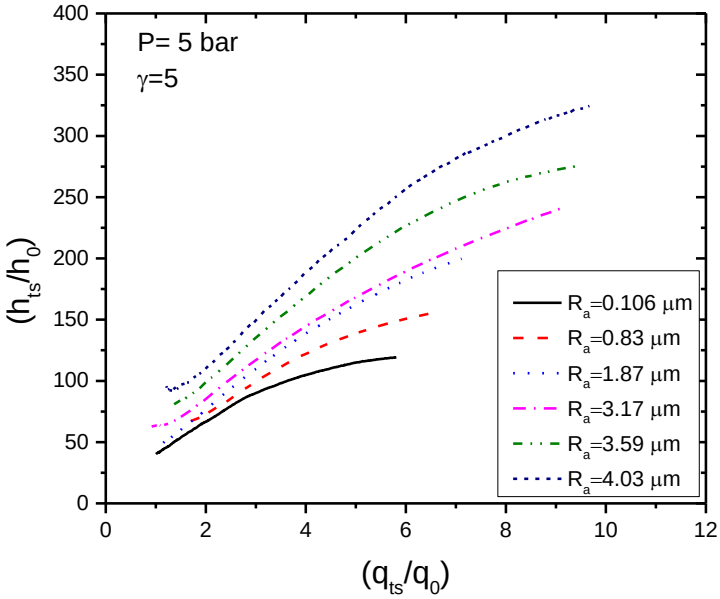

(b)

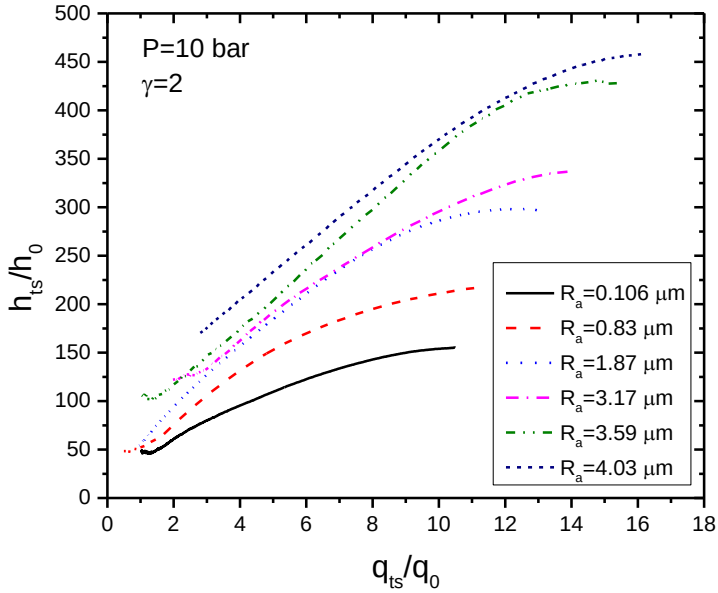

(c)

Figure 4.18 Variation in non-dimensional h_{ts} with non-dimensional q_{ts} for different surface roughness at (a) P=1 bar, γ=3 (b) P=5 bar, γ=5 (c) P=10 bar, γ=2

4.10 CRITICAL HEAT FLUX

The transition from FDNB to film boiling occurs due to formation of vapor blanket on the entire surface. The upper limit of the heat flux at this moment is defined as CHF. The peak of the curve shown in Figure 4.18 that corresponds to the maximum HTC is identified as CHF. After CHF, the HTC decreases with the increase in the wall superheat. The steady and transient state pool boiling study are carried to examine the effect of heating condition on CHF. The steady state CHF values for both, rough surface and microchannel geometry, are plotted in Figure 4.19 at pressure of 1 bar, 5 bar and 10 bar. The CHF of stepped microchannel is higher than that of parabolic and square one. It is found that steady-state CHF for SM-1.0, PM-1.6 and SM-1.6 is 66.87%, 100.60% and 131.36% higher than that for R_a=0.106 μm, respectively, at P=1 bar. The stepped and parabolic microchannel have wider channel top width compared to that of square microchannel. Larger channel mouth assists the growth of the bubble and improves the quantity of liquid supply through the channel. Hence, steady-state CHF for parabolic and stepped microchannel is higher than that for square microchannel. In case of parabolic microchannel, bubble always nucleates at the channel base and gets adhered to the channel wall due to parabolic channel profile. This restricts the upward bubble growth and thus, bubble spreads in the channel space. However, in case of stepped microchannel, bubble nucleates at the corner of step can grow and depart without any influence of the channel wall. Moreover, liquid replenishment in the stepped microchannel can takes place from bottom of the channel as well as from the channel top. This characteristics of stepped microchannel has resulted in the best heat transfer performance among the tested microchannel geometries. The effect of surface roughness on CHF at different pressures is also studied. It is found that CHF has enhanced remarkably due to increase in the surface roughness. The improved surface wettability and increased nucleation site density due to unidirectional scratches play vital role in the CHF enhancement. It is found at P=1 bar that steady-state CHF for R_a=4.03 μm is 92.85% higher than that for R_a=0.106 μm. The steady-state CHF of R_a=4.03 μm is close to the CHF of stepped microchannel at high pressure. It seems that the surface modification into stepped microchannel and rough surface (R_a=4.03 μm) have equal potential for CHF enhancement.

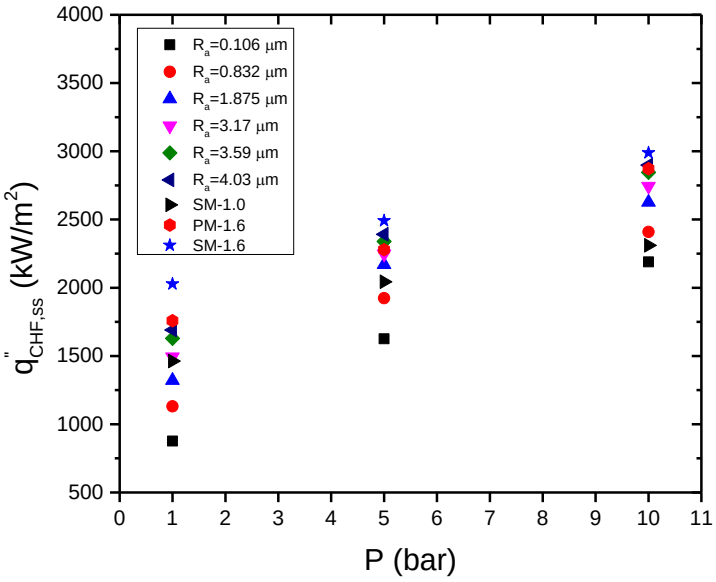

Figure 4.19 Steady-state CHF of rough and microchannel geometries as function of pressure

The study is also carried out by supplying exponential heat with different time constant to understand the effect of state of heating on CHF. The variation in CHF with γ at P=5 bar is shown in Figure 4.20. It is found that transient CHF for rough as well as microchannel geometries gradually decreased with increase in γ during exponential heat supply. Sakurai and Shiotsu (1977) and Su et al. (2016) reported that the transient CHF of thin element decreased with increase in the rate of heat supply. The drop in the CHF implies the inefficient heat removal from the surface during rapid exponential heating. The mechanism of liquid-vapor interaction plays vital role in the occurrence of CHF. The rapid unsteady state heat supply causes the instability in the liquid replenishment. Spontaneous nucleation is observed during rapid transient which leads to early horizontal bubble coalescence. Thus, bubble spreads rapidly over the horizontal surface causing large bubble to depart from the surface. This mechanism of boiling during rapid heating is the reason for drop in the CHF.

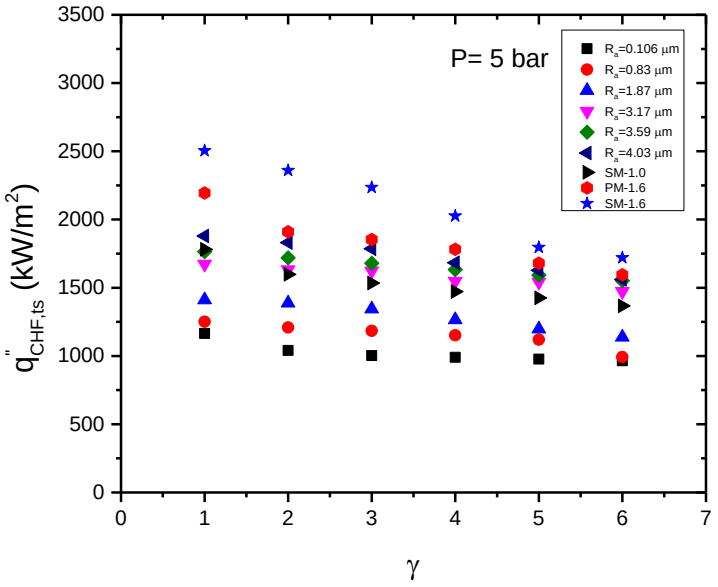

Figure 4.20 Effect of time constant on transient CHF of rough and microchannel geometries at 5 bar pressure

At P=5 bar, CHF for R_a=0.106 µm, R_a=0.83 µm, R_a=1.87 µm, R_a=3.17 µm, R_a=3.59 µm and R_a=4.03 µm during rapid transient of γ=6 is decreased by 13.43%, 4.79%, 9.6%, 12.76%, 8.29% and 16.79%, respectively, from the CHF obtained during quasi-steady transient of γ=1. CHF for microchannel geometries like SM-1.0, PM-1.6 and SM-1.6 during exponential heat supply of γ=6 at P=5 bar is decreased by 23.20%, 27.29% and 31.31%, respectively. It is clear that the drop in the CHF for microchannel geometries is much higher than drop in the CHF for highly rough surface. It suggests that the microchannel geometries are not capable enough as that of rough surface for the efficient heat removal at rapid heat supply. The liquid replenishment during rapid transient should be highly efficient and quick as spontaneous bubble growth may lead to rapid bubble spreading over the surface, resulting in the surface dry-out. During slow exponential transient, sufficient liquid supply to the nucleation sites can takes place through the microchannel. However, during rapid transient, dry-out of channel occurs quickly due to instability in the liquid-vapor motion. Moreover, channel wall restricts the upward bubble growth which also triggers the bubble spreading in the channel space. During rapid heat supply, hydrophilic surface of unidirectional scratches does

not allow the bubble to spread over the surface which keeps nucleation sites flooded even at high heat flux. The variation in the transient CHF with the time constant at pressure upto 10 bar is also studied and results are plotted in Figure B.7 (a-b) of Appendix B.

The comparative study shown in Figure 4.21 suggests that transient CHF is lower than that of the steady-state CHF for all the samples. The transient CHF for R_a=4.03 μm at heat supply of γ=1 and γ=6 is found to be 9.38% and 24.60%, respectively, lower than the corresponding steady-state CHF at P=1 bar.

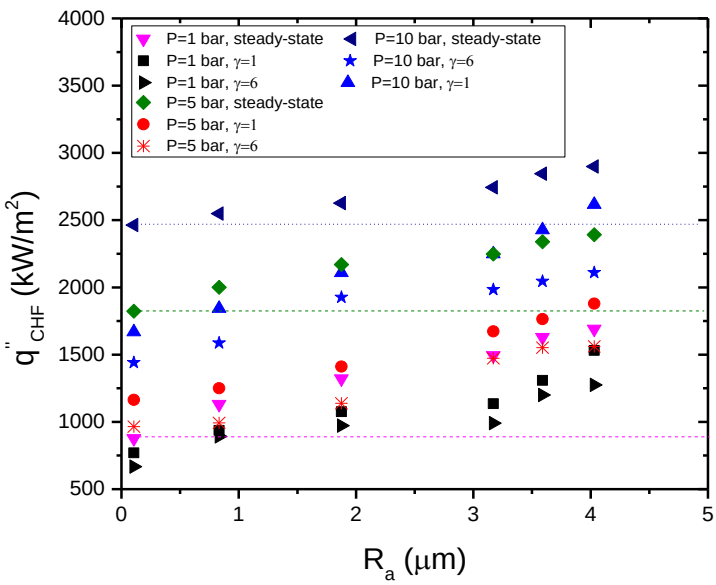

Figure 4.21 Effect of surface roughness on steady and transient CHF at various pressures

It is found that transient CHF of R_a=4.03 μm during exponential transient of γ=1 is higher than the steady-state CHF of R_a=0.106 μm at all pressures. It means that drop in the CHF during exponential heat supply can be compensated by using sample of rough surface. It is also found that drop in the CHF during short transient (γ=6) can be compensated only at P=1 bar and P=5 bar by increasing the surface roughness upto 4.03 μm. This can be justified through bubble dynamics and wettability study. Though it is vague to characterize surface solely based on R_a, it is the most suitable parameter related

to the unidirectional scratches, where R_a relates to the radius of the capillary tube. Additional parameter S_m is also quantified to explain the role of unidirectional scratches in CHF enhancement. It is observed during characterization that mean spacing S_m between two adjacent scratches increases with increase in R_a. Hydrophilicity of the rough surface and the quantity of liquid supply through the scratches increase with increase in R_a. The increase in S_m resulted in increase in the spacing between the nucleated bubbles. Thus horizontal bubble coalescence is retarded at high heat flux. Thus, the combined effect of R_a and S_m resulted in CHF enhancement which can compensate the drop in the CHF during transient heat supply. CHF values obtained for each sample during γ=3 at different pressure are plotted in Figure 4.22 to examine the effect of pressure on transient CHF. It is found that the transient CHF for R_a=0.106 μm increases by 40.21% and 128.66% due to increase in the pressure to P=5 bar and 10 bar, respectively.

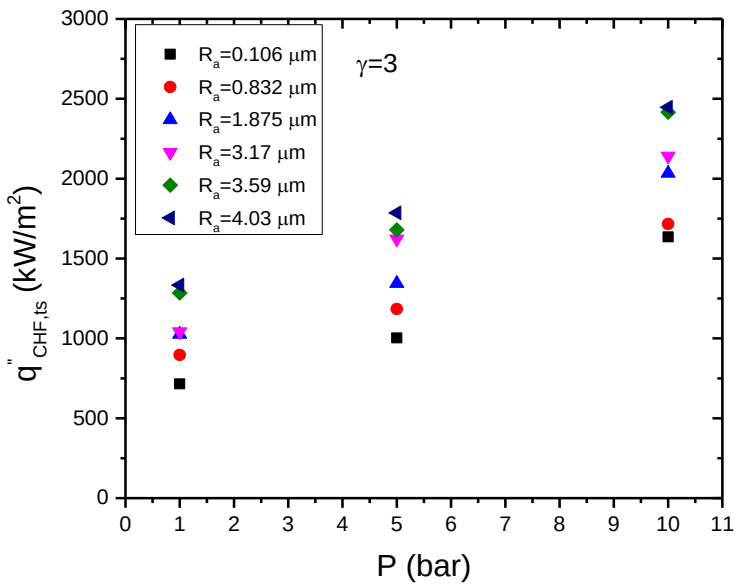

Figure 4.22 Variation in transient CHF with pressure at different surface roughness

The comprehensive influence of all the parameters on CHF is examined with the help of contour plot shown in Figure 4.23. The normalized values of these parameter are used to plot the contour. The range of the values is categorized into lower, moderate

and higher range. It is clear that lowest CHF is observed in the region of lower R_a and higher γ at low and moderate pressure. The highest CHF is found in two regions viz. higher range of γ along with higher R_a at lower range of pressure and lower range of γ with moderate R_a at higher pressure. It is concluded that surface roughness plays vital role in the CHF enhancement irrespective of operating pressure. However, rapid transient deteriorates the CHF of the pool boiling on smooth surface at low pressure.

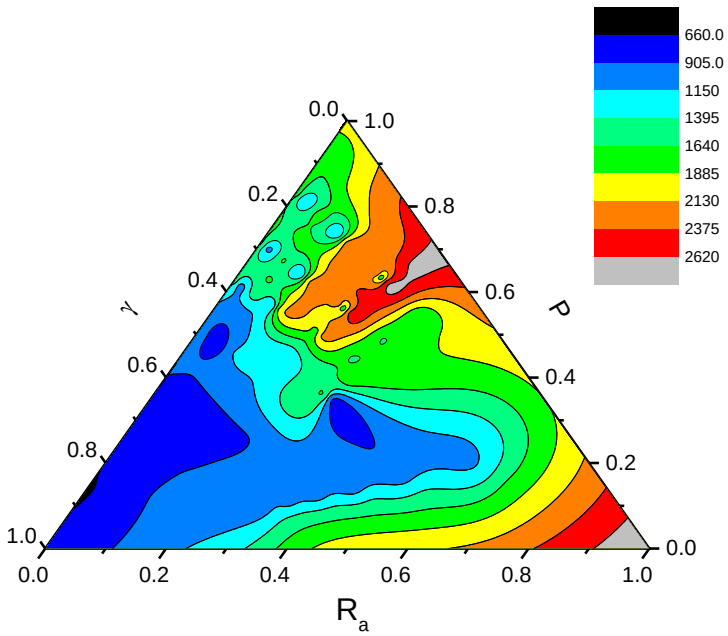

Figure 4.23 Contour plot of CHF for normalized R_a, γ and P

4.11 TRANSIENT MAXIMUM HEAT TRANSFER COEFFICIENT

Transient maximum heat transfer coefficient ($h_{max,ts}$) obtained for each sample at different pressure and heat supply of different time constant is presented in Figure 4.24. It is found that $h_{max,ts}$ considerably increased with increase in R_a signifying the efficient heat removal during each transient heat supply due to improved surface roughness values. The time constant during exponential heat supply has adverse effect on $h_{max,ts}$ however it is found to be moderate. The percentage increase in $h_{max,ts}$ increases with increase in the pressure at fixed R_a.

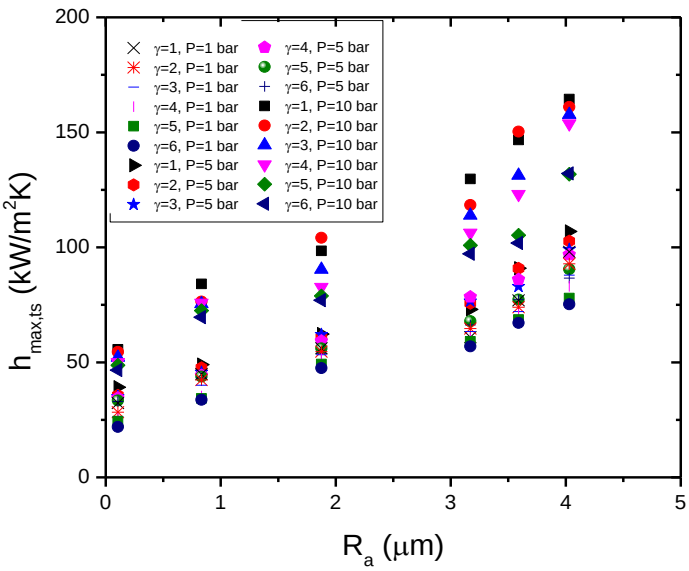

Figure 4.24 Effect of surface roughness on transient HTC at different time constant and pressure

The comprehensive influence of all the parameters viz. R_a, γ and P on h_{max} is examined with the help of contour plot shown in Figure 4.25. The normalized values of these parameter are used to plot the contour. The range of the values is categorized into lower, moderate and higher range. It is found during rapid transient that h_{max} is lowest for pool boiling on smooth surface at lower range of pressure. Maximum value of h_{max} is found for higher R_a at moderate pressure and slow transient.

In this work, it is found that transient CHF decreases with increase in the time constant and CHF of steady state condition is found to be higher than transient CHF for each sample. It is important to develop a relation between steady and transient CHF to predict the drop in CHF due to transient heat supply. A correlation for steady state CHF as a function of R_a and P is derived as given in Equation (4.3) by least square regression analysis. The predicted $q''_{CHF,ss}$ at different experimental $q''_{CHF,ss}$ are plotted in Figure 4.26 and it is found that present correlation predicts $q''_{CHF,ss}$ with MAE of 6.05%.

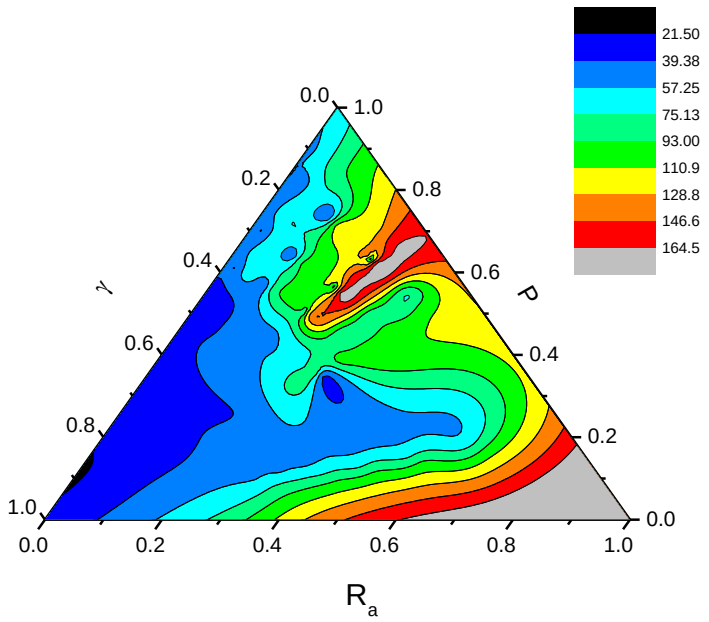

Figure 4.25 Contour plot of h_{max} for normalized R_a, γ and P

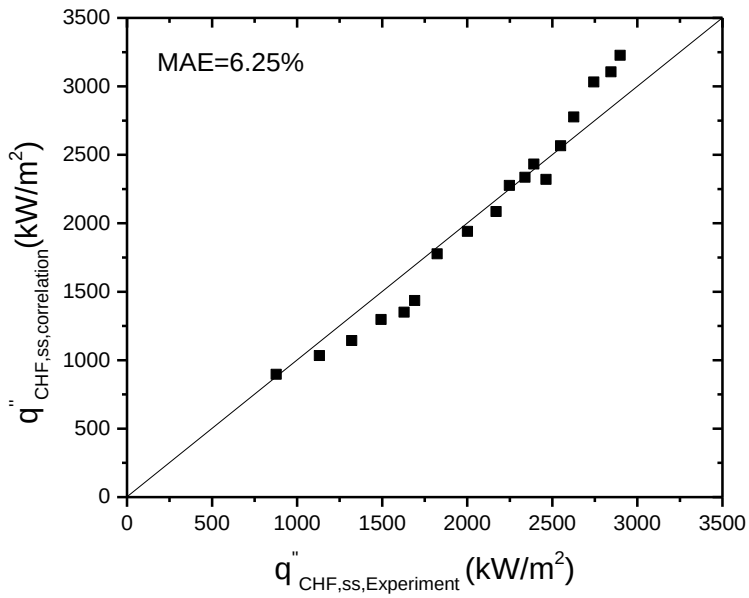

Figure 4.26 Comparison of CHF predicted by Equation (4.3) with the experimental CHF at steady-state heat supply

The correlation of $q''_{CHF,ts}$, as given in Equation (4.4), is also developed by similar method and the comparison between predicted $q''_{CHF,ts}$ and experimental $q''_{CHF,ts}$ is given in Figure 4.27. This correlation predicts $q''_{CHF,ts}$ with MAE of 10.11%.

$$q''_{CHF,ss} = 1280.8\,(R_a)^{0.14}(P)^{0.27} \tag{4.3}$$

$$q''_{CHF,ts} = 1031.9\ (\gamma)^{-0.08}(R_a)^{0.14}(P)^{0.27} \tag{4.4}$$

A relation between steady and transient CHF is derived using Equation (4.3**)** and Equation (4.4) and is expressed in Equation (4.5).

$$q''_{CHF,ts} = 0.81(\gamma)^{-0.08}q''_{CHF,ss} \tag{4.5}$$

Many investigators have suggested that HTC is a strong function of surface roughness and correlations in the form of $h\ \alpha\ C{R_a}^m q^n$ are proposed. The correlation presented by Gorenflo (1993) is found to be useful, as it predicts the HTC of almost all the fluids at high pressure. Gorenflo (1993) used the exponent of R_a, m=0.133 as suggested by Stephan (1963). A simplified form of Gorenflo correlation is given in Equation (4.6).

$$h = h' \times F_P \times F_q \times F_R \tag{4.6}$$

where, $F_P = 1.73{P_r}^{0.27} + \left(6.1 + \frac{0.68}{1-P_r}\right){P_r}^2$; $F_q = \left(\frac{q}{q'}\right)^n$; $n = 0.9 - 0.3{P_r}^{0.15}$;

$F_R = \left(\frac{R_a}{R_{a0}}\right)^{0.133}$

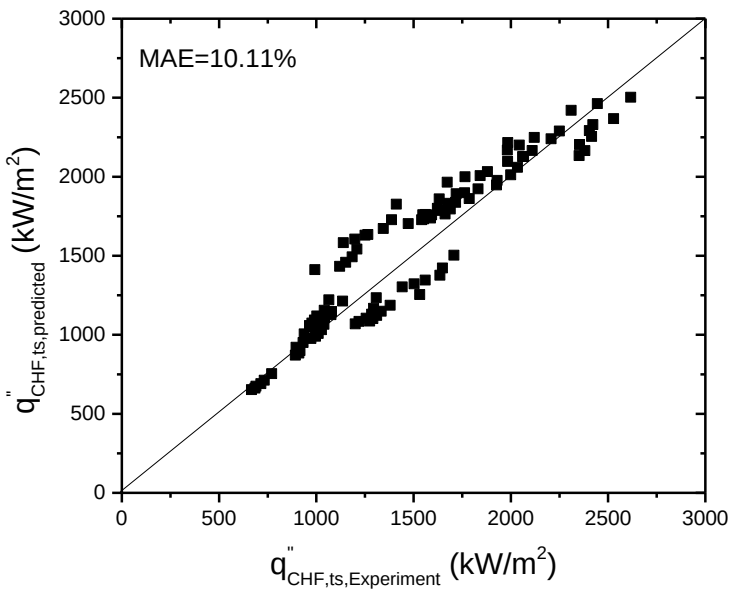

Figure 4.27 Comparison of CHF predicted by Equation (4.5) with the experimental CHF at exponential heat supply

The reference conditions for pure water are $h^{'}$=5600 W/m^{2}K, $q^{'}$=20,000 W/m^2 and R_{a0} = 0.4 μm. The values of predicted HTC by Equation (4.6) at corresponding experimental values are plotted in Figure 4.28 and it is found that error between the experimental transient HTC and predicted HTC increases with increase in the time constant γ. In the present study it is found that HTC is also the function of γ. As Equation (4.6) does not consider the effect of γ for the prediction of HTC, it is found that predicted HTC values are higher than the experimental values. The MAE between predicted and experimental HTC is 20.96%.

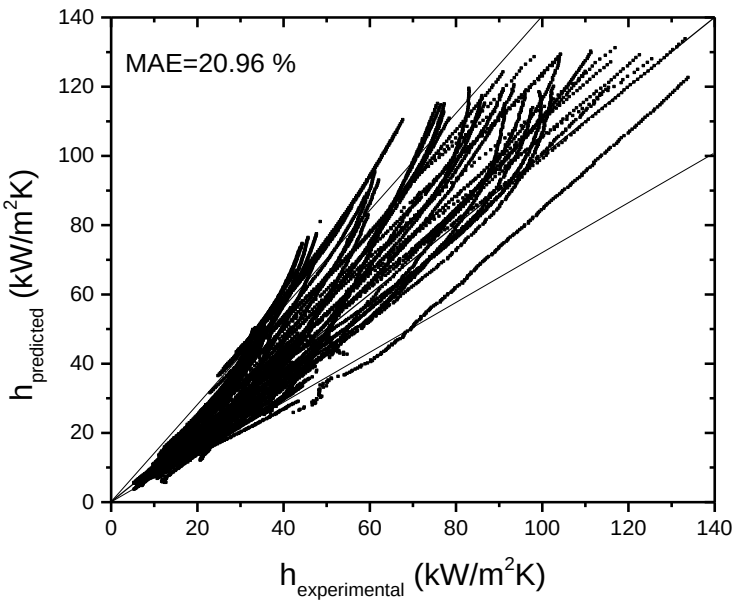

Figure 4.28 Comparison of HTC predicted by Equation (4.6) with the experimental HTC at exponential heat supply

The Gorenflo correlation is modified to account for the effect of transient heat supply wherein the time constant γ is incorporated. γ can be called as non-dimensional time value which justifies the rate of transient i.e. slow, intermediate or rapid transient. Thus, modified Gorenflo correlation is formulated as given in Equation (4.7).

$$h_{ts} = h' \times F_P \times F_q \times F_R \times F_\gamma \tag{4.7}$$

where, $F_\gamma = \gamma^s = \left(\frac{t}{\tau}\right)^s$

Following the Gorenflo's work, the exponent of the time constant (s) is obtained from the regression analysis and its value is -0.15. The predicted HTC values are plotted at corresponding experimental values as shown in Figure 4.29. MAE between the experimental and predicted HTC is 14.91%. The negative value of s indicates the inverse relation between HTC and γ. HTC considerably drops with increase in γ due to its adverse effect on bubble mechanism. This mechanism is discussed in the earlier section.

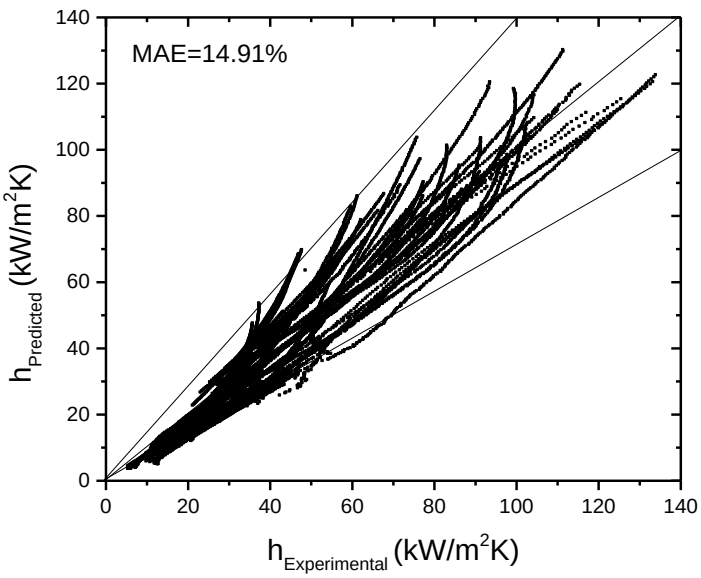

Figure 4.29 Comparison of transient HTC predicted by Equation (4.7) with the experimental HTC

CHAPTER 5

CHF MODEL

Critical heat flux is the maximum limit of efficient heat removal from the surface and hence it is vital to predict the CHF through the knowledge of governing mechanism. Several approaches for the prediction of CHF have been proposed earlier which can be broadly classified as far-field and near field model. The present experimental steady-state CHF values and CHF values predicted by model of Zuber (1959), Lienhard and Dhir (1973), Kandlikar (2001) and Kim et al. (2016) for R_a=0.106 μm are plotted in Figure 5.1. The CHF value predicted by Zuber (1959) and Lienhard and Dhir (1973) is higher than the experimental CHF value. The effect of contact angle is considered by Kandlikar (2001) whereas effect of both, surface roughness and contact angle are considered by Kim et al. (2016) in their model. The predicted CHF by model of Kandlikar (2001) and Kim et al. (2016) agree well with the present experimental CHF value at 1 bar. However, at higher pressure, experimental values are higher than the predicted values. Figure 5.2 shows the comparison of experimental and predicted CHF by Kim's model for the sample of R_a ranging from 0.106 μm to 4.03 μm at P=1 bar, P=5 bar and P=10 bar. It is found that the predicted values of CHF by Kim's model are higher than the experimental CHF for the sample of higher surface roughness ($R_a \geq 3.17$ μm). This variation between experimental and predicted CHF values is obvious because the Θ and C used for the CHF prediction at high pressure are measured at atmospheric pressure. Kim et al. (2016) conducted experiments at atmospheric pressure and developed a CHF model which predicts their experimental values in good agreement. To predict the CHF at high pressure, the parameter Θ and C need to be determined at corresponding saturation temperature and system pressure. It clearly suggests that CHF model should be developed by incorporating the effect of pressure and corresponding saturation temperature on the wettability.

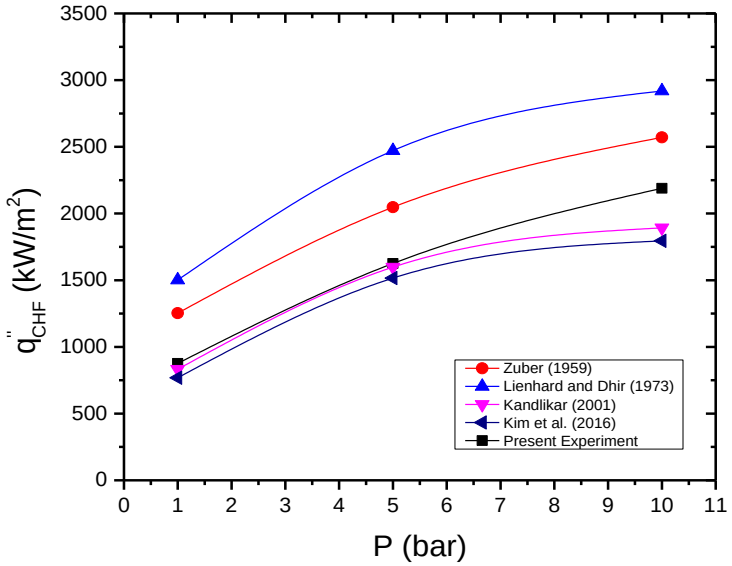

Figure 5.1 Variation in CHF with pressure

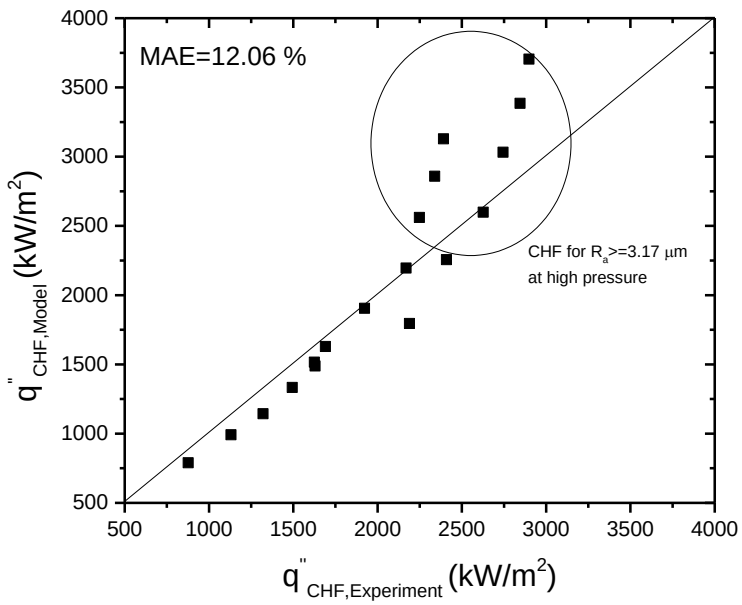

Figure 5.2 Comparison of CHF predicted by model of Kim et al. (2016) with present experimental CHF

5.1 PRESENT MODEL

It is proved by the study presented in the literature that CHF enhancement due to improved surface characteristics like micro-pillar structure, surface roughness, surface wettability and nucleation site density can be modelled by force balance approach. As R_a solely can not characterize the surface, additional parameter i.e. spacing between two adjacent scratches (S_m) is also considered in the present model. Static contact angle between water droplet and the surface before the pool boiling experiments is considered in the literature. The parameter, so called bubble angle (Θ_b), is the angle between the bubble meniscus, surface and the surrounding liquid seems to be the most relevant and real time entity to be considered instead of contact angle of the water droplet. Phan et al. (2009, 2010, 2011), Teodori et al. (2017) and Malavasi et al. (2018) suggested a relation between static angle and bubble angle. The trend of bubble departure diameter and contact angle was also presented. They developed a model where the concept of macro- and micro-contact angles is coined. In the present study, the bubble angle for four discrete bubbles at each pressure and roughness value is measured. Schematic diagram of bubble angle measurement is shown in Figure 5.3.

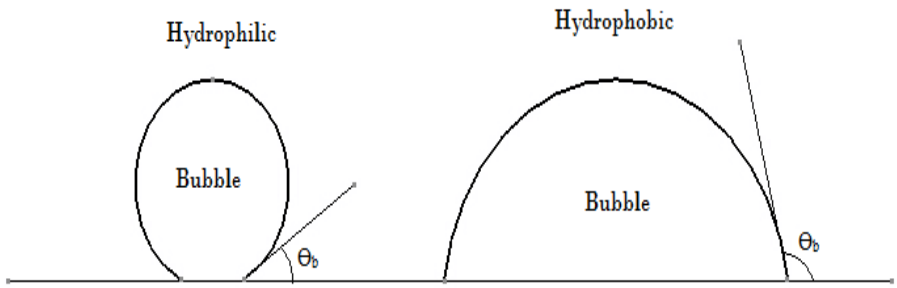

Figure 5.3 Schematic representation of bubble angle measurement

The average value of bubble angle at different pressures is given in Figure 5.4. It is found that contact angle of the water droplet measured at 25°C is approximately 9°

higher than the bubble angle measured at the saturated condition. This bubble angle study suggests that surface becomes hydrophilic with increase in R_a. However influence of R_a on bubble contact angle diminishes at high pressure.

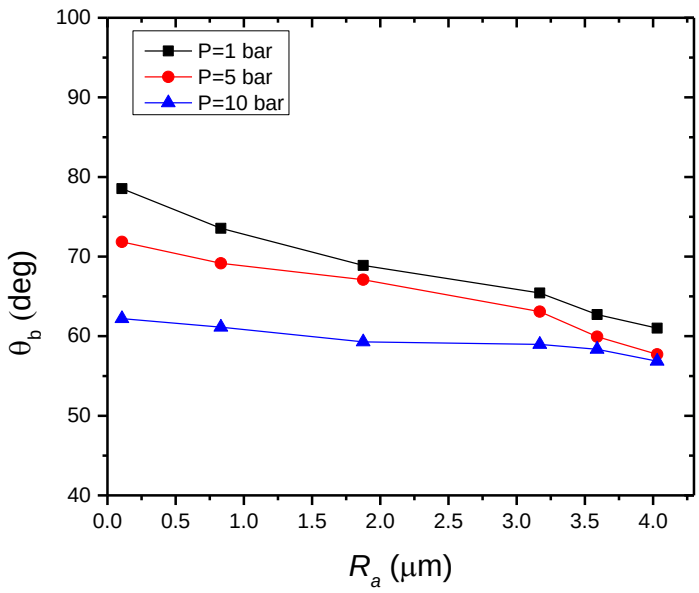

Figure 5.4 Variation in bubble angle with R_a at different pressure

Present study thus includes the effect of surface roughness on bubble angle at different pressures which is not yet considered in the CHF model presented in the literature. Present experimental study of transient pool boiling is carried out at high pressure of distilled water using samples of different surface roughness value. The time constant (γ) should be included in the CHF model to predict transient CHF. The forces acting on the bubble parallel to the surface, as shown in Figure 5.5, are considered in the present force balance approach. Bubble experiences a pull force F_M during unsteady growth due to momentum change which allows bubble to spread over the surface. Simultaneously, sum of drag forces like surface tension force, gravity and capillary force also acts on the bubble which retains its original position and does not allow its horizontal growth. Visualization study suggests that fully developed nucleate boiling regime turns into film boiling due to progressive horizontal bubble coalescence. This

phase transition occurs when F_M surpasses the sum of drag forces resulting in CHF which is upper limit of efficient heat removal from the surface.

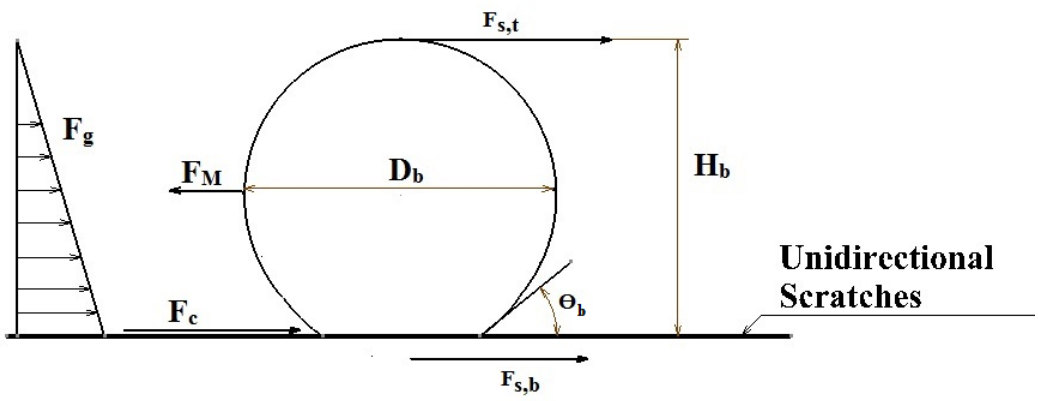

Figure 5.5 Forces acting on the bubble parallel to the surface

CHF is identified by the force balance as given in Equation (5.1).

$$F_M = F_{s,t} + F_{s,b} + F_g + F_c \tag{5.1}$$

A growing bubble experiences a force on its meniscus due to the change in momentum caused by the increase in velocity. F_M is the momentum change due to evaporation of the liquid and can be expressed as given in Equation (5.2).

$$F_M = \frac{1}{\rho_v}\left(\frac{q_l''}{h_{fg}}\right)^2 H_b \tag{5.2}$$

$F_{s,t}$ and $F_{s,b}$, given in Equation (5.3), are the surface tension forces acting at top and bottom of the bubble, respectively.

$$F_{s,t} = \sigma \; ; F_{s,b} = \sigma \cos\theta_b \tag{5.3}$$

F_g refers to the gravity force which is formulated in Equation (5.4) for the horizontal upward facing surface.

$$F_g = \frac{1}{2}\, g(\rho_l - \rho_v)H_b^2 \tag{5.4}$$

H_b is the equivalent height of the bubble and it is obtained by Equation (5.5). Bubble diameter can be formulated, as given in Equation (5.6), from Taylor unstable wavelength, as suggested by Kandlikar (2001).

$$H_b = \frac{D_b}{2}(1 + \cos\theta_b) \tag{5.5}$$

$$D_b = \frac{\lambda_T}{2} = \pi \left[\frac{\sigma}{g(\rho_l - \rho_v)}\right]^{1/2} \tag{5.6}$$

The capillary pressure P_c which acts on the bubble through the small tube of radius R_c is derived by Young-Laplace equation, as given in Equation (5.7).

$$P_c = \frac{2\sigma\cos\theta_b}{R_c} \tag{5.7}$$

Each unidirectional scratch on the surface is assumed as a single capillary tube and many such tubes lie underneath the bubble. Considering this assumption, it can be expressed, as given in Equation (5.8), that the radius of the capillary tube is proportional to the roughness value R_a.

$$R_a \propto R_c \tag{5.8}$$

Capillary force expressed by Equation (5.9) considers the number of capillary tubes underneath the bubble, radius of each tube and the capillary pressure inside each tube.

$$F_c = N\pi R_c^2 P_c = N\pi R_c^2 \frac{2\sigma\cos\theta_b}{R_c} = 2\pi N R_c \sigma\cos\theta_b \tag{5.9}$$

Kim et al. (2016) expressed the capillary force, as given in Equation (5.10), by considering inverse proportion between N and S_m.

$$F_c = 2\pi C\left(\frac{R_a}{S_m}\right)\sigma\cos\theta_b \tag{5.10}$$

Combining all the above forces, force balance is expressed by Equation (5.11).

$$\frac{1}{\rho_v}\left(\frac{q_l''}{h_{fg}}\right)^2 H_b = \sigma + \sigma\cos\theta_b + \frac{1}{2}\, g(\rho_l - \rho_v)H_b^2 + 2\pi C\left(\frac{R_a}{S_m}\right)\sigma\cos\theta_b \tag{5.11}$$

Equation (5.12) is obtained by rearranging the above equation to express q_l''.

$$q_l'' = h_{fg}{\rho_v}^{0.5}\,[\sigma g(\rho_l - \rho_v)]^{0.25}\left[\frac{2}{\pi} + \frac{\pi}{4}(1+\cos\theta_b) + \frac{4C\cos\theta_b}{1+\cos\theta_b}\left(\frac{R_a}{S_m}\right)\right]^{0.5} \tag{5.12}$$

Steady-state CHF can be obtained by the Equation (5.13) as suggested by Kandlikar (2001).

$$q_{CHF,ss}'' = \left(\frac{1+cos\,\theta_b}{16}\right) q_l'' \tag{5.13}$$

Thus the final form of steady-state CHF model is given in Equation (5.14).

$$q_{CHF,ss}'' = \left(\frac{1+cos\,\theta_b}{16}\right)\left\{h_{fg}{\rho_v}^{0.5}\,[\sigma g(\rho_l - \rho_v)]^{0.25}\right\}\left[\frac{2}{\pi} + \frac{\pi}{4}(1+\cos\theta_b) + \frac{4C\cos\theta_b}{1+\cos\theta_b}\left(\frac{R_a}{S_m}\right)\right]^{0.5} \tag{5.14}$$

The proportionality constant *C* implies the number of tubes underneath the growing bubble. CHF predicted by Equation (5.14) is compared with present experimental data and presented in Figure 5.6. The predicted CHF is found to be in good agreement with the experimental CHF with MAE of 6.65 %.

The transient CHF model of the samples with wide range of surface roughness R_a under exponential heat supply ranging from γ=1 to γ=6 at pressure upto 10 bar is obtained by combining Equation (4.5), Equation (5.12) and Equation (5.13) and is given in Equation (5.15).

$$q_{CHF,ts}'' = \left(\frac{0.81}{\gamma^{0.08}}\right)\left(\frac{1+cos\,\theta_b}{16}\right)\left\{h_{fg}{\rho_v}^{0.5}\,[\sigma g(\rho_l - \rho_v)]^{0.25}\right\}\left[\frac{2}{\pi} + \frac{\pi}{4}(1+\cos\theta_b) + \frac{4C\cos\theta_b}{1+\cos\theta_b}\left(\frac{R_a}{S_m}\right)\right]^{0.5} \tag{5.15}$$

As the bubble base diameter decreases with increase in pressure, the value of C decreases with increase in the pressure. The value of C is obtained by using θ_b, R_a, S_m, and CHF. The transient CHF predicted by Equation (5.15) is compared with present experimental data and presented in Figure 5.7. The predicted transient CHF is found to be in good agreement with the experimental transient CHF with MAE of 11.89 %. Thus new terms viz. time constant (γ) and bubble angle (θ_b) are included in the transient CHF model in addition to the roughness parameter R_a and S_m.

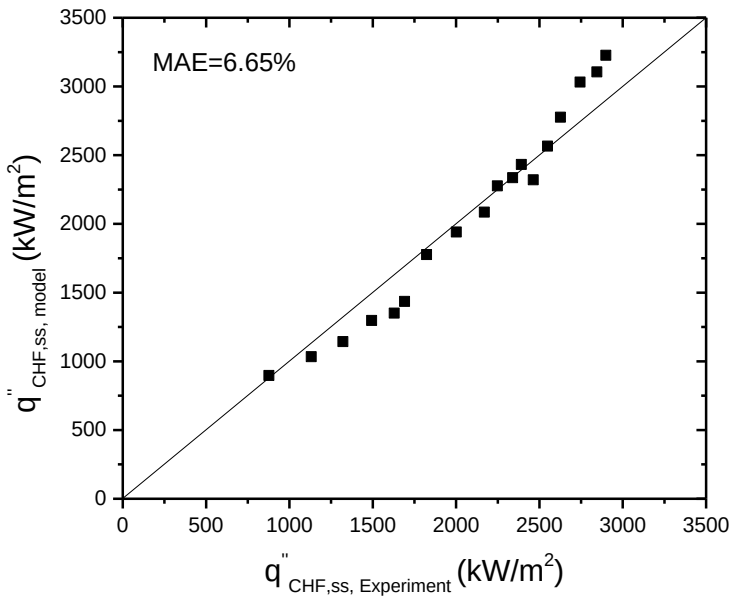

Figure 5.6 Comparison of CHF predicted by modified Kim's model with present experimental CHF at steady-state condition

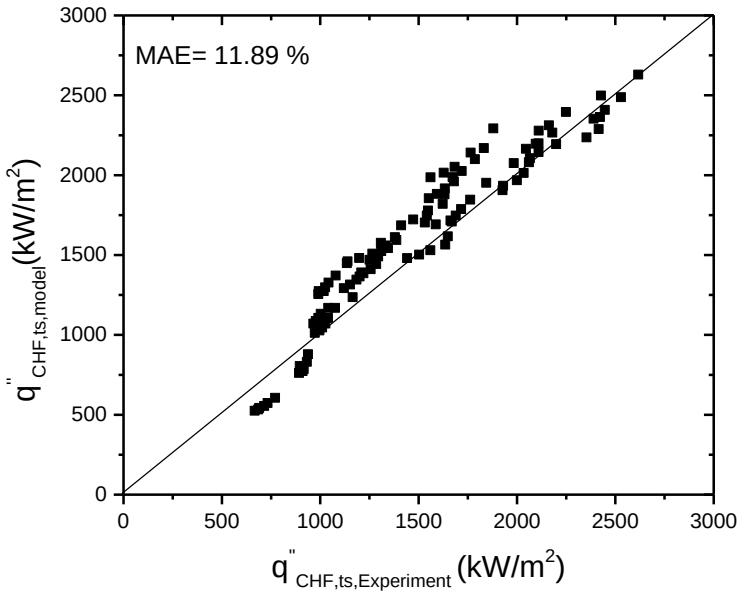

Figure 5.7 Comparison of experimental and predicted CHF

CHAPTER 6

BUBBLE DYNAMICS

The mechanism of bubble growth on microchannel geometry and rough surface during steady-state condition is studied. Bubble departure diameter and bubble frequency is measured at different pressure and presented in this chapter.

6.1 VISUALIZATION OF POOL BOILING ON MICROCHANNEL GEOMETRIES

6.1.1 Mechanism of bubble growth

The bubble growth study for all the microchannel geometries is done by the visualization of bubble nucleation, intermediate bubble growth and bubble departure at low heat flux range. The time trace of the bubble diameter is presented in Table. 6.1 at q=160-175 kW/m^2. For all the microchannel geometries, it is found that bubble originates at the corner of the channel, enlarges in the channel space and finally grows vertically. It is also noticed that bubble nucleation takes place at the fin top of square microchannel and departs independently only at low heat flux. At high heat flux, horizontal coalescence is observed between the bubbles generated from the adjacent channels as they grow beyond the channel height.

As shown in Figure 6.1, square channel is modified into parabolic and stepped profile by keeping the channel base width and channel height constant, which can have larger channel top width than square profile. Thus, the effect of channel top width on the bubble growth and departure diameter is discussed further. Larger channel mouth assist the growth of the bubble which has been generated from the small cavities present at the channel base. In case of square microchannel (β=1), bubble is confined between the two walls and can not grow beyond the channel width. During this phase, bubble may grow laterally along the length of channel and turns into elliptical shape. Finally, making a finite angle with top of the fin, bubble takes mushroom shape as it grows

beyond the channel height and departs spherically, as shown in Figure 6.2 (a). The liquid supply to the nucleation site for different channel profiles is schematically shown in Figure 6.2 (b).

Table 6.1 Bubble growth study at q=160-175 kW/m^2

Test surface	Bubble ebullition	Intermediate bubble growth		Bubble departure
Plain	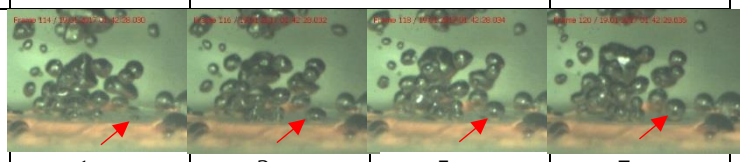			
	t=1 ms d=0.2 mm	t=3 ms d=0.39 mm	t=5 ms d=0.82 mm	t=7 ms D_b=1.5 mm
SM-1.0				
	t=1 ms d=0.42 mm	t=2 ms d=1.03 mm	t=4 ms d=1.80 mm	t=6 ms D_b=1.85 mm
PM-1.6	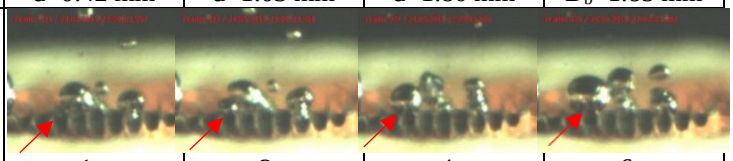			
	t=1 ms d=0.74 mm	t=2 ms d=1.32 mm	t=4 ms d=1.75 mm	t=6 ms D_b=1.97 mm
SM-1.6	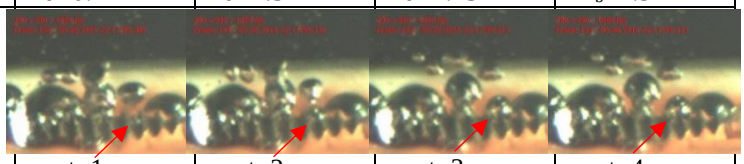			
	t=1 ms d=0.57 mm	t=2 ms d=0.98 mm	t=3 ms d=2.1 mm	t=4 ms D_b=2.01 mm

Since, parabolic and stepped microchannel have higher channel top width, trend of the bubble growth is found to be different. In both cases, bubble grows spherically in the channel zone before departure. However, bubble turns to mushroom shape as parabolic wall profile offers the restriction to the vertical bubble growth. This indicates the existence of cohesive role of the channel profile and channel top width of the geometry for the enhancement in departure diameter and bubble frequency.

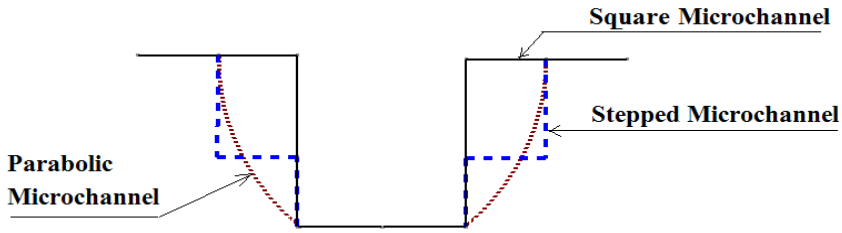

Figure 6.1 Schematic diagram of different channel profile

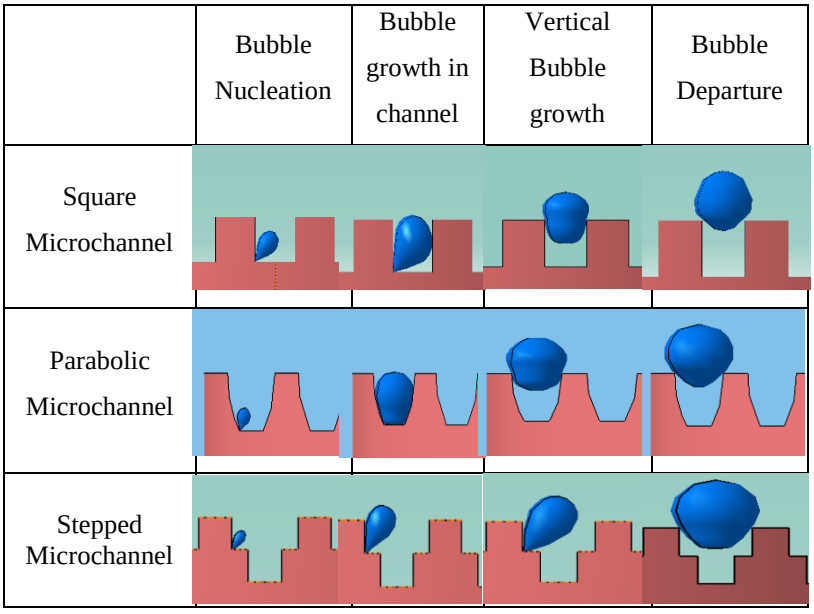

(a)

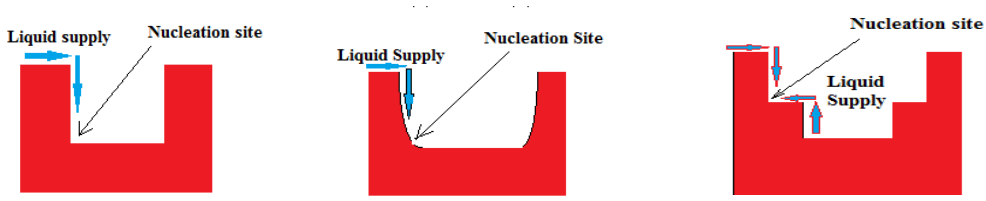

(i) Square channel (ii) Parabolic channel (iii) Stepped channel

(b)

Figure 6.2 Proposed mechanism of (a) bubble growth and (b) liquid supply in the microchannel

6.1.2 Effect of microchannel profile on bubble departure diameter

A pioneering study is done by the authors to examine the role of channel profile on bubble diameter, frequency and growth rate. The bubble departure diameter of the microchannel for different *Ja* at P=1 bar is plotted in Figure 6.3. The bubble departure diameter is found to be strong function of *Ja* as well as channel profile. Bubble departure diameter of all microchannel geometries is higher than that of plain surface. It is observed that stepped microchannel has higher bubble departure diameter than the parabolic channel profile. The potential of microlayer evaporation is considered to study the influence of channel profile. The wetted surface area of the stepped profile is higher than the parabolic profile which ensures the higher potential of microlayer evaporation. The superheated liquid supply to the nucleation site at the step of the channel is possible from either side of the channel wall, as shown in Figure 6.2. This increases the quantity of the liquid evaporation and thus bubble departed from the stepped microchannel is largest amongst all tested geometries.

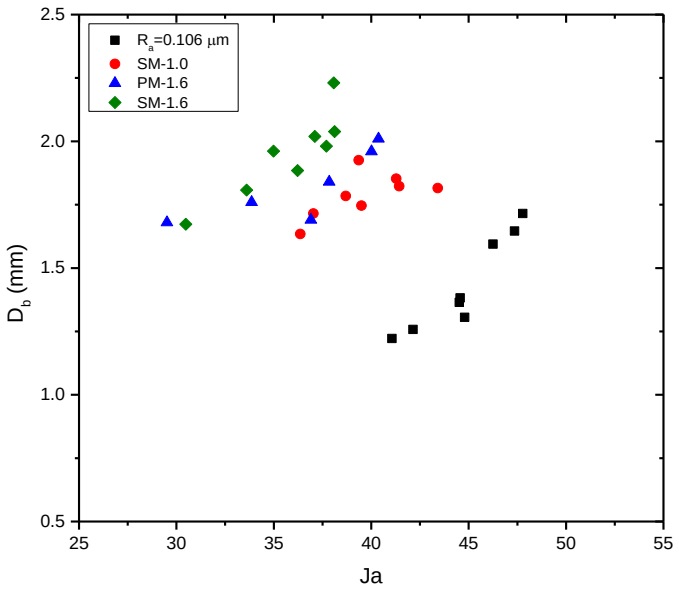

Figure 6.3 Variation of bubble departure diameter with Jakob number

6.1.3 Effect of microchannel profile on bubble frequency

The bubble frequency of the microchannel geometries for different *Ja* is shown in Figure 6.4 at P=1 bar. The forces acting on the bubble during its growth in the channel are considered to analyze the effect of channel profile on the bubble frequency. Bubble frequency for SM-1.0 is found to be lowest at low Jakob number as the bubble growth period is much higher than other microchannel geometries. Bubble frequency for SM-1.0 increases rapidly with increase in *Ja*. Bubble frequency for the stepped microchannel (SM-1.6) is higher than the parabolic microchannel (PM-1.6). For wider parabolic microchannel, it is observed that bubble acquires the exact shape of the wall profile and adheres to the solid wall. The surface tension force seems to be higher in this case. Thus, it reduces the bubble growth rate and frequency of the bubble formation. The bubble morphology of the stepped microchannel (SM-1.6) is different than parabolic (PM-1.6). Bubble generated at the step of the channel can grow without much influence of the channel wall. Bubble nucleated at the base of the channel exerts a push force to the growing bubble at the next step of the same channel which results in higher bubble frequency.

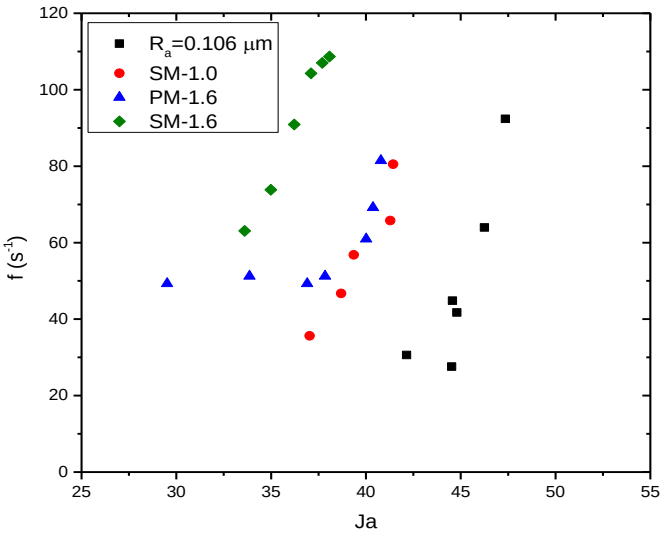

Figure 6.4 Variation of bubble frequency with Jakob number

6.2 MODELING OF BUBBLE DEPARTURE DIAMETER

6.2.1 Force Balance

In the microchannel geometries, the bubble nucleates and grows because of the evaporation of liquid microlayer present on the channel surface and this growth must be driven by inertia, as discussed by Ramaswamy et al. (2003). As mentioned earlier, the bubble departing from the channel wall is considered to be spherical and it makes a finite contact angle with the top surface of the channel wall. Hence, surface tension force should be considered to estimate the bubble diameter. The model developed in the present work for prediction of bubble departure diameter from the microchannel geometries considers the unsteady growth force, buoyancy force, surface tension, lift force and bubble inertia. The expression for the different forces are given below

(i) Unsteady growth force (F_{duy}): The bubble growth is a dynamic process for which momentum transfer between the growing bubble and surrounding stagnant liquid should be considered. The unsteady growth force acting on the growing bubble can be solved by estimating the pressure distribution along the liquid-vapor interface. The expression for growth force, given in Equation (6.1), considering transient bubble growth was developed by Zeng et al. (1993).

$$F_{duy} = \pi\rho_l r^2 \left(\frac{3}{2}C_s\dot{r}^2 + r\ddot{r}\right) \tag{6.1}$$

where C_s is an empirical constant and is equal to 20/3 as suggested by Klausner et al. (1993) and r is an instantaneous radius of the bubble.

For inertia driven mechanism, bubble growth rate follows Equation (6.2).

$$r(t) = at \tag{6.2}$$

where a is a function of wall temperature and fluid property. Thus, expression for unsteady growth force is formulated as Equation (6.3).

$$F_{duy} = \frac{3}{2}\rho_l \pi a^2 C_s r^2 \tag{6.3}$$

(ii) Buoyancy force (F_{buy}): The upward force experienced by the growing bubble due to density variation between liquid and vapor is defined as buoyancy force and is obtained by Equation (6.4).

$$F_{buy} = (\rho_l - \rho_v) g V_b \tag{6.4}$$

where V_b is the volume of spherical bubble and is obtained by Equation (6.5).

$$V_b = \frac{\pi}{6} {D_b}^3 \tag{6.5}$$

(iii) Surface tension force (F_{st}): Surface tension force acting on the bubble is formulated by considering the trend of the bubble growth. During phase-I growth, as shown in Figure 6.5, bubble grows on the base of channel where it expands vertically upward. After certain time, bubble grows against the confined channel wall. During Phase-II bubble growth, bubble turns into spherical shape where bubble meniscus makes a contact with the channel top. Surface tension forces involved in Phase-I $(F_{st})_I$ and Phase-II growth $(F_{st})_{II}$ period are considered as a function of channel parameter, surface tension and bubble departure diameter and thus it is formulated as given in Equation (6.6).

$$F_{st} = (\mathrm{F_{st,y}})_\mathrm{I} + (\mathrm{F_{st,y}})_\mathrm{II} = \frac{\pi}{3} \sigma \left[\frac{2{W_b}^2}{9C_h} + \frac{{W_t}^2}{D_b} \right] \tag{6.6}$$

Where $(F_{st,y})_I$ and $(F_{st,y})_{II}$ are the y-component of the surface tension forces acting during the Phase-I and Phase-II growth, respectively.

(iv) Lift force (F_L): The non-uniform velocity field is present across the bubble due to channel confinement, the liquid supply through channel and wake of the departing bubble. Hence, bubble experiences the upward lift force which is estimated by Equation (6.7) as given by Ramaswamy et al. (2003).

$$F_L = 2\pi \rho_l C_l (a D_b)^2 \tag{6.7}$$

where C_l = 1.2.

(v) Bubble inertia force (F_{bi}): The bubble inertia force resists the dynamic bubble growth which is obtained by Equation (6.8), as suggested by Sharma (1998).

$$F_{bi} = d(m_b v_b) = m_b \frac{dv_b}{dt} + v_b \frac{dm}{dr} \frac{dr}{dt} \tag{6.8}$$

where $v_b = \frac{dr}{dt} = a$, $\frac{dv_b}{dt} = \frac{d\ddot{r}}{dt} = 0$, $\frac{dm}{dr} = \pi \rho_b {D_b}^2$

Combining above terms, the expression of the resultant bubble inertia force is given in Equation (6.9).

$$F_{bi} = a^2 \pi \rho_b {D_b}^2 \tag{6.9}$$

As suggested by Ramaswamy et al. (2003), the liquid inertia force is considered as zero as velocity of bubble is constant.

The force balance equation can be written as Equation (6.10).

$$F_{duy} + F_{st} + F_{bi} = F_{buy} + F_L \tag{6.10}$$

The schematic description of the forces acting on the growing bubble is shown in the Figure 6.5.

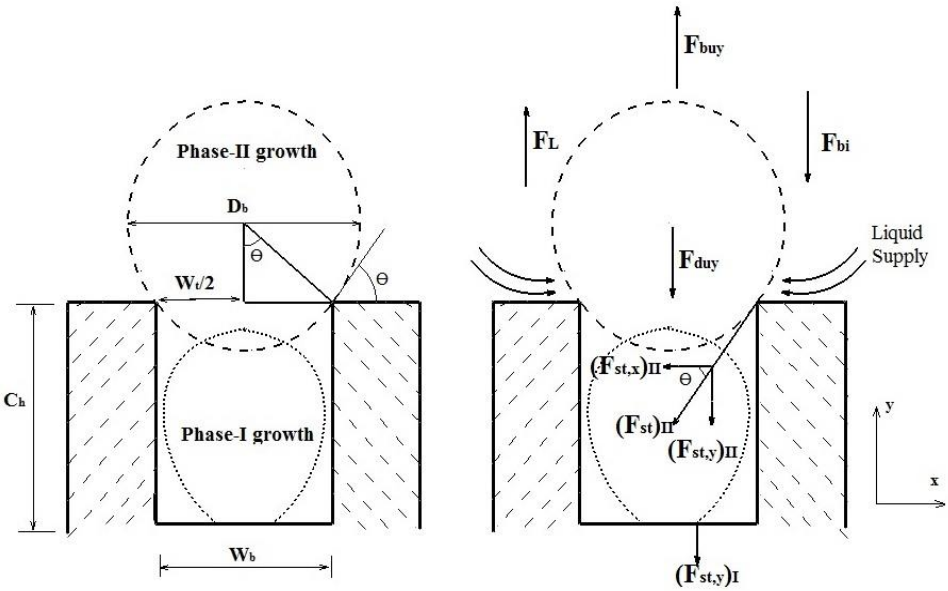

Figure 6.5 Bubble growth in Square Microchannel

It is observed that surface tension force is dominant during the initial growth of the bubble whereas it is found to be negligible during the Phase-II growth because of gradual reduction in the line of contact between the bubble and channel wall. As bubble grows in the channel space, considerable velocity and pressure variation exists across the bubble meniscus. During the Phase-II growth, buoyancy force become dominant as bubble diameter increases. The spherical bubble departs from the channel as upward forces (buoyancy and lift force) dominate the downward acting forces (growth force, surface tension and inertia force).

6.2.2 Verification of the model

Cooke and Kandlikar (2012) carried out pool boiling experiments on rectangular microchannel at atmospheric condition of water. Bubble departure diameter for Chip-2 (W_b=W_t=197 μm and C_h=335 μm) and Chip-9 (W_b=W_t=375 μm and C_h=400 μm) was found to be 0.82 mm and 1.55 mm, respectively. However, the corresponding wall superheat or heat flux is not available in the literature. Hence, bubble departure diameter is considered to be constant throughout their experiments. The bubble departure diameter of Chip-2 and Chip-9 is predicted by present model and results are presented in Figure 6.6.

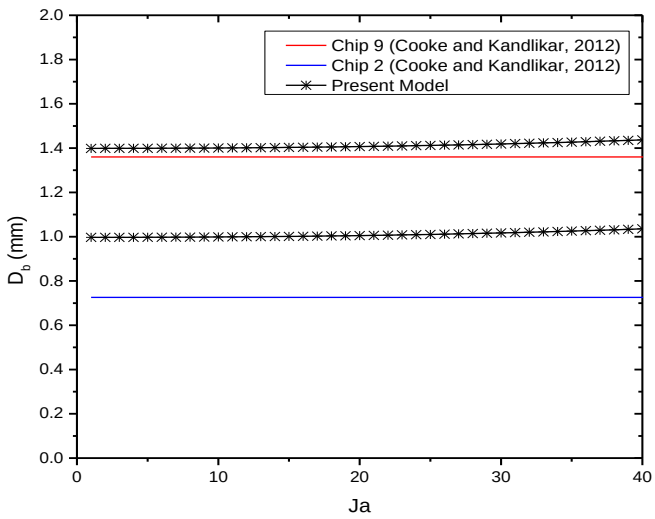

Figure 6.6 Comparison of bubble departure diameter of Chip 2 and 9 (Cooke and Kandlikar, 2012) with the present model

It is found that the predicted bubble departure diameter is in good agreement with the experimental results of Cooke and Kandlikar (2012) with MAE of 3.33 % and 38.21 % for Chip-9 and Chip-2, respectively. The deviation between predicted and experimental bubble departure diameter for Chip-2 is in the range of 0.27-0.30 mm. The bubble growth along the channel length may be much higher in the narrow channel of Chip-2 (W_b= 197 μm). The surface tension forces during lateral elongation of the meniscus is

not considered in the present model. This may be the reason for the over prediction of the bubble diameter in case of Chip-2.

The present model can predict the bubble departure diameter at high pressure as this model is based on thermo-physical properties of the fluid. The bubble departure diameter predicted by the present model and measured during experimentation at P=1 bar, P=5 bar and P=10 bar is compared and plotted in Figure 6.7 for all the microchannel geometries. MAE between predicted and experimental bubble departure diameter values for all the microchannel geometries is found to be 13.30%.

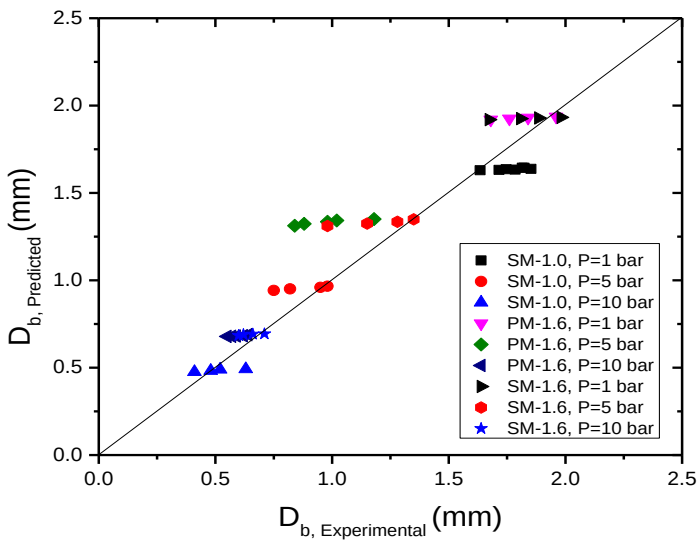

Figure 6.7 Comparison of predicted and experimental bubble departure diameter of microchannel geometries

6.3 VISUALIZATION POOL BOILING ON ROUGH SURFACE

6.3.1 Mechanism of bubble growth

Table 6.2 illustrates the boiling phases observed for R_a=4.03 μm at different pressures. It is observed that the discrete bubble forms at the onset of boiling and number of such discrete bubbles increases with increase in the wall superheat. The moment at which entire surface is covered by discrete bubbles is termed as fully developed nucleate

boiling phase. Thereafter, vertical bubble coalescence is observed which forms vapor column over the nucleation site.

Table 6.2 Boiling phases for R_a=4.03 μm at different pressures

Pressure	Onset of boiling	Nucleate boiling	Fully developed Nucleate boiling	Vapor blanket (CHF)
P=1 bar	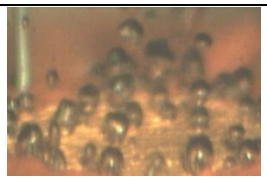	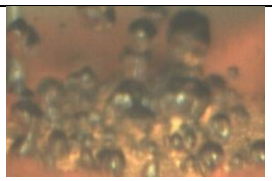	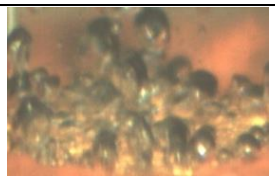	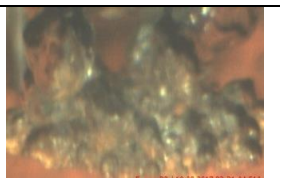
	q'' = 270.82 kWm^2	q'' = 553.50 kWm^2	q'' = 787.02 kWm^2	q'' = 1690.78 kWm^2
P=5 bar	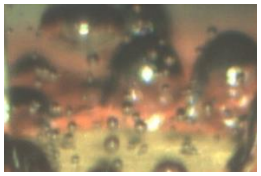	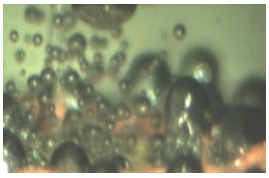	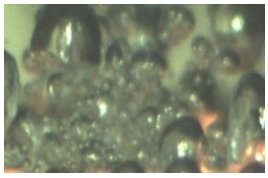	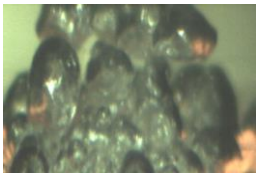
	q'' = 257.02 kWm^2	q'' = 551.81 kWm^2	q'' = 1194.99 kWm^2	q'' = 2025.78 kWm^2
P=10 bar	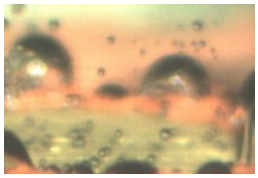	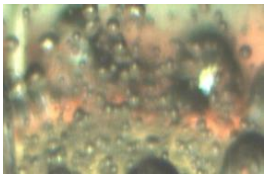	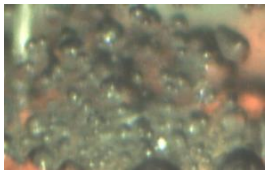	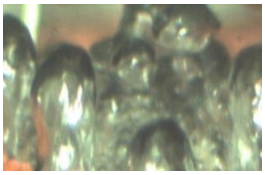
	q'' = 287.35 kWm^2	q'' = 694.29 kWm^2	q'' = 1458.03 kWm^2	q'' = 2543.40 kWm^2

The horizontal bubble coalescence is retarded due to capillary action in the unidirectional scratches as shown in Figure 6.8. This ensures the continuous liquid supply to the nucleation sites which retard the vapor from spreading over the entire surface. Thus heat transfer increases due to increase in the R_a. The time interval between ONB and CHF, so called as period of nucleate boiling, is estimated from the video recorded during each trial. It is found that the period of nucleate boiling increases with the R_a. At high heat flux, bubble spreads horizontally to form vapor blanket over the entire surface. At this moment a large vapor bubble occupies the complete surface. This vapor blanket acts as a barrier for the heat transfer from the surface to the liquid which results in the reduction of HTC. The phase which has upper limit of heat transfer is recognized as CHF.

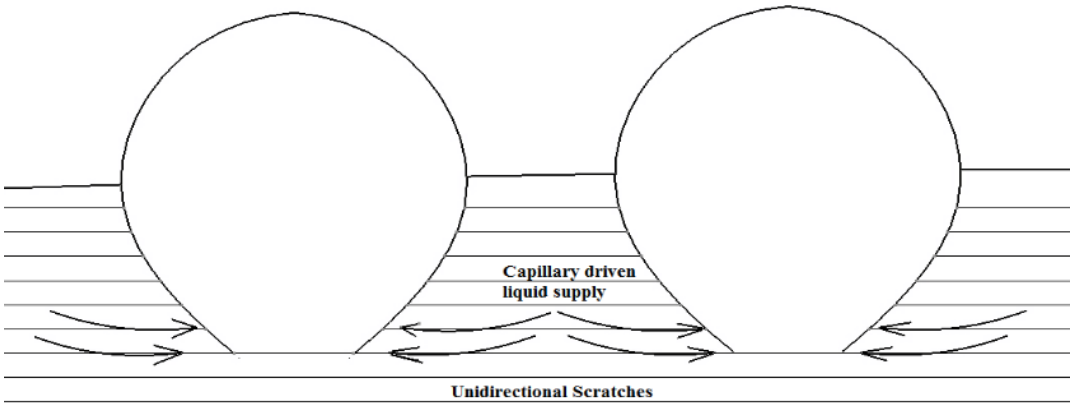

Figure 6.8 Liquid supply through unidirectional scratches

6.3.2 Bubble departure diameter

At each steady-state condition, boiling videos are recorded at 1 bar, 5 bar and 10 bar system pressure for the samples of wide range of R_a. The video is recorded upto the moment of bubble coalescence. Frames of isolated bubbles are selected from the recorded video to measure the bubble departure diameter. The bubble diameter measured for the sample of different R_a is plotted as a function of *Ja* at different pressures as shown in Figure 6.9.

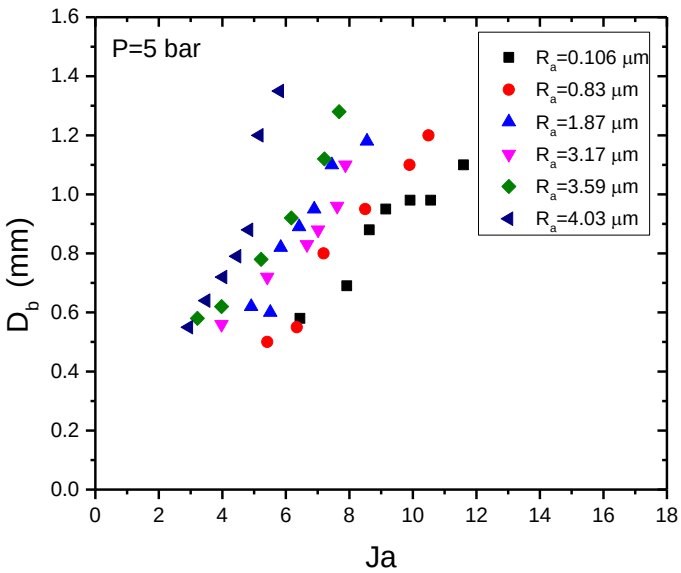

(a)

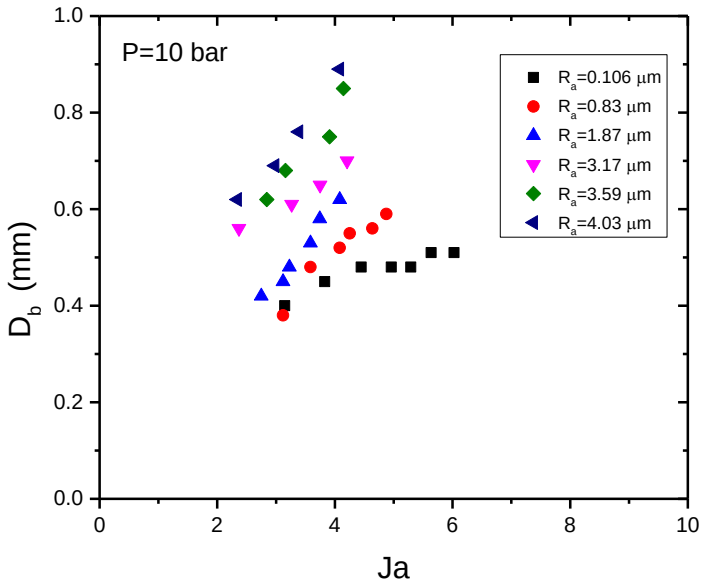

(b)

Figure 6.9 Variation in the bubble departure diameter with Jakob number at (a) P=5 bar (b) P=10 bar

It illustrates that the bubble departure diameter increases linearly with increase in *Ja* at all pressures. It is found that the wall superheat temperature reduced with increase in the R_a. The bubble departure diameter found to be increased with increase in R_a at given *Ja*. In the present study, unidirectional scratches, which act as a liquid supply passage to the nucleated bubble, are made from different grit of SiC sandpaper. The spacing between two unidirectional scratches and R_a increased with decrease in the grit number of SiC sandpaper. Abrasive particle size becomes larger for less grit number which resulted in the higher cavity size of the nucleation site. This enlarges the bubble during its initial growth period. Combined effect of cavity size and unidirectional scratches resulted in the increase in the bubble departure diameter. It is also found that bubble departure diameter decreases with increase in the system pressure. The forces acting on the growing bubble need to be considered to justify this phenomena. Bubble nucleated on the upward facing surface experiences upward acting forces viz. buoyancy and lift force whereas hydrostatic and surface tension forces act against the bubble growth. The surface tension force decreases with increase in the temperature. The bubble detaches from the surface immediately after its initial growth phase. Hence bubble departure

diameter decreased with increase in pressure resulting in tiny bubbles departing from the surface.

The correlation for bubble departure diameter available in the literature is in the form of $[\sigma/(g(\rho_l - \rho_v))]^{0.5}$. The measured bubble departure diameter is compared with that predicted by the correlation of Cole (1967), Cole and Rohsenow (1969) and Cole and Shulman (1966). The variation in the predicted bubble departure diameter with the experimental one for the smooth surface of R_a=0.106 μm at 1 bar, 5 bar and 10 bar system pressure is shown in Figure 6.10. The MAE and percentage deviation is considered for the statistical evaluation. MAE between predicted and experimental bubble departure diameter are given in Table 6.3. The overall MAE of the predicted values by correlation of Cole (1967), is below 20% for all experimental conditions considered in the present work. It is found in Figure 6.10 that the correlation of Cole and Rohsenow (1969) and Cole and Shulman (1966) overpredicts the bubble departure diameter at P=1 bar whereas experimental values are higher than that of the predicted values at P=5 bar and P=10 bar. The bubble departure diameter predicted by Cole (1967), is a function of *Ja* only whereas, correlation of Cole and Rohsenow (1969) and Cole and Shulman (1966) predicts the bubble departure diameter as a function of saturation temperature and pressure, respectively. As it is found in the present study that bubble departure diameter is the function of both, *Ja* and pressure, the variation in the predicted and experimental values are considerably high.

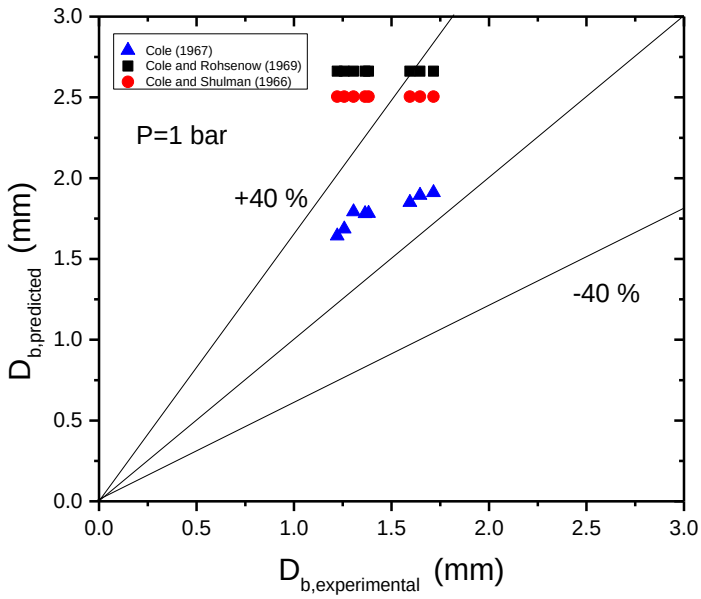
Cole (1967)
Cole and Rohsenow (1969)
Cole and Shulman (1966)
P=1 bar
+40 %
-40 %
$D_{b,predicted}$ (mm)
$D_{b,experimental}$ (mm)
0.0
0.5
1.0
1.5
2.0
2.5
3.0

(a)

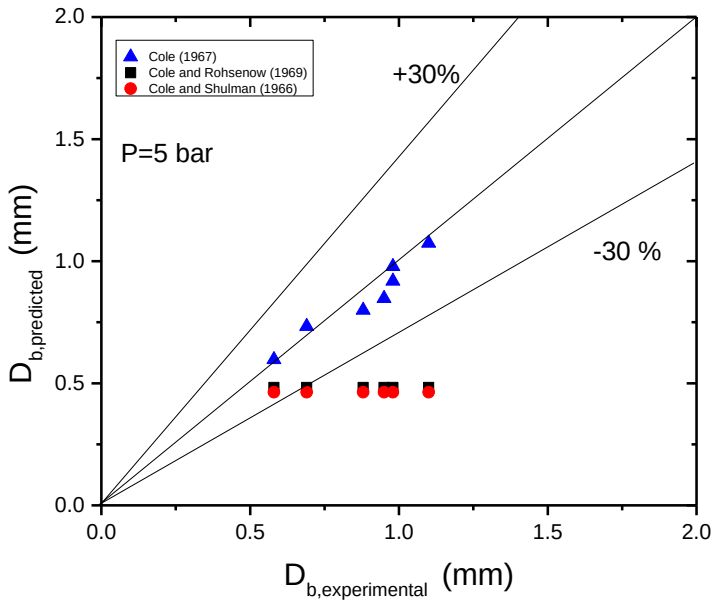
Cole (1967)
Cole and Rohsenow (1969)
Cole and Shulman (1966)
P=5 bar
+30%
-30 %
$D_{b,predicted}$ (mm)
$D_{b,experimental}$ (mm)
0.0
0.5
1.0
1.5
2.0

(b)

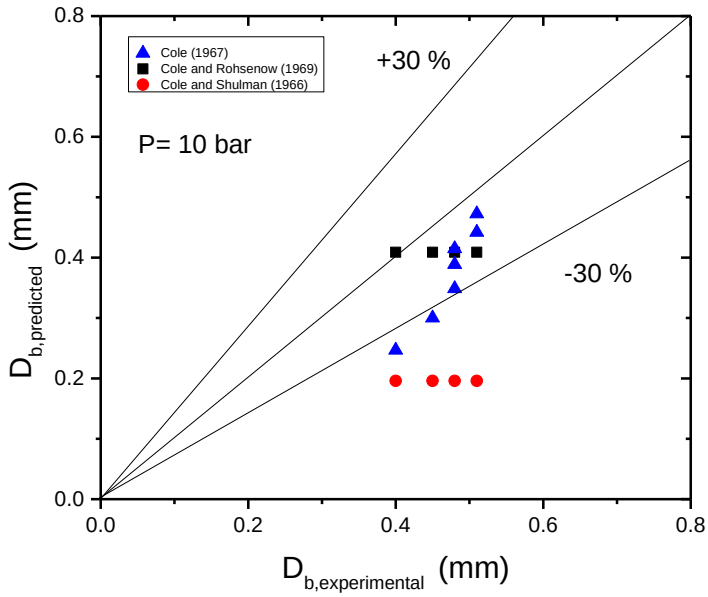

(c)

Figure 6.10 Variation in the predicted bubble departure diameter with the corresponding experimental values of R_a=0.106 μm at (a) P=1 bar (b) P=5 bar (c) P=10 bar

Table 6.3 MAE between predicted and measured bubble departure diameter

Correlation	P=1 bar	P=5 bar	P= 10 bar
Cole (1967)	25.95%	5.42%	21.75%
Cole and Rohsenow (1969)	88.09%	42.66%	13.64%
Cole and Shulman (1966)	76.96%	44.97%	58.29%

6.3.3 Correlation for bubble departure diameter

Forces in bubble dynamics classified as the unsteady growth force, buoyancy force, surface tension, lift force and bubble inertia are considered in force balance as given in Equation 6.10. Bubble departs from the surface as upward acting forces on the bubble exceed the downward acting forces. The bubble departure diameter is measured at the detachment of the bubble from the surface. Considering the force balance, the

correlation for bubble departure diameter is developed in the present work as described below.

$$F_{duy} + F_{st} + F_{bi} = F_{buy} + F_L \tag{6.10}$$

$$\frac{\pi}{6} {D_b}^3 g(\rho_l - \rho_v) + 2\pi\rho_l {D_b}^2 C_L \left(\frac{dr}{dt}\right)^2 = 2\pi r_d \sigma \sin\theta + \frac{3\pi}{8} C_s \rho_l {D_b}^2 \left(\frac{dr}{dt}\right)^2 + \frac{\pi}{8}\rho_l {D_b}^3 \frac{d^2r}{dt^2} + \frac{\pi}{6}\rho_v {D_b}^3 \frac{d^2r}{dt^2} + \pi\rho_v {D_b}^2 \left(\frac{dr}{dt}\right)^2 \tag{6.11}$$

Rearranging the above terms,

$$\frac{\pi}{6} {D_b}^3 g(\rho_l - \rho_v) = 2\pi r_d \sigma \sin\theta + \left[\frac{3C_s\rho_l}{8} - 2C_L\rho_l + \rho_v\right] \pi {D_b}^2 \left(\frac{dr}{dt}\right)^2 + \frac{\pi}{2}\left[\frac{\rho_l}{4} + \frac{\rho_v}{3}\right] {D_b}^3 \frac{d^2r}{dt^2} \tag{6.12}$$

As $\rho_l \gg \rho_v$ the summation of ρ_l and ρ_v is approximated to ρ_l.

$$\frac{\pi}{6} {D_b}^3 g(\rho_l - \rho_v) = 2\pi r_d \sigma \sin\theta + \left[\frac{3C_s}{8} - 2C_L\right] \pi\rho_l {D_b}^2 \left(\frac{dr}{dt}\right)^2 + \frac{\pi}{8}\rho_l {D_b}^3 \frac{d^2r}{dt^2} \tag{6.13}$$

Dividing Equation (6.13) by $\frac{\pi\sigma D_b}{6}$

$$\frac{{D_b}^2 g(\rho_l - \rho_v)}{\sigma} = \frac{12 r_d \sin\theta}{D_b} + \left[\frac{3C_s}{8} - 2C_L\right] \frac{6\rho_l D_b}{\sigma} \left(\frac{dr}{dt}\right)^2 + \frac{3\rho_l {D_b}^2}{4\sigma} \left(\frac{d^2r}{dt^2}\right) \tag{6.14}$$

The bubble growth can be formulated from the heat balance between conduction heat transfer through the microlayer and latent heat transfer by the bubble. Thus bubble growth rate can be expressed as given in Equation (6.15).

$$\frac{dr}{dt} = C_t \frac{k\Delta T}{R\rho_v h_{fg}} \tag{6.15}$$

$$\frac{d^2r}{dt^2} = \left(\frac{-2}{D_b}\right)\left(\frac{dr}{dt}\right)^2 \tag{6.16}$$

Equation (6.17) is derived from Equation (6.14), Equation (6.15) and Equation (6.16).

$$\frac{{D_b}^2 g(\rho_l-\rho_v)}{\sigma} = \frac{12 r_d \sin\theta}{D_b} + \left[\frac{3C_s}{8} - 2C_L\right]\left(\frac{6\rho_l D_b}{\sigma}\right)\frac{{C_t}^2 k^2 \Delta T^2}{R^2 {\rho_v}^2 {h_{fg}}^2} + \frac{3\rho_l {D_b}^2}{4\sigma}\left(\frac{-2}{D_b}\right)\frac{{C_t}^2 k^2 \Delta T^2}{R^2 {\rho_v}^2 {h_{fg}}^2} \quad (6.17)$$

$$B_o^{\frac{3}{2}} = \frac{12 r_d \sin\theta}{D_b}\left(B_o^{\frac{1}{2}}\right) + \left[9C_s {C_t}^2 - 48 C_L {C_t}^2 - 6{C_t}^2\right] K_l \quad (6.18)$$

Where $B_o = \frac{{D_b}^2 g(\rho_l-\rho_v)}{\sigma}$, $K_l = \left(\frac{Ja}{Pr_l}\right)^2 Ar^{-1}$, $Ar = \left[\frac{g\rho_l(\rho_l-\rho_v)}{\mu_l^2}\right]\left[\frac{\sigma}{g(\rho_l-\rho_v)}\right]^{3/2}$

The dry-out radius of the bubble at departure is very small compared to the bubble departure diameter, hence the value of r_d/D_b will be close to zero and thus first term in Equation (6.18) is neglected. The proportional relation of B_o with K_l is expressed in Equation (6.19).

$$B_o^{\frac{3}{2}} \sim \left[9C_s {C_t}^2 - 48 C_L {C_t}^2 - 6{C_t}^2\right] K_l \quad (6.19)$$

In order to fit the experimental data, the linear dependence can be written as given in Equation (6.20).

$$B_o^{\frac{1}{2}} = (\omega_1 + \omega_2 K_l)^{\frac{1}{3}} \quad (6.20)$$

Based on the experimental data, the fitting parameters ω_1 and ω_2 are obtained. The relationship between B_o and K_l is presented in Equation (6.21).

$$B_o^{\frac{1}{2}} = (0.02 + 1018.5)^{\frac{1}{3}} \quad (6.21)$$

The final expression of the present correlation for bubble departure diameter of the sample of R_a ranging from 0.106 μm to 4.03 μm at 1 bar, 5 bar and 10 bar system pressure is given in Equation (6.22).

$$D_b = (0.02 + 1018.5 K_l)^{\frac{1}{3}}\left[\frac{\sigma}{g(\rho_l-\rho_v)}\right]^{\frac{1}{2}} \quad (6.22)$$

Similar form of correlation is derived by Chen et al. (2017), for the prediction of bubble departure diameter of methane. Figure 6.11 shows the comparison between the predicted and experimental values of bubble departure diameter. The predicted bubble

departure diameter is within ±30 % deviation. The MAE between predicted and experimental values of the bubble diameter is 17.83%. It illustrate that values predicted by the present correlation are in good agreement with the experimental values.

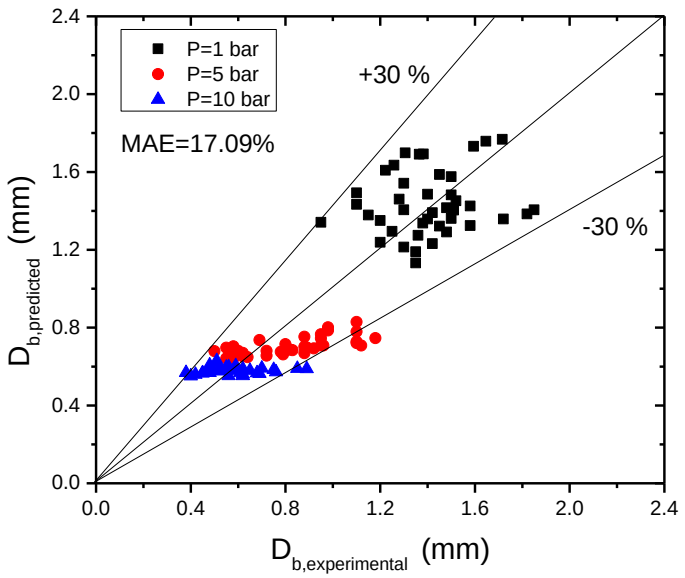

Figure 6.11 Comparison between bubble departure diameter predicted from present correlation and present experimental value

6.3.4 Bubble frequency

The bubble frequency for the sample of different R_a is plotted as a function of *Ja* at different pressure in Figure 6.12. It is observed that bubble frequency increases with increase in the *Ja*. It is also observed that bubble frequency increases with increase in R_a at constant *Ja* at all the pressures. The bubble growth is classified into two phases viz. initial growth stage and final growth stage. Initial stage is dominated by the heat transfer whereas the kinetic effect plays significant role during final stage of the bubble growth. The enhanced heat transfer due to increase in R_a stimulate the initial stage of bubble growth wherein hemispherical bubble grows over the nucleation cavity.

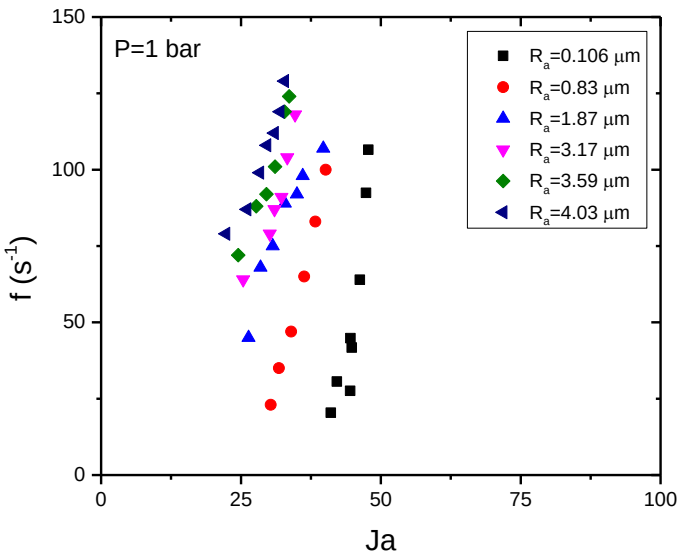

(a)

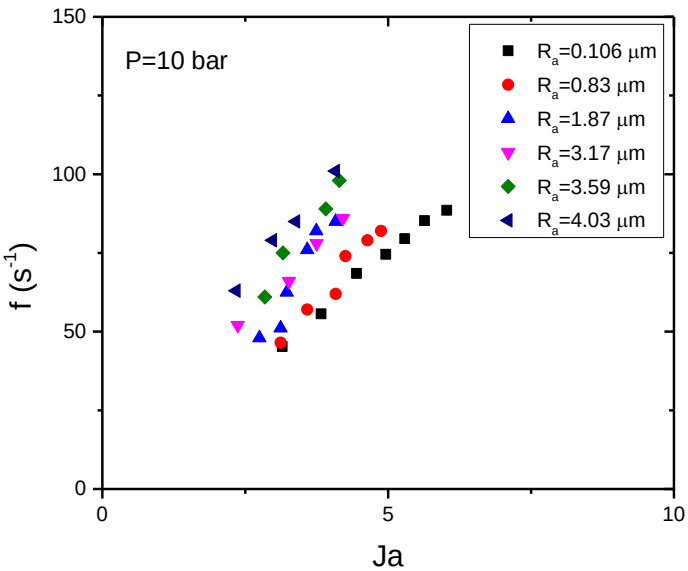

(b)

Figure 6.12 Variation in bubble frequency with Jakob number at (a) P=1 bar (b) P=10 bar

Thus bubble growth period substantially dropped with the increase in heat flux and *Ja*. The bubble dynamics plays vital role in the final stage of bubble growth. Buoyancy force becomes dominant as the bubble grows larger in diameter in its initial stage of

growth. This leads to the early bubble departure. Thus overall growth period decreases with increase in *Ja*. The unidirectional scratches offer intense liquid supply through capillary action. The liquid rushes towards the bubble base which causes vapor to get entrapped at the bubble neck. Thus waiting period between two consecutive bubble nucleation decreased with increase in wall superheat. At high heat flux, waiting period is found to be negligible. The combined reduction in growth period and waiting period resulted in the increase in bubble frequency.

6.3.5 Correlation for bubble frequency

The correlations used in the present study to compare the experimental data are in the form of fD_b^n. The values of $fD_b^{1/2}$and fD_b at different pressure is obtained from the experimental data for R_a=0.106 μm and compared with the value predicted from correlations of Cole (1960), Zuber (1963) and Jakob and Fritz (1931) as shown in Figure 6.13 (a) (b) and (c), respectively. At 5 bar and 10 bar pressure, correlation of Cole (1960) predicted the experimental value of $fD_b^{1/2}$within ±40% deviation with MAE of 28.71% whereas it predicts the experimental value at 1 bar beyond +40% deviation. The correlation of Zuber (1963) is based on the thermo-physical properties of the liquid and thus the predicted fD_b varies with the pressure, as shown in Figure 6.13(b). It predicts the experimental fD_b within ±40% deviation for 1 bar and 5 bar pressure whereas predicted fD_b found to beyond +40% deviation from the experimental values at 10 bar. The correlation of Jakob and Fritz (1931) predicts the experimental fD_b similar to that of Zuber (1963).

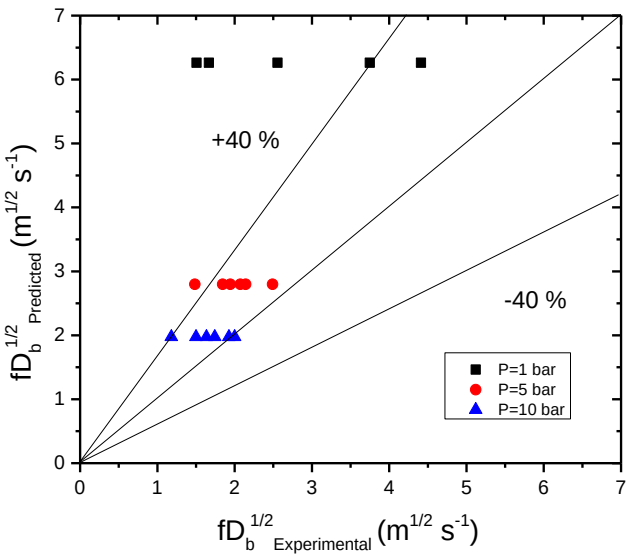
+40 %
-40 %
P=1 bar
P=5 bar
P=10 bar
$fD_b^{1/2}$ Predicted ($m^{1/2}$ s^{-1})
$fD_b^{1/2}$ Experimental ($m^{1/2}$ s^{-1})

(a)

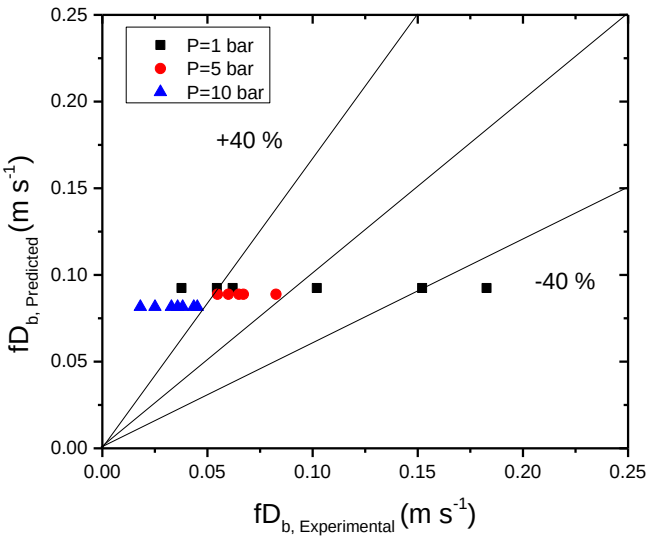
P=1 bar
P=5 bar
P=10 bar
+40 %
-40 %
$fD_{b,\ Predicted}$ (m s^{-1})
$fD_{b,\ Experimental}$ (m s^{-1})

(b)

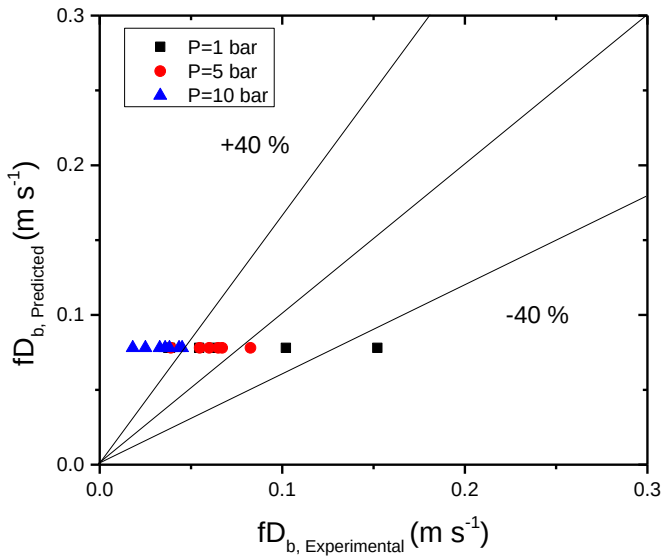

(c)

Figure 6.13 Comparison of predicted fD_b^n by (a) Cole (1960) (b) Zuber (1963) (c) Jakob and Fritz (1931) with the corresponding experimental value

The correlations considered in the present study can not predict the experimental data at different R_a. In this study, pool boiling of water with the sample of different R_a at pressure upto 10 bar is carried. The correlation is developed in the form of fD_b^2 by fitting the experimental data of the present study. The form of correlation is developed by considering the bubble waiting period, bubble growth period and bubble growth rate. Bubble frequency (*f*), as given in Equation (6.23), is the reciprocal of sum of growth period and waiting period of the bubble.

$$f = \frac{1}{t_g + t_w} \tag{6.23}$$

Inertial controlled bubble growth on the structured surface, is a linear function of time as suggested by Chen et al. (2017), can be expressed as given in Equation (6.24).

$$\frac{dr}{dt} = \frac{C_t k \Delta T}{R \rho_v h_{fg}} = \frac{C_t Ja \propto_l}{R} \tag{6.24}$$

where C_t is proportionality constant.

Bubble growth period (t_g) is the transient bubble growth from its nucleation till the departure. R is the bubble radius at its departure. Integrating the Equation (6.24),

$$\int_0^R R dr = C_t Ja \propto_l \int_0^{t_g} dt \tag{6.25}$$

$$t_g = \frac{R^2}{2C_t Ja \propto_l} \tag{6.26}$$

The waiting period (t_w) is defined as the time interval from the detachment of a preceding bubble to the nucleation of a following bubble. Liquid replenishment towards the nucleation site takes place immediately after the bubble departure. Thermal layer develops over the nucleation site during the waiting period of the bubble cycle. The thickness of thermal layer developed during this period is given by Cooper (1969) and is expressed in Equation (6.27).

$$\delta = (\pi \propto_l t_w)^{\frac{1}{2}} \tag{6.27}$$

$$t_w = \frac{\delta^2}{\pi \propto_l} \tag{6.28}$$

Kutateladze and Gogonin (1979) suggested that the radius of the bubble is proportional to the microlayer developed beneath it. Thus, considering $\delta = xR$, Equation (6.28) becomes,

$$t_w = \frac{x^2 R^2}{\pi \propto_l} \tag{6.29}$$

Combining Equation (6.19), Equation (6.26) and Equation (6.29), bubble frequency is expressed as given in Equation (6.30).

$$f = \frac{8\pi C_t Ja \propto_l}{{D_b}^2(\pi + 2x^2 CJa)} \tag{6.30}$$

The form of the correlation is expressed in terms of $f{D_b}^2$ in Equation (6.31) where ω_3 and ω_4 are the fitting parameters.

$$\frac{fD_b{}^2}{Ja\propto_l} = \frac{8\pi C_t}{(\pi+2x^2C_tJa)} = \frac{\omega_3}{\pi+\omega_4 Ja} \tag{6.31}$$

Considering experimental data, the fitting parameters are obtained. Thus correlation for the relation between bubble departure diameter and bubble frequency is developed as given in Equation (6.32).

$$fD_b{}^2 = \left(\frac{43.07}{1+3.18\times10^{-4}Ja}\right) Ja \propto_l \tag{6.32}$$

Figure 6.14 shows the variation in the predicted $fD_b{}^2$ with experimental values at pressure of 1 bar, 5 bar and 10 bar. The deviation between predicted and experimental $fD_b{}^2$ is found within ±30 for all the pressures. The correlation developed in the present study can predict the experimental value with MAE of 25.26%. Thus it is commented that present correlation is in good agreement with the experimental values in investigated range of R_a varying from 0.106 μm to 4.03 μm at pressure upto 10 bar.

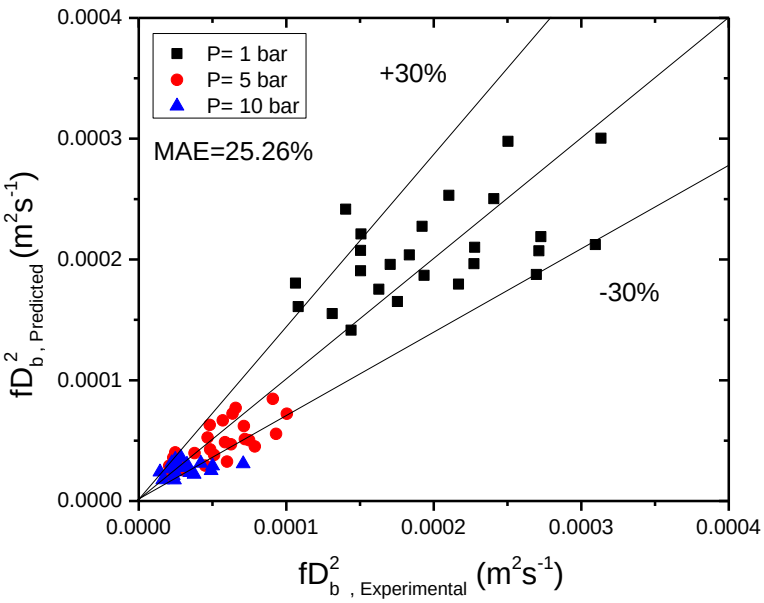

Figure 6.14 Comparison of present correlation for $fD_b{}^2$ with the experimental value

CHAPTER 7

CONCLUSION AND SCOPE FOR FUTURE WORK

The important aspects of pool boiling heat transfer from rough surface and microchannel geometries under steady and transient heat supply was investigated. Experiments were conducted under saturated condition of distilled water at pressures 1 bar, 5 bar and 10 bar under steady and transient heat supply. The surface roughness value R_a was varied from 0.106 μm to 4.03 μm. Three different channel profiles namely, square, parabolic and stepped, were fabricated on the top surface of 20 mm diameter copper sample. The effect of surface roughness and microchannel profile on bubble dynamics and CHF during pool boiling under steady and transient heat supply was studied. Effect of time constant on transient CHF for sample of rough surface and microchannel geometries was extensively examined. High speed camera is used to observe the transition mechanism of boiling phase during steady and exponential heat supply. CHF model for rough samples based on force balance approach was developed. Forces acting on the bubble were considered to predict the bubble parameters. Following conclusions are drawn from this research work.

7.1 CONCLUSIONS

- The steady and transient CHF are found to be increased with increase in the surface roughness. Improved wettability and increased nucleation site density have resulted in the CHF enhancement. Transient CHF enhancement for R_a=4.03 μm when γ=1 is found to be 98.88%, 76.55% and 53.21% at pressures P=1 bar, P=5 bar and P=10 bar, respectively, however it is found to be lower by 9.38%, 21.40% and 9.73%, compared to steady state CHF enhancement for R_a=4.03 μm, at respective pressures.
- Improved liquid supply through the channel space and significant bubble growth resulted in the CHF enhancement by all the microchannel geometries. CHF enhancement for SM-1.6 μm during steady and exponential heat supply of γ=1 is found to be 159.51% and 131.36%, respectively, at P=1 bar.

- CHF increased with increase in the pressure at both the condition viz. steady and transient. Steady-state CHF for R_a=4.03 μm and SM-1.6 at P=10 bar is found to be 71.43% and 47.37% higher compared to the CHF at P=1 bar, respectively.
- Transient CHF gradually decreased with increase in γ due to liquid-vapor instability during exponential heat supply. At P=10 bar, the transient CHF for R_a=1.87 μm and PM-1.6 are found to be decreased by 9.12% and 15.87% due to increase in the γ from 1 to 6, respectively.
- It is found during steady-state heat supply that CHF for square microchannel is lower than the CHF for R_a=3.17 μm however, CHF for parabolic and stepped microchannel is higher than that for the surface roughness upto R_a=3.17 μm. The steady-state CHF for R_a=4.03 μm, parabolic and stepped microchannel are almost in the same range.
- Modified Gorenflo correlation, which includes the non-dimensional time constant γ, predicts the present transient HTC values with MAE of 14.91%.
- The present CHF model, which includes the bubble angle, time constant and roughness parameters viz. R_a and S_m, predicts the experimental values of transient CHF with MAE of 11.89%.
- Bubble dynamics during pool boiling of saturated water was significantly affected by the surface characteristics i.e. surface roughness and microchannel.
- At 1 bar pressure, bubble departure diameter for all the samples of rough surface varied from 1.0 mm to 1.8 mm whereas, for microchannel geometries, it varied from 1.6 mm to 2.3 mm.
- Bubble departure diameter and bubble frequency is found to be influenced by the channel top width and the surface roughness value.
- Bubble departure diameter remarkably reduced due to increase in the pressure from 1 bar to 5 bar, however, the bubble departure diameter at 5 bar and 10 bar found to be in the same range.
- Bubble departure diameter is found to be independent on the state of heating viz. steady and quasi-steady for all the samples. However, bubble frequency increased during quasi-steady heat supply due to considerable drop in the

bubble waiting period compared to the steady-state condition. During transient heat supply, vertical bubble coalescence is noticed at high heat flux range.

- It is observed during visualization study that tiny bubbles form over the surface and depart quickly at high pressure. Surface wettability increases with increase in temperature and thus, liquid replenishment takes place immediately after the bubble departure. Hence, prolonged nucleated boiling regime is noticed for rough surface at high pressure.
- Horizontal coalescence which leads the bubble spreading over the surface is responsible for the formation of vapor film over the surface. Bubble coalescence is retarded due to capillary action in the unidirectional scratches. Channel profile does not have an influence on the wettability, hence, bubble generated in the channel spreads rapidly during rapid transients and thus, liquid supply to the channel gets obstructed which results in the quick formation of vapor film.
- Forces acting vertically on the growing bubble are considered to predict the bubble departure diameter. The MAE between measured and predicted bubble departure diameter for the rough surface and the microchannel geometries at all pressure is 17.09% and 13.30%, respectively.

7.2 SCOPE FOR FUTURE WORK

- The research work may be extended to examine the pool boiling heat transfer from hybrid microchannel i.e. rough microchannel geometries.
- The experimental study of pool boiling can be carried out by adopting compound enhancement technique like rough and microchannel geometries with surface vibration.
- Transient pool boiling heat transfer and bubble morphology of superhydrophilic surface during exponential heat supply can be examined.

REFERENCES

Ahn, H. S., Lee, C., Kim, H., Jo, H., Kang, S., Kim, J., Shin, J. and Kim, M. H. (2010). "Pool boiling CHF enhancement by micro-nanoscale modification of zircaloy-4 surface." *Nuclear Engineering and Design*, 240, 3350–3360.

Ahn, H. S., Jo, H. J., Kang, S. H. and Kim, M. H. (2011). "Effect of liquid spreading due to nano/ microstructures on the critical heat flux during pool boiling." *Appl. Phys. Lett.*, 98, 071908.

Anderson, T. M. and Mudawar, I. (1989). "Microelectronic Cooling by Enhanced Pool Boiling of a Dielectric Fluorocarbon Liquid." *J. of Heat Transfer*, 111, 752-759.

Balakin, B. V., Delov, M. I., Kuzmenkov, D. M., Kutsenko, K.V., Lavrukhin, A. A. and Marchenko, A. S. (2017). "Boiling crisis in cryogenic fluids during unsteady heat supply." *Int. J. Heat Mass Transf.*, 111, 1107–1111.

Bhavnani, S. H., Fournelle, G. and Jaeger, R. C. (2001). "Immersion-Cooled Heat Sinks for Electronics Insight from High-Speed Photography." *IEEE Transactions on Components and Packaging Technologies*, Vol. 24, No. 2, 166-176.

Benjamin, R. J. and Balakrishnan, A. R. (1997). "Nucleation site density in pool boiling of saturated pure liquids: effect of surface micro-roughness and surface and liquid physical properties." *Exp. Thermal Fluid Sci.*, 15, 32–42.

Chang, Y. P. (1961). "An Analysis of the Critical Conditions and Burnout in Boiling Heat Transfer." *USAEC Rep*. TID-14004, Washington, DC.

Chen, H., Chen, G., Zou, X., Yao, Y. and Gong, M. (2017). "Experimental investigations on bubble departure diameter and frequency of methane saturated nucleate pool boiling at four different pressures." *Int. J. Heat Mass Transf.*, 112, 662–675.

Chien, L. and Webb, R. L. (1998). “Visualization of pool boiling on enhanced surfaces.” *Exp. Thermal Fluid Sci.*, 16, 332-341.

Cole, R. (1960). “A photographic study of pool boiling in the region of the critical heat flux.” *AIChE J.*, 6 (4), 533–538.

Cole, R. (1967). “Bubble frequencies and departure volumes at subatmospheric pressures.” *AIChE J.*, 13 (4), 779–783.

Cole, R. and Rohsenow, W. M. (1969). “Correlation of bubble diameters of saturated Liquids.” *Chem. Eng. Prog. Symp. Ser.*, 65 (92), 211–213.

Cole, R. and Shulman, H. L. (1966). “Bubble departure diameters at subatmospheric pressures,” *Chem. Eng. Prog. Symp. Ser.*, 62 (64), 6–16.

Cooke, D. and Kandlikar, S. G. (2012). “Effect of open microchannel geometry on pool boiling enhancement.” *Int. J. Heat Mass Transf.*, 55, 1004–1013.

Cooke, D. and Kandlikar, S. G. (2011). “Pool Boiling Heat Transfer and bubble dynamics over plain and enhanced microchannel.” *J. Heat Transfer*, 133(5), 1-9.

Cooke, D. and Kandlikar, S. G. (2012). “Effect of open microchannel geometry on pool boiling enhancement.” *Int. J. Heat Mass Transf.*, 55, 1004–1013.

Cooper, M. G. (1984). “Saturation nucleate pool boiling-a simple correlation.” In: *National Conference on Heat Transf.*, Permagon Press, Elmsford, NY, pp. 785–793.

Cooper, M. G. and Lloyd, A. J. P. (1969). “The microlayer in nucleate pool boiling.” *Int. J. Heat Mass Transf.*, 12, 895– 913.

Deev, V. I., Oo, H. L., Kharitonov, V. S., Kutsenko, K. V. and Lavrukhin, A. A. (2007). “Critical heat flux modeling in water pool boiling during power transients.” *Int. J. Heat Mass Transf.*, 50, 3780–3787.

Dharmendra, M., Suresh, S., Sujith Kumar, C. S. and Qiaqin Yang (2016). “Pool boiling heat transfer enhancement using vertically aligned carbon nanotube coatings on a copper substrate.” *Appl. Ther. Engg.*, 99, 61–71.

Dong, L., Quan, X. and Cheng, P. (2014). “An experimental investigation of enhanced pool boiling heat transfer from surfaces with micro/nano-structures.” *Int. J. Heat Mass Transf.*, 71, 189–196.

Drach, V., Sack, N. and Fricke, J. (1996). “Transient heat transfer from surfaces of defined roughness into liquid nitrogen.” *Int. J. Heat Mass Transf.*, 39(9), 1953-1961.

Duluc, M., Benoit Stutz, B., and Lallemand, M. (2004). “Transient nucleate boiling under stepwise heat generation for highly wetting fluids.” *Int. J. Heat Mass Transf.*, 47, 5541–5553.

El-Genk, M. S. (2008). “On the introduction of nuclear power in Middle East countries: Promise, strategies, vision and challenges.” *Energy Conversion Management*, 49, 2618–2628.

Fukuda, K., Shiotsu, M. and Sakurai, A. (2000). “Effect of surface conditions on transient critical heat fluxes for a horizontal cylinder in a pool of water at pressures due to exponentially increasing heat inputs.” *Nuclear Engineering and Design*, 200, 55–68.

Ghiu, C. and Joshi, Y. K. (2005). “Visualization study of pool boiling from thin confined enhanced structures.” *Int. J. Heat Mass Transf.*, 48, 4287–4299.

Gorenflo, D. (1993). “Pool Boiling.” *VDI Heat Atlas*, VDI Verlag, Düsseldorf.

Gong, S. and Cheng, P. (2017). “Direct numerical simulations of pool boiling curves including heater’s thermal responses and the effect of vapor phase’s thermal conductivity.” *Int. Commun. Heat Mass Transf.*, 87, 61–71.

Haramura, Y. and Katto, Y. (1983). “A new hydrodynamic model of critical heat flux, applicable widely to both pool and forced convection boiling on submerged bodies in saturated liquids.” *Int. J. Heat Mass Transf.*, 26, 389-399.

Htet, M. H., Fukuda, K. and Liu, Q. (2016). “Transient boiling critical heat flux on horizontal vertically oriented ribbon heater with treated surface condition in pool of water.” *Mechanical Engineering Journal*, 3(3), 1-19.

http://www.putnamlabs.com

Hosseini, R., Gholaminejad, A. and Nabil, M. (2011). “Concerning the effect of surface material on nucleate boiling heat transfer of R-113.” *J. Electron. Cooling Thermal Control*, 1, 22–27.

Howard, A. H. and Mudawar, I. (1999). “Orientation effects on pool boiling critical heat flux (CHF) and modeling of CHF for near-vertical surfaces.” *Int. J. Heat Mass Transf.*, 42, 1665–1688.

Jaikumar, A. and Kandlikar, S. G. (2016). “Ultra-high pool boiling performance and effect of channel width with selectively coated open microchannel.” *Int. J. Heat Mass Transf.*, 95, 795–805.

Jakob, M. and Fritz, W. (1931). “Versuche über den Verdampfungsvorgang,” *Forschung im Ingenieurwesen*, 2 (12), 435–447.

Johnson, H. A. (1971). “Transient boiling heat transfer to water.” *Int. J. Heat Mass Transf.*, 14, 67-82.

Jones, B. J., McHale, J. P. and Garimella, S. V. (2009). “The Influence of Surface Roughness on Nucleate Pool Boiling Heat Transfer.” *J. Heat Transfer*, 131, 1-14.

Kandlikar, S. G. (2001). “A Theoretical model to predict pool boiling CHF incorporating effects of contact angle and orientation.” *J. Heat Transfer*, 123, 1071–1079.

Kang, M. G. (2000). “Effect of surface roughness on pool boiling heat transfer.” *Int. J. Heat Mass Transf.*, 43, 4073–4085.

Kedzierski, M. A. and Fick, S. E. (2015). "Effect of Acoustic Excitation on R134a/Al_2O_3 Nanolubricant Mixture Boiling on a Reentrant Cavity Surface." *J. Heat Transfer,* 137 (11), 111503-111503-9.

Kim, J., Jun, S., Laksnarain, R. and You, S. M. (2016). "Effect of surface roughness on pool boiling heat transfer at a heated surface having moderate wettability." *Int. J. Heat Mass Transf.,* 101, 992–1002.

Kim, J., Jun, S., Lee, J., Godinez, J. and You, S. M. (2017). "Effect of Surface Roughness on Pool Boiling Heat Transfer of Water on a Superhydrophilic Aluminum Surface." *J. of Heat* Transfer, 139, 1-9.

Kirishenko, Y. A. and Cherniakov, P. S. (1973). "Determination of the first critical thermal heat flux on flat heaters." *J. Eng. Phys.*, 20, 699–702.

Klausner, J. F., Mei, R., Bernhard, D. M. and Zeng, L. Z. (1993). "Vapor bubble departure in forced convection boiling." *Int. J. Heat Mass Transf.,* 36 (3), 651–662.

Kruse, C. M., Anderson, T., Wilson, C., Zuhlke, C., Alexander, D., Gogos, G. and Ndao, S. (2015). "Enhanced pool-boiling heat transfer and critical heat flux on femtosecond laser processed stainless steel surfaces." *Int. J. Heat Mass Transf.,* 82, 109–116.

Kutateladze, S. S. (1948). "On the transition to film boiling under natural convection." *Kotloturbostroenie*, 3, 152–158.

Kutateladze, S. S. and Gogonin, I. I. (1979). "Growth rate and detachment diameter of a vapor bubble in free convection boiling of a saturated liquid." *Teplofizika Vysokikh Temperatur*, 17, 792–797.

Lay, J. H. and Dhir, V. K. (1995). "Shape of a vapor stem during nucleate boiling of saturated liquids." *Trans. ASME J. Heat Transfer*, 117, 394-401.

Lee, C. Y., Chun, T. H. and In, W. K. (2014). “Effect of change in surface condition induced by oxidation on transient pool boiling heat transfer of vertical stainless steel and copper rodlets.” *Int. J. Heat Mass Transf.*, 79, 397-407.

Li, Y., Liu, Z. and Zheng, B. (2015). “Experimental study on the saturated pool boiling heat transfer on nano-scale modification surface.” *Int. J. Heat Mass Transf.*, 84, 550–561.

Lienhard, J. H. and Dhir, V. K. (1973). “Hydrodynamic theory of the peak and minimum pool boiling heat fluxes.” *CR*-2270.

Malavasi, I., Teodori, E., Moita, A. S., Moreira, A. L. N. and Marengo, M. (2018). “Wettability effect on pool boiling: a review.” *Encyclopedia of Two-Phase Heat Transfer and Flow III: Macro and Micro Flow Boiling and Numerical Modeling Fundamentals* (A 4-volume Set).” Vol. 4, Edited by J. Thome, World Scientific Publishing Co Pte Ltd. ISBN: 978-981-3227-31-6.

McHale, J. P. and Garimella, S. V. (2010). “Bubble nucleation characteristics in pool boiling of a wetting liquid on smooth and rough surfaces.” *Int. J. Multiphase Flow*, 36, 249–260.

Mehta, J. S. and Kandlikar, S. G. (2013). “Pool boiling heat transfer enhancement over cylindrical tubes with water at atmospheric pressure, Part I: Experimental results for circumferential rectangular open microchannel.” *Int. J. Heat Mass Transf.*, 64, 1205–1215.

Mehta, J. S. and Kandlikar, S. G. (2013). “Pool boiling heat transfer enhancement over cylindrical tubes with water at atmospheric pressure, Part II: Experimental results and bubble dynamics for circumferential V-groove and axial rectangular.” *Int. J. Heat Mass Transf.*, 64, 1216–1225.

Moita, A. S., Teodori, E. and Moreira, A. L. N. (2015). “Influence of surface topography in the boiling mechanisms.” *Int. J. Heat Fluid Flow*, 52, 50–63.

Mostinski, I. L. (1963). “Application of the rule of corresponding states for calculation of heat transfer and critical heat flux.” *Teploenergetika*, 10 (4), 66–71.

Nishikawa, K., Fujita, Y., Ohta, H. and Hidaka, S. (1982). “Effect of the surface roughness on the nucleate boiling heat transfer over the wide range of pressure.” In: *Proc. 7th Int. Heat Transfer Conf.*, Vol. 4, 61–66.

Park, J., Fukuda, K, and Liu, Q. (2012). “CHF Phenomena by Photographic Study of Boiling Behavior due to Transient Heat Input.” *Science and Technology of Nuclear Installations*, 12, 1-12.

Pasamehmetoglu, K. O., Chappidi, P. R., Unal, C. and Nelson, R. A. (1993). “Saturated pool nucleate boiling mechanisms at high heat fluxes.” *Int. J. Heat Mass Transf.*, 36, 3859-3868.

Patil, C. M and Kandlikar, S. G. (2014). “Pool boiling enhancement through microporous coatings selectively electrodeposited on fin tops of open microchannel.” *Int. J. Heat Mass Transf.*, 79, 816–828.

Phan, H., Caney, N., Marty, P. and Colasson, J. (2009). “Surface wettability control by nanocoating: The effects on pool boiling heat transfer and nucleation mechanism.” *Int. J. Heat Mass Transf.*, 52, 5459-5471.

Phan, H., Caney, N., Marty, P., Colasson, S. and Gavillet, J. (2010). “A model to predict the effect of contact angle on the bubble departure diameter during heterogeneous boiling.” *Int. Comm. Heat Mass Transfer*, 37, 964-969.

Phan, H.T., Bertossi, R., Caney, N., Marty, P. and Colasson, J. (2012). “A model to predict the effect of surface wettability on critical heat flux.” *Int. Comm. Heat Mass Transfer*, 39, 1500-1504.

Qu, Z. G., Xu, Z. G., Zhao, C. Y. and Tao, W. Q. (2012). “Experimental study of pool boiling transfer on horizontal metallic foam surface with crossing and single-directional V-shaped groove

in saturated water." *Int. J. Multiphase Flow*, 41, 44–55.

Quan, X., Dong, L. and Cheng, P. (2014). "A CHF model for saturated pool boiling on a heated surface with micro/nano-scale structures." *Int. J. Heat Mass Transf.*, 76, 452–458.

Ramaswamy, C., Joshi, Y., Nakayama, W. and Johnson, W. B. (2003). "Semi-analytical model for boiling from enhanced structures." *Int. J. Heat Mass Transf.*, 46, 4257–4269.

Rosenthal, M. W. (1957). "An experimental study of transient boiling." *Nucl. Sci. Eng.*, 2 640–656.

Sakurai, A. and Shiotsu, M. (1977). "Transient pool boiling heat transfer Part 1: Incipient boiling superheat." *J. Heat transfer*, 99, 547-553.

Sakurai, A. and Shiotsu, M. (1977). "Transient pool boiling heat transfer Part 2: Boiling heat transfer and Burnout." *J. Heat transfer*, 99, 554-560.

Sakurai, A., Shiotsu, M. and Hata, K. (1992). "Boiling heat transfer characteristics for heat inputs with various increasing rates in liquid nitrogen." *Cryogenics*, 32 (5), 421–428.

Sakurai, A., Shiotsu, M., Hata, K. and Fukuda, K. (2000). "Photographic study on transitions from non-boiling and nucleate boiling regime to film boiling due to increasing heat inputs in liquid nitrogen and water." *Nucl. Eng. Des.*, 200, 39–54.

Saeidi, D., Alemrajabi, A. A. and Saeidi, N. (2015). "Experimental study of pool boiling characteristic of an aluminized copper surface." *Int. J. Heat Mass Transf.*, 85, 239–246.

Siegel, R. and Keshock, E. G. (1964). "Effects of reduced gravity on nucleate boiling bubble dynamics in saturated water." *AIChE J.*, 10 (4), 509–517.

Sharma, P. R. (1998). “Determination of heat transfer rates in nucleate pool boiling of pure liquids for a wide range of pressure and heat flux.” *In: Proceedings of the 11th International Heat Transfer Conference, Kyongju, South Korea*, Vol. 2, 467–472.

Stephan, K. (1963). “Mechanismus und Modellgesetz des Wärmeübergangs bei der Blasenverdampfung.” *Chemie-Ingenieur-Technik*, 35 (11), 775–784.

Su, G. Y., Bucci, M., McKrell, T. and Buongiorno, J. (2016). “Transient boiling of water under exponentially escalating heat inputs. Part I: pool boiling.” *Int. J. Heat Mass Transf.*, 96, 667–684.

Sun, Y., Chen, G., Zhang, S., Tang, Y., Zeng, J. and Yuan, W. (2017). “Pool boiling performance and bubble dynamics on microgrooved surfaces with reentrant cavities.” *Appl. Thermal Eng*., 125, 432-442.

Teodori, E., Valente, T., Malavasi, I., Moita, A. S., Marengo, M. and Moreira, A. L. N. (2017). “Effect of extreme wetting scenarios on pool boiling conditions.” *Appl. Ther. Eng.*, 115, 1424-1437.

Wei, J. J. and Honda, H. (2003). “Effects of fin geometry on boiling heat transfer from silicon chips with micro-pin-fins immersed in FC-72.” *Int. J. Heat Mass Transf.*, 46, 4059-4070.

Xu, Z. G. and Zhao, C. Y. (2015). “Experimental study on pool boiling heat transfer in gradient metal foams.” *Int. J. Heat Mass Transf.*, 85, 824–829.

Yeom, H., Sridharan, K. and Corradini, M. L. (2015). “Bubble Dynamics in Pool Boiling on Nanoparticle Coated Surfaces.” *Heat Transfer Engineering*, 36 (12), 1013–1027.

Yu, C. K. and Lu, D. C. (2007). “Pool boiling heat transfer on horizontal rectangular fin array in saturated FC-72.” *Int. J. Heat Mass Transf.*, 50, 3624–3637.

Zeng, L. Z., Klausner, J. F. and Mei, R. (1993). “A unified model for the prediction of bubble detachment diameters in boiling systems-I Pool boiling.” *Int. J. Heat Mass Transf.*, 36 (9), 2261–2270.

Zhao, Y. H., Masuoka, T. and Tsuruta, T. (2002). “Unified theoretical prediction of fully developed nucleate boiling and critical heat flux based on a dynamic micro layer model.” *Int. J. Heat Mass Transf.*, 45, 3189-3197.

Zhao, Y. H., Masuoka, T. and Tsuruta, T. (2002). “Theoretical studies on transient pool boiling based on microlayer model.” *Int. J. Heat Mass Transf.*, 45, 4325–4331.

Zuber, N. (1959). “Hydrodynamic aspects of boiling heat transfer.” *AECU-4439*.

Zuber, N. (1963). “Nucleate boiling. The region of isolated bubbles and the similarity with natural convection.” *Int. J. Heat Mass Transf.*, 6 (1), 53–78.

APPENDIX A

UNCERTAINTY

Table A.1 Uncertainty values for heat flux, HTC and surface temperature of the test sample of R_a=4.03 μm at 10 bar pressure

Heat Flux (kW/m^2)	Heat Transfer Coefficient (kW/ m^{2}K)	Uncertainty in Heat Flux (%)	Uncertainty in Heat Transfer Coefficient (%)	Uncertainty in surface temperature (°C)
154.62	50.06	31.47	47.03	0.41
287.36	59.85	17.18	28.35	0.42
334.09	63.05	14.88	25.30	0.42
547.29	79.23	9.48	18.46	0.44
694.29	92.29	7.76	16.60	0.47
823.07	105.48	6.80	15.81	0.49
892.98	112.45	6.41	15.49	0.50
932.79	114.39	6.21	15.11	0.51
1022.60	121.33	5.84	14.65	0.53
1102.51	124.30	5.56	14.01	0.55
1202.41	131.27	5.28	13.64	0.57
1352.32	139.24	4.95	13.03	0.61
1458.03	145.15	4.77	12.73	0.64
1681.94	157.12	4.47	12.23	0.70
1911.85	172.09	4.26	12.09	0.76
2150.65	189.30	4.10	12.15	0.83
2313.20	195.39	4.01	11.97	0.88
2543.41	208.74	3.92	11.96	0.95
2775.96	219.83	3.84	11.95	1.02
2898.52	226.92	3.81	11.95	1.06

Table A.2 Uncertainty in the measurement of bubble departure diameter and bubble frequency for the sample of R_a=4.03 μm at 10 bar pressure

Jakob Number, *Ja*	**Bubble departure diameter, D_b (mm)**	**Bubble frequency, f (s^{-1})**	**Uncertainty in D_b (%)**	**Uncertainty in f (%)**
2.34368	0.62	63	6.912964	3.983025
2.97921	0.69	79	6.212362	4.727181
3.38643	0.76	85	5.642159	7.484121
4.08	0.89	101	4.818956	8.109665

APPENDIX B

POOL BOILING HEAT TRANSFER FROM ROUGH SURFACE AND MICROCHANNEL GEOMETRY

B.1 VALIDATION OF EXPERIMENTAL RESULTS

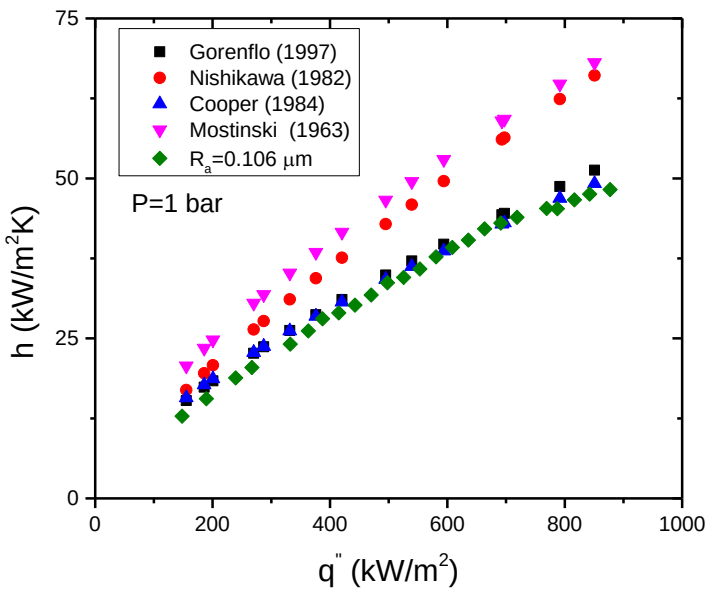

Figure B.1(a) Validation of experimental results of R_a=0.106 μm at P=1 bar

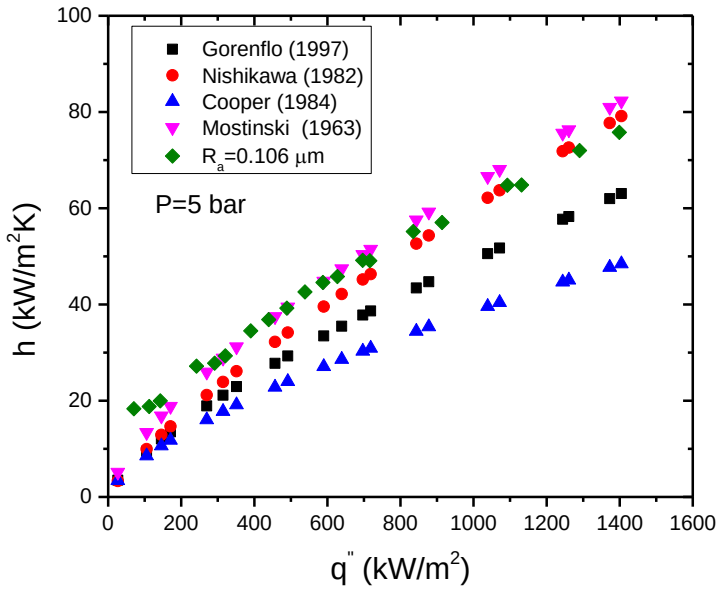

Figure B.1(b) Validation of experimental results of R_a=0.106 μm at P=5 bar

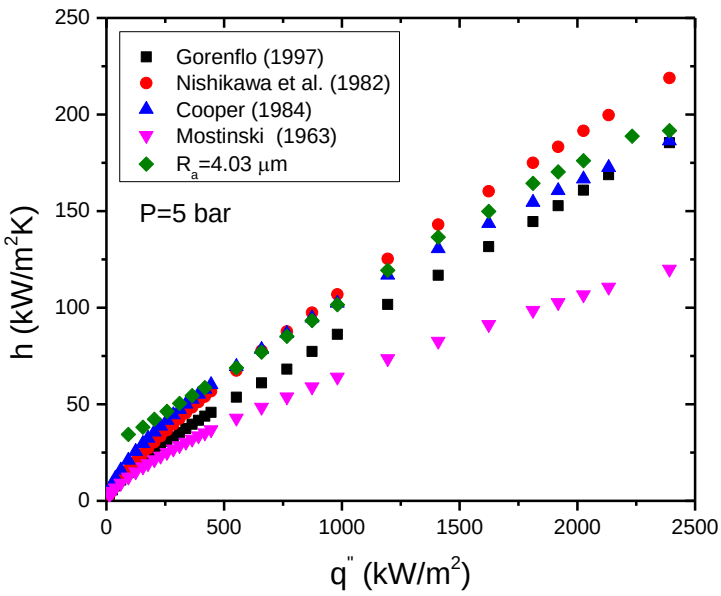

Figure B. 1(c) Validation of experimental results of R_a=4.03 μm at P=5 bar

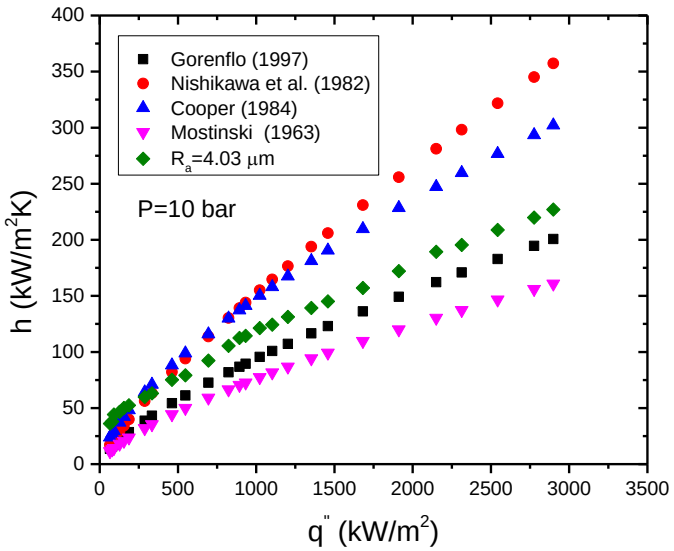

Figure B. 1(d) Validation of experimental results of 4.03 μm at P=10 bar

B.2 POOL BOILING CURVE FOR ROUGH SURFACE AND MICROCHANNEL GEOMETRY

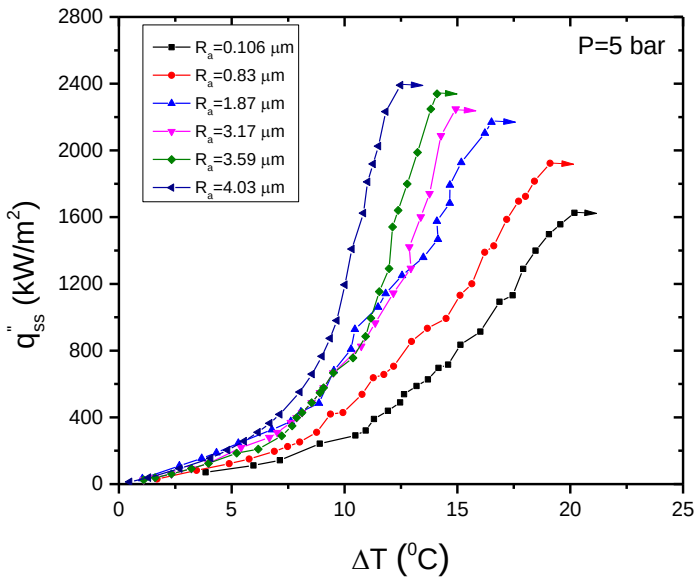

Figure B.2(a) Effect of surface roughness on pool boiling heat transfer during steady-state heat supply at 5 bar pressure

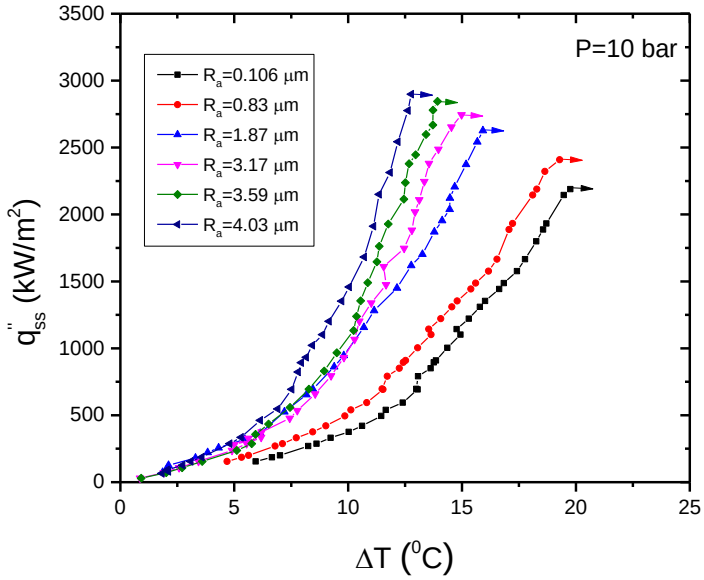

Figure B. 2(b) Effect of surface roughness on pool boiling heat transfer during steady-state heat supply at 10 bar pressure

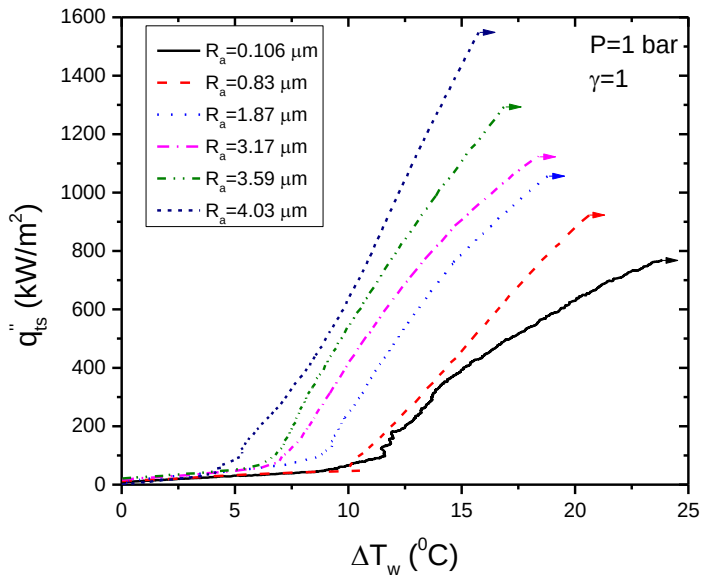

Figure B.3(a) Effect of surface roughness on pool boiling heat transfer during exponential heat supply at P=1, γ=1

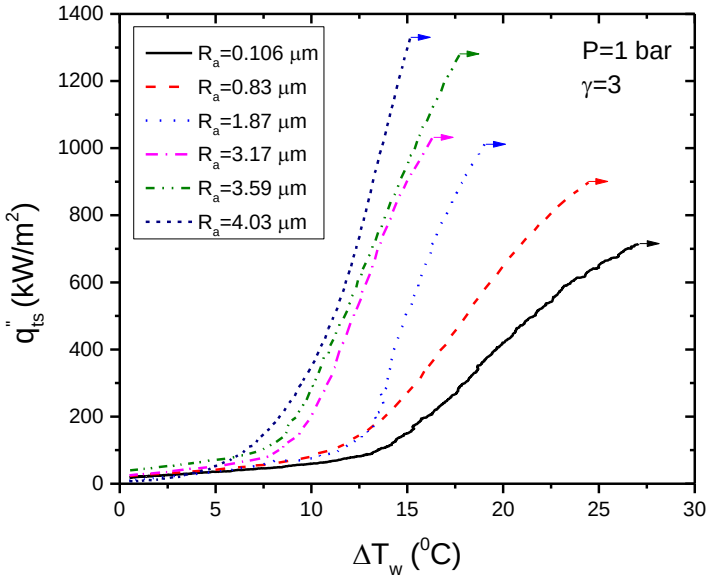

Figure B. 3(b) Effect of surface roughness on pool boiling heat transfer during exponential heat supply at P=1, γ=3

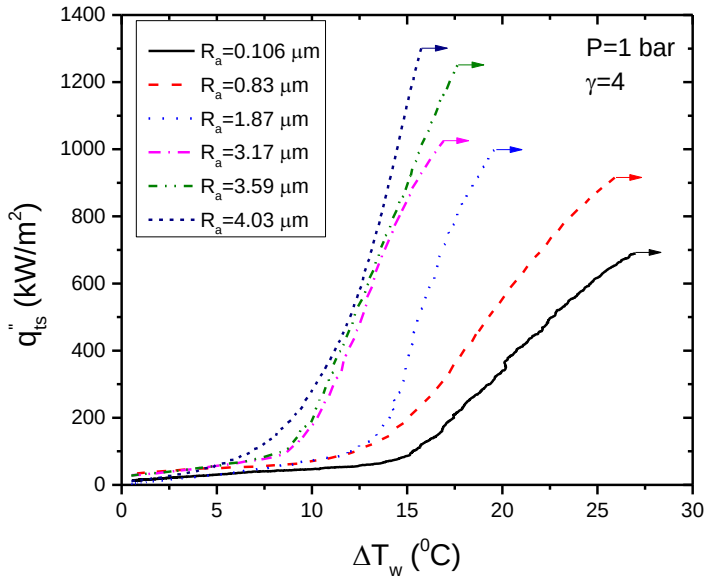

Figure B. 3(c) Effect of surface roughness on pool boiling heat transfer during exponential heat supply at P=1, γ=4

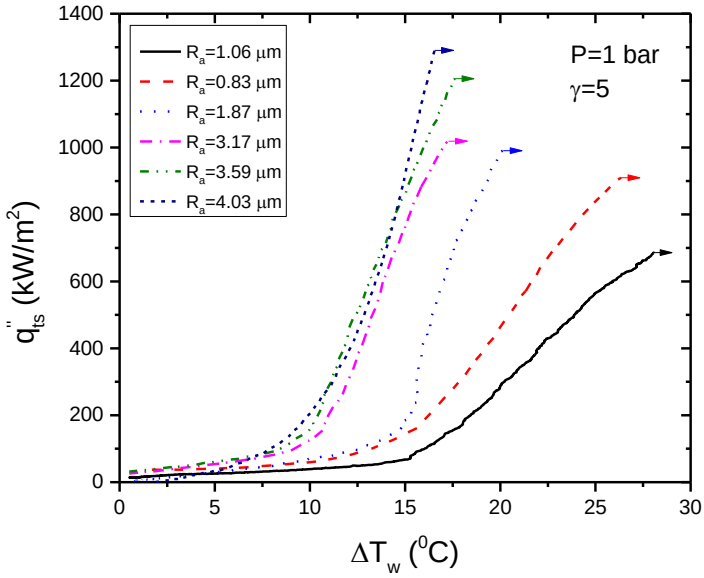

Figure B. 3(d) Effect of surface roughness on pool boiling heat transfer during exponential heat supply at P=1, γ=5

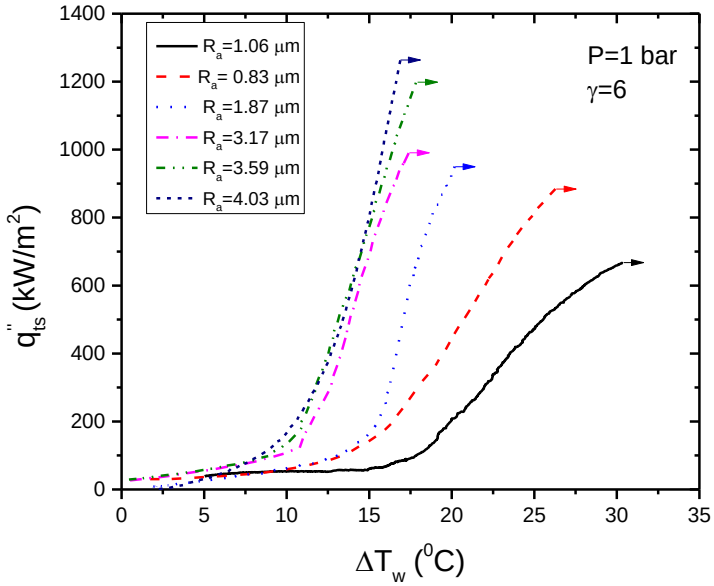

Figure B. 3(e) Effect of surface roughness on pool boiling heat transfer during exponential heat supply at P=1, γ=6

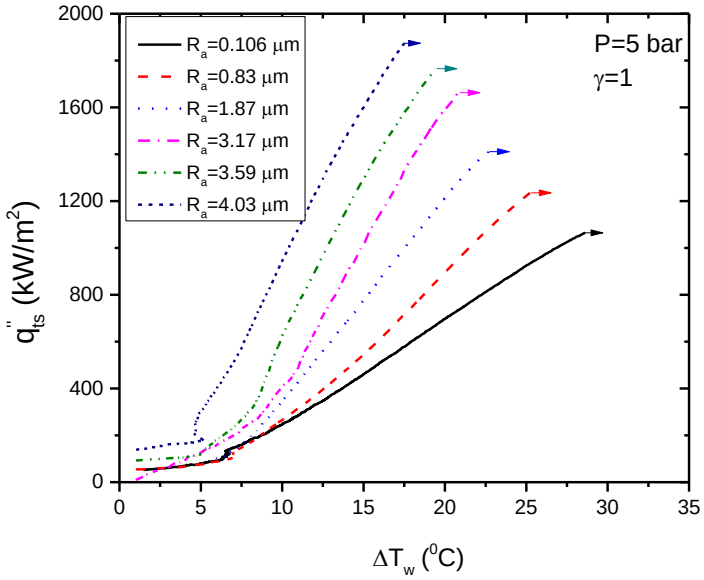

Figure B. 3(f) Effect of surface roughness on pool boiling heat transfer during exponential heat supply at P=5, γ=1

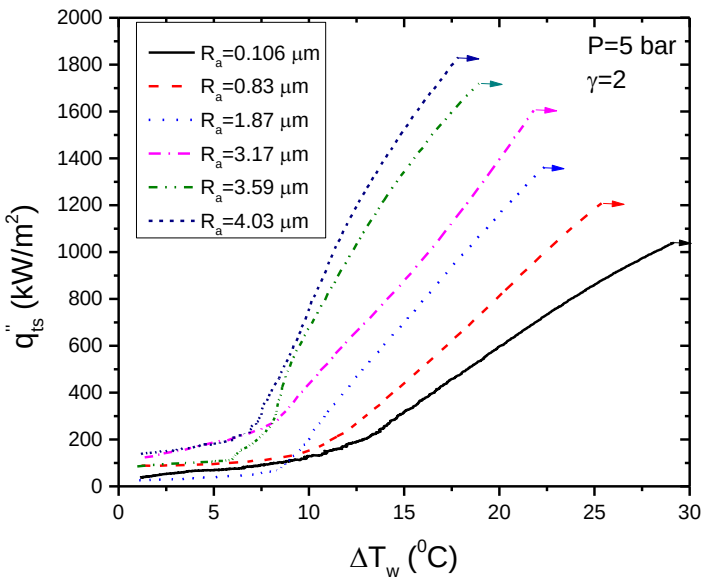

Figure B. 3(g) Effect of surface roughness on pool boiling heat transfer during exponential heat supply at P=5, γ=2

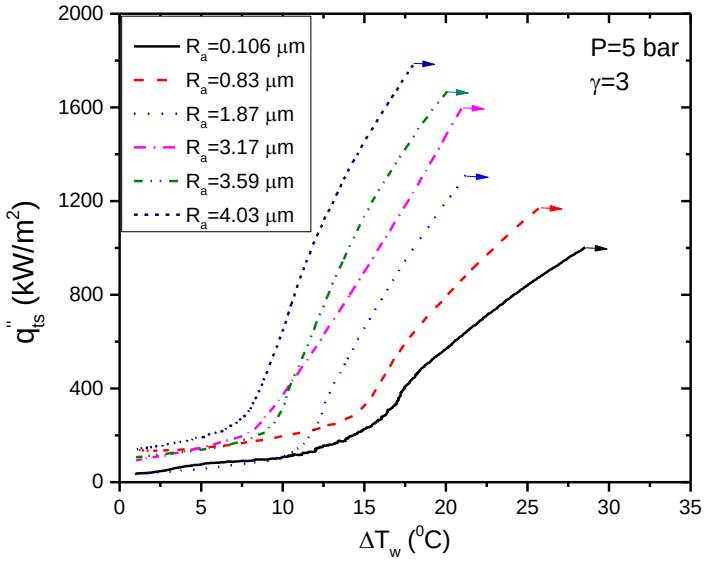

Figure B. 3(h) Effect of surface roughness on pool boiling heat transfer during exponential heat supply at P=5, γ=3

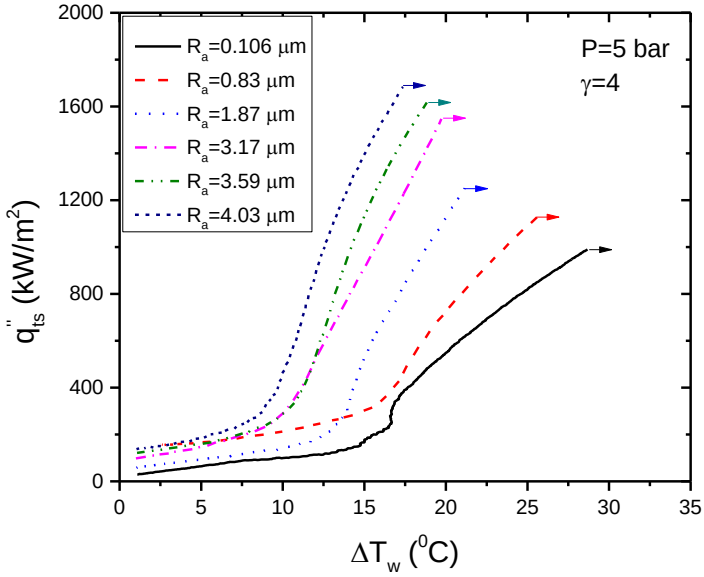

Figure B. 3(i) Effect of surface roughness on pool boiling heat transfer during exponential heat supply at P=5, γ=4

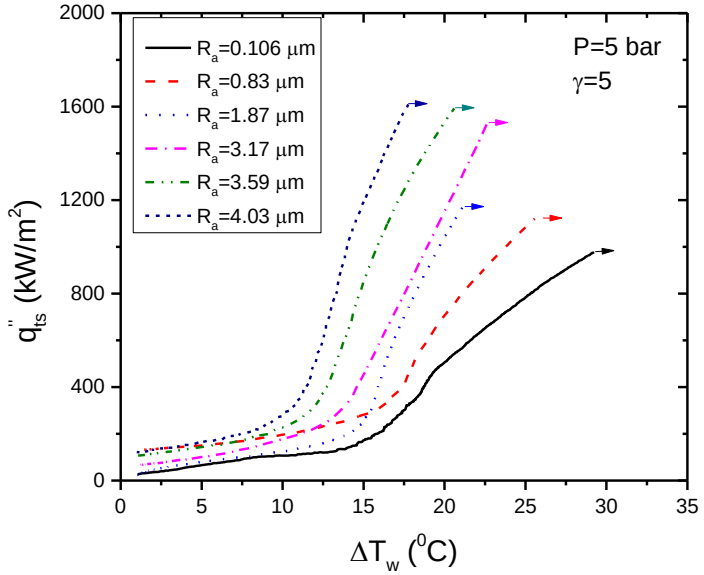

Figure B. 3(j) Effect of surface roughness on pool boiling heat transfer during exponential heat supply at P=5, γ=5

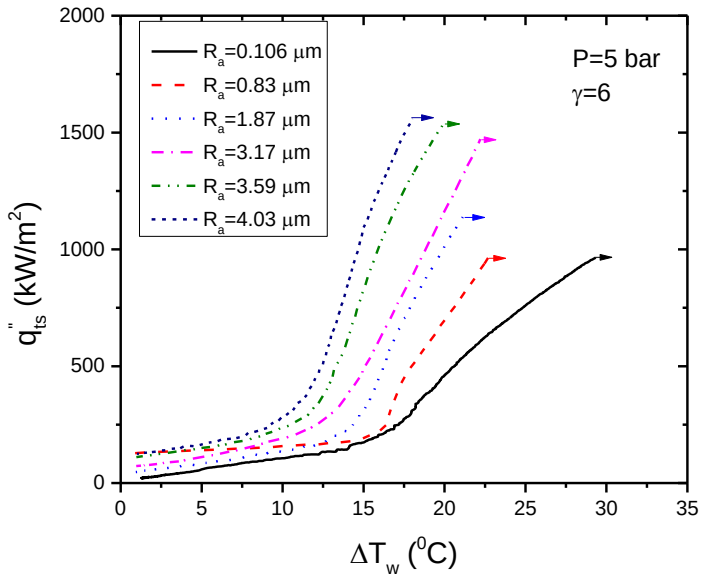

Figure B. 3(k) Effect of surface roughness on pool boiling heat transfer during exponential heat supply at P=5, γ=6

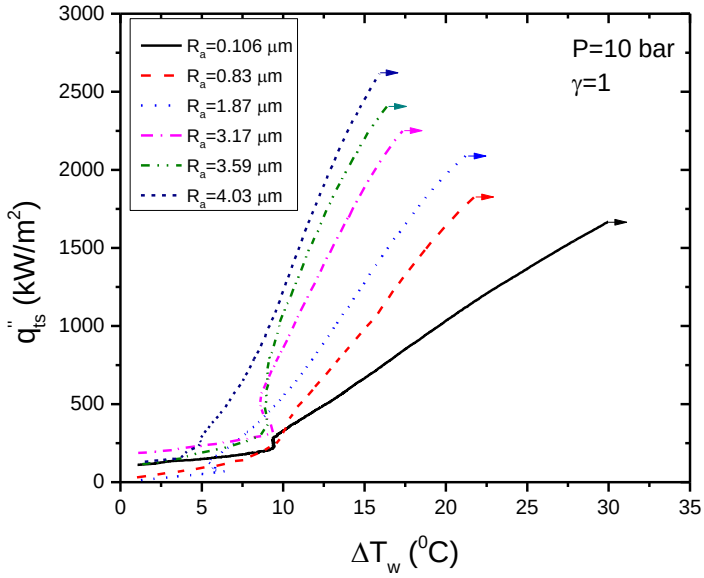

Figure B. 3(l) Effect of surface roughness on pool boiling heat transfer during exponential heat supply at P=10, γ=1

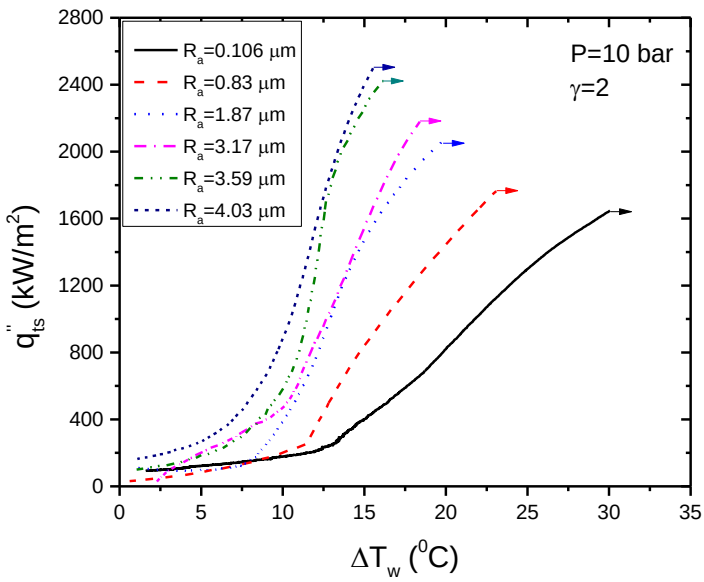

Figure B. 3(m) Effect of surface roughness on pool boiling heat transfer during exponential heat supply at P=10, γ=2

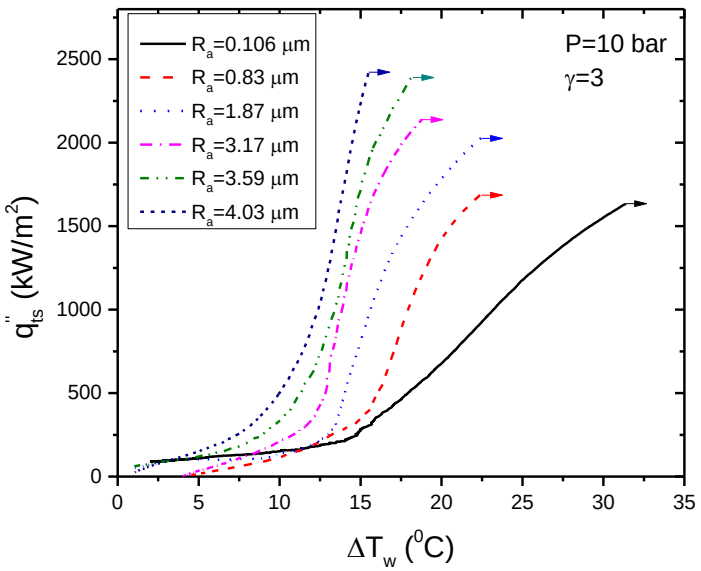

Figure B. 3(n) Effect of surface roughness on pool boiling heat transfer during exponential heat supply at P=10, γ=3

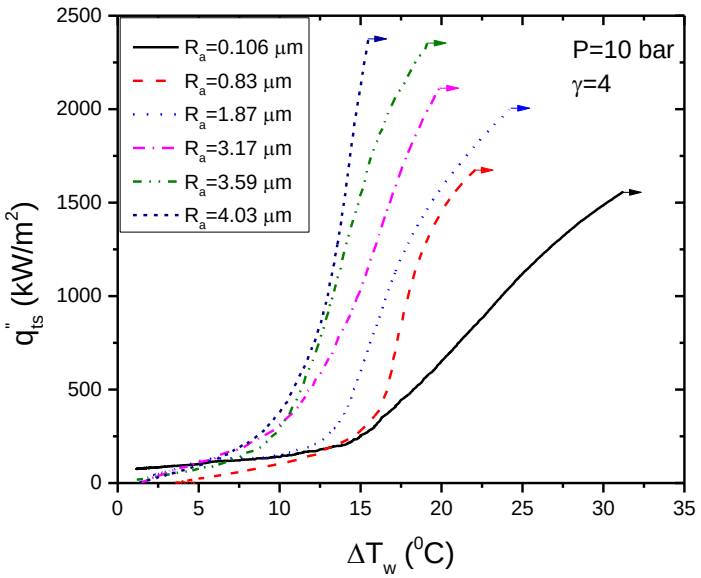

Figure B. 3(o) Effect of surface roughness on pool boiling heat transfer during exponential heat supply at P=10, γ=4

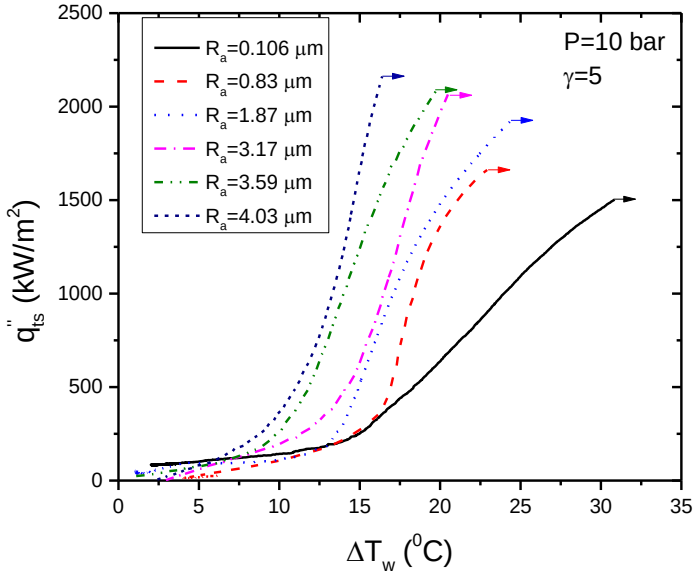

Figure B. 3(p) Effect of surface roughness on pool boiling heat transfer during exponential heat supply at P=10, γ=5

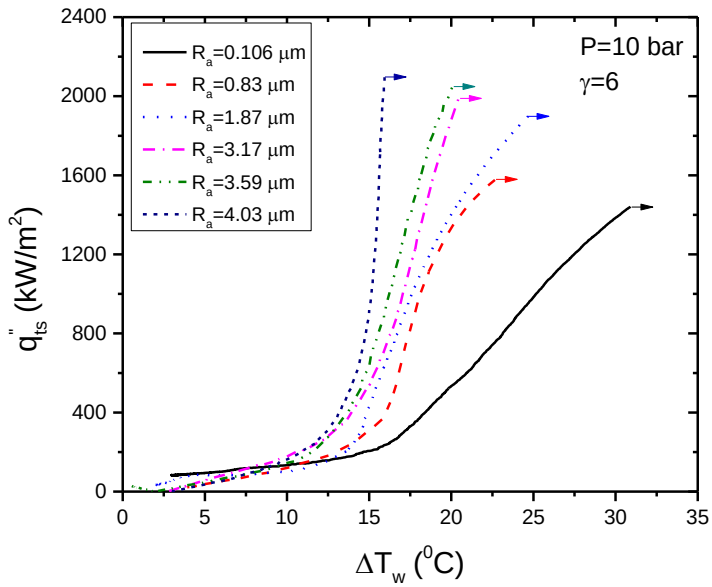

Figure B. 3(q) Effect of surface roughness on pool boiling heat transfer during exponential heat supply at P=10, γ=6

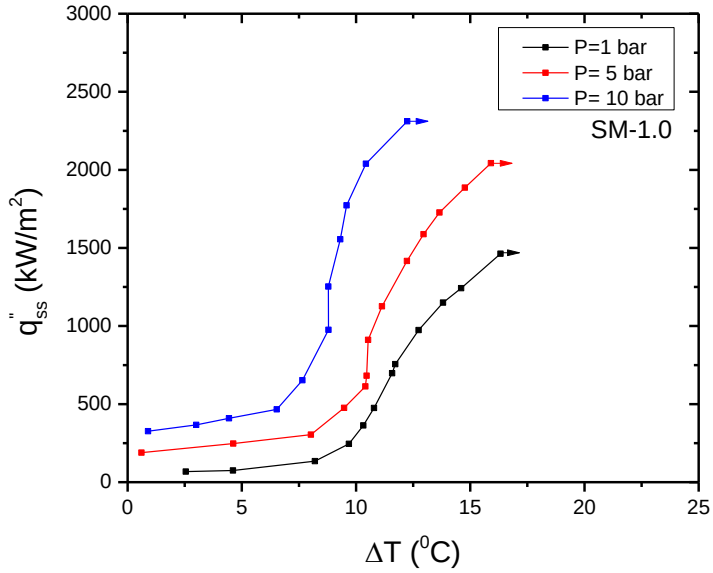

Figure B.4(a) Effect of pressure on pool boiling heat transfer from square microchannel during steady-state heat supply

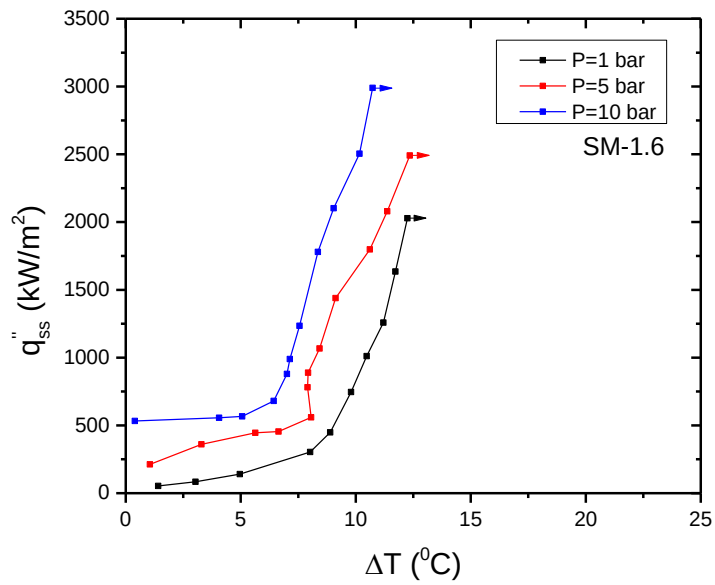

Figure B. 4(b) Effect of pressure on pool boiling heat transfer from stepped microchannel during steady-state heat supply

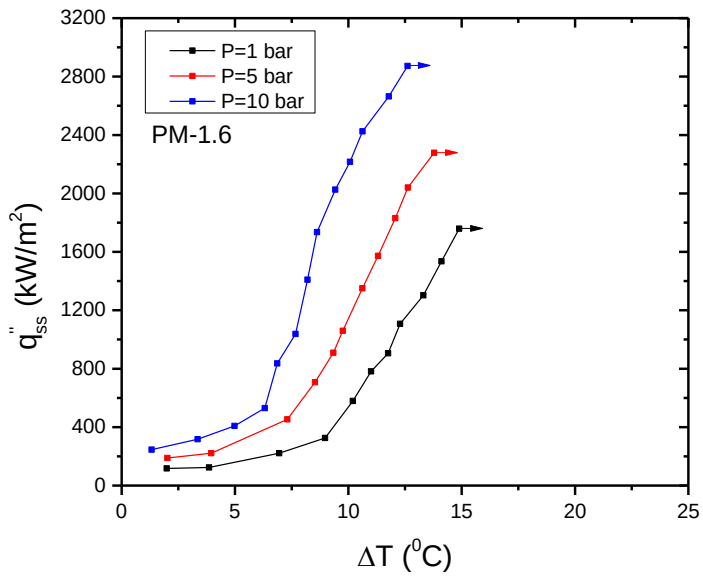

Figure B. 4(c) Effect of pressure on pool boiling heat transfer from parabolic microchannel during steady-state heat supply

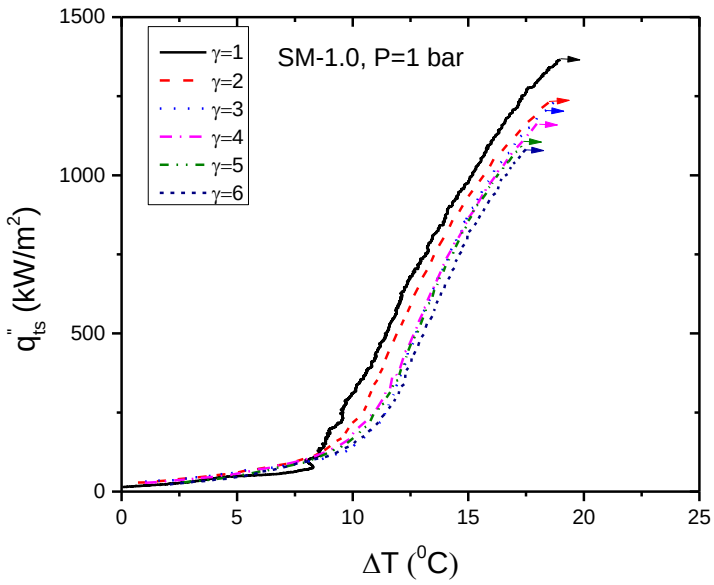

Figure B.5(a) Effect of time constant on pool boiling heat transfer from square microchannel during exponential heat supply at P=1 bar

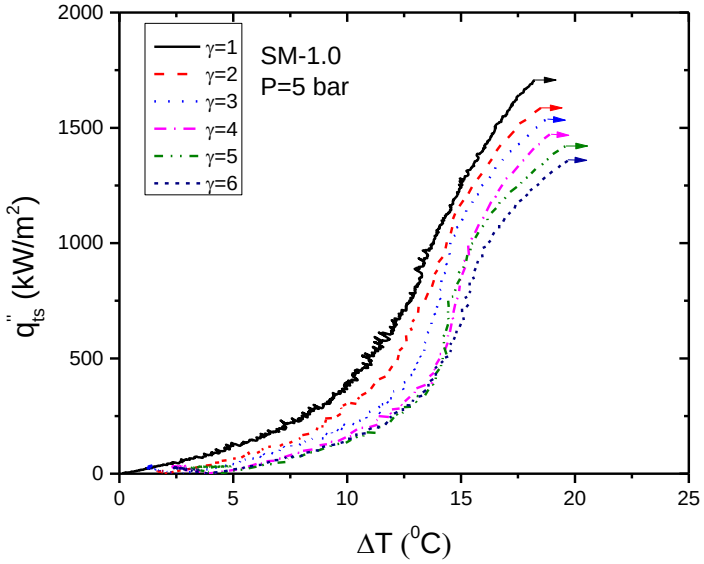

Figure B. 5(b) Effect of time constant on pool boiling heat transfer from square microchannel during exponential heat supply at P=5 bar

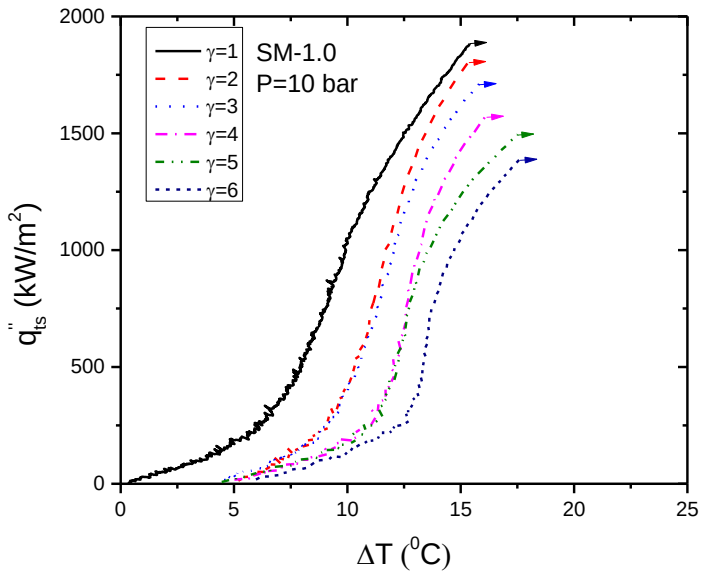

Figure B. 5(c) Effect of time constant on pool boiling heat transfer from square microchannel during exponential heat supply at P=10 bar

B.3 TRANSIENT POOL BOILING HEAT TRANSFER COEFFICIENT FOR ROUGH SURFACE

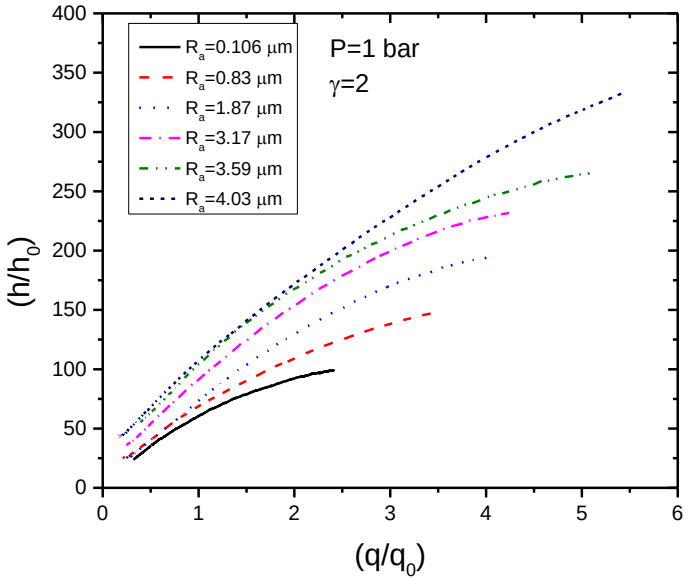

Figure B.6(a) Variation in non-dimensional h_{ts} with non-dimensional q_{ts} for different surface roughness at P=1 bar, γ=2

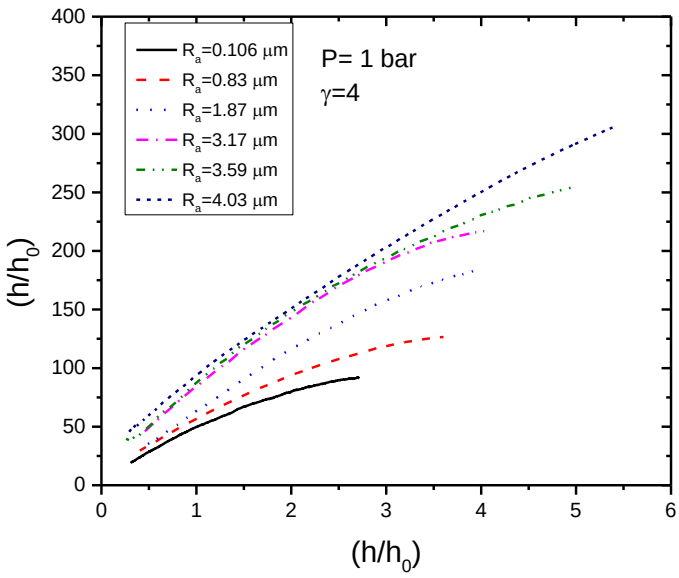

Figure B. 6(b) Variation in non-dimensional h_{ts} with non-dimensional q_{ts} for different surface roughness at P=1 bar, γ=4

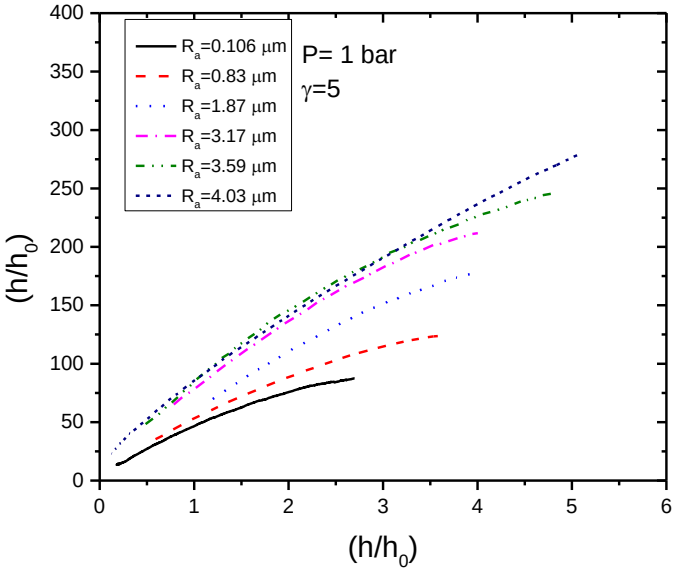

Figure B.6(c) Variation in non-dimensional h_{ts} with non-dimensional q_{ts} for different surface roughness at P=1 bar, γ=5

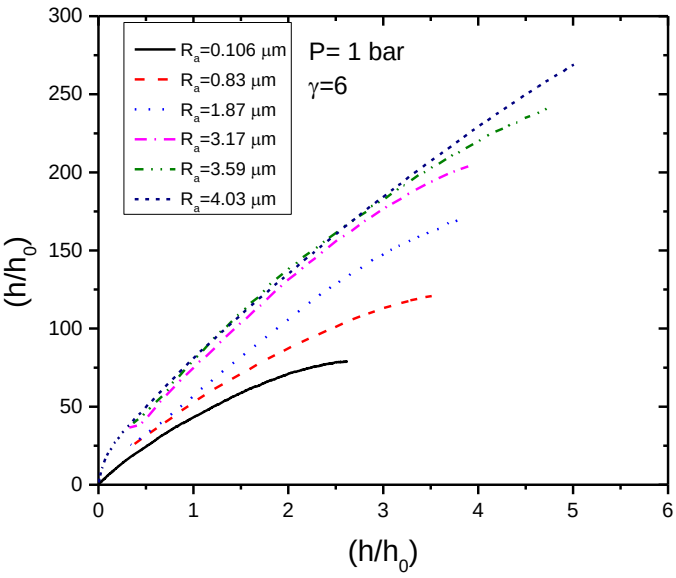

Figure B. 6(d) Variation in non-dimensional h_{ts} with non-dimensional q_{ts} for different surface roughness at P=1 bar, γ=6

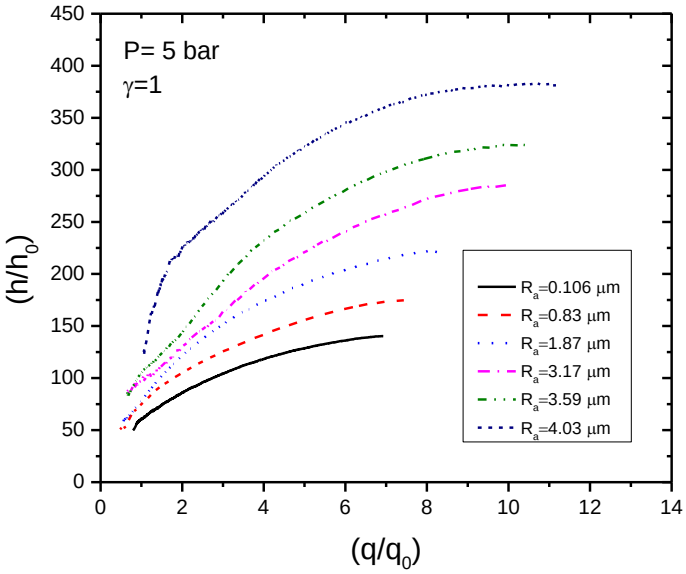

Figure B. 6(e) Variation in non-dimensional h_{ts} with non-dimensional q_{ts} for different surface roughness at P=5 bar, γ=1

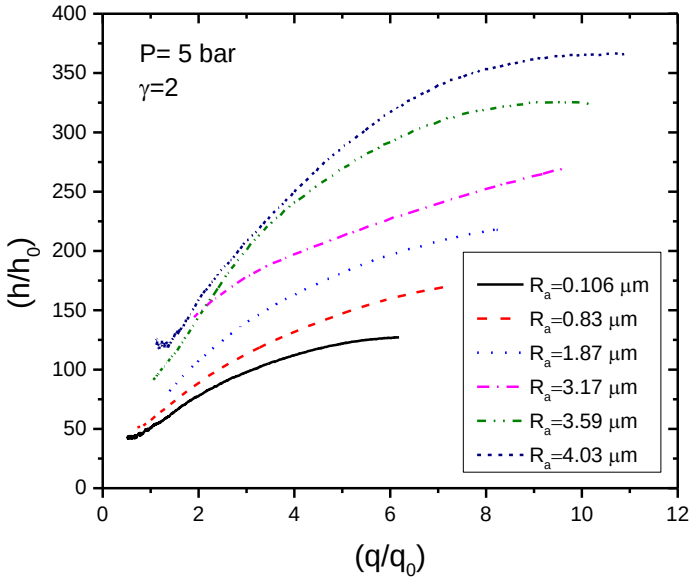

Figure B. 6(f) Variation in non-dimensional h_{ts} with non-dimensional q_{ts} for different surface roughness at P=5 bar, γ=2

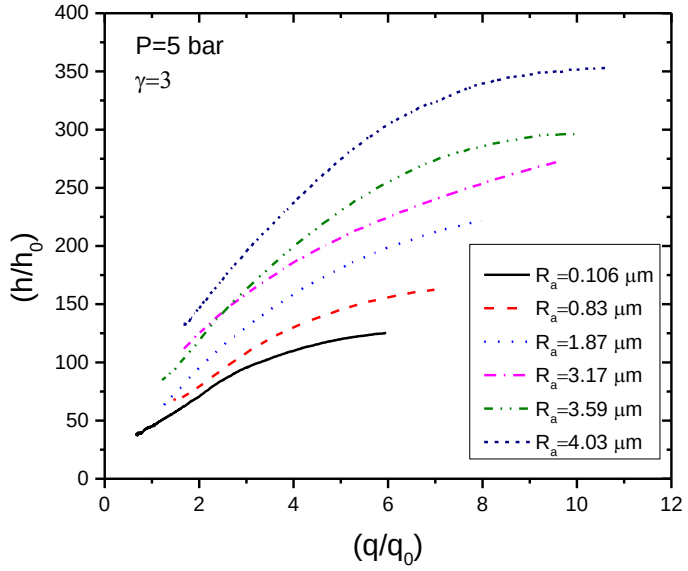

Figure B. 6(g) Variation in non-dimensional h_{ts} with non-dimensional q_{ts} for different surface roughness at P=5 bar, γ=3

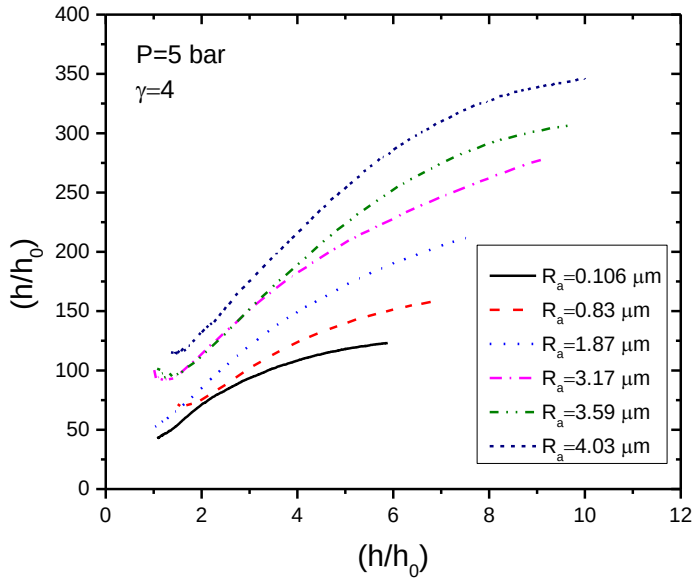

Figure B. 6(h) Variation in non-dimensional h_{ts} with non-dimensional q_{ts} for different surface roughness at P=5 bar, γ=4

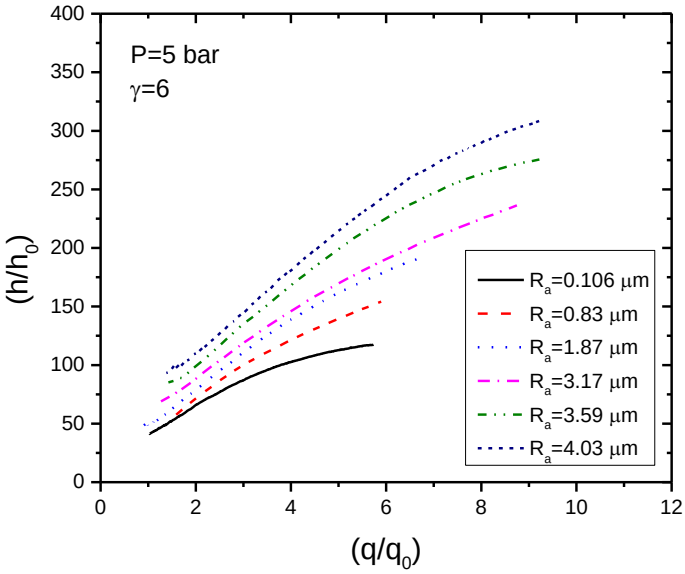

Figure B. 6(i) Variation in non-dimensional h_{ts} with non-dimensional q_{ts} for different surface roughness at P=5 bar, γ=6

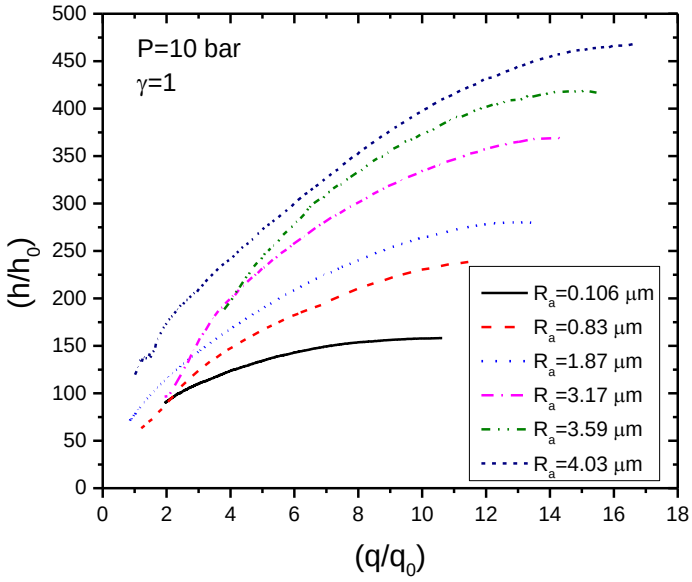

Figure B. 6(j) Variation in non-dimensional h_{ts} with non-dimensional q_{ts} for different surface roughness at P=10 bar, γ=1

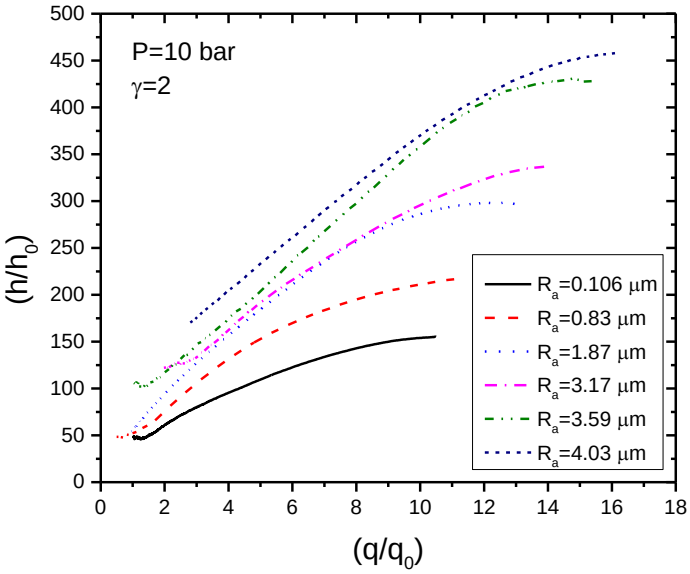

Figure B. 6(k) Variation in non-dimensional h_{ts} with non-dimensional q_{ts} for different surface roughness at P=10 bar, γ=2

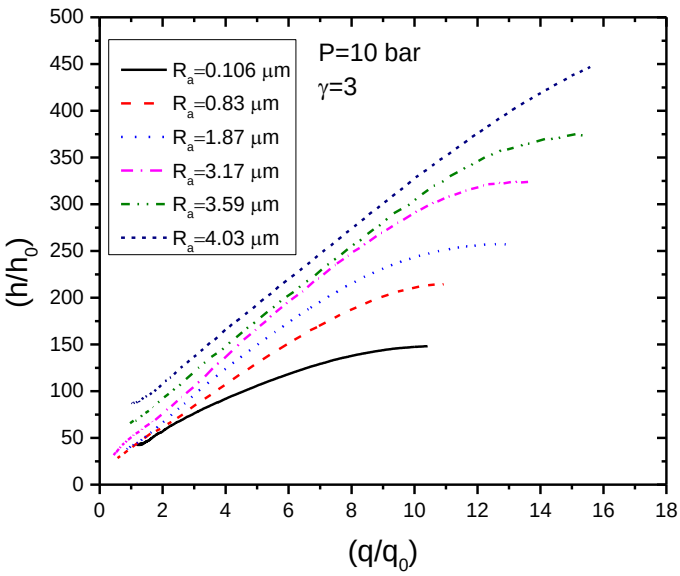

Figure B. 6(l) Variation in non-dimensional h_{ts} with non-dimensional q_{ts} for different surface roughness at P=10 bar, γ=3

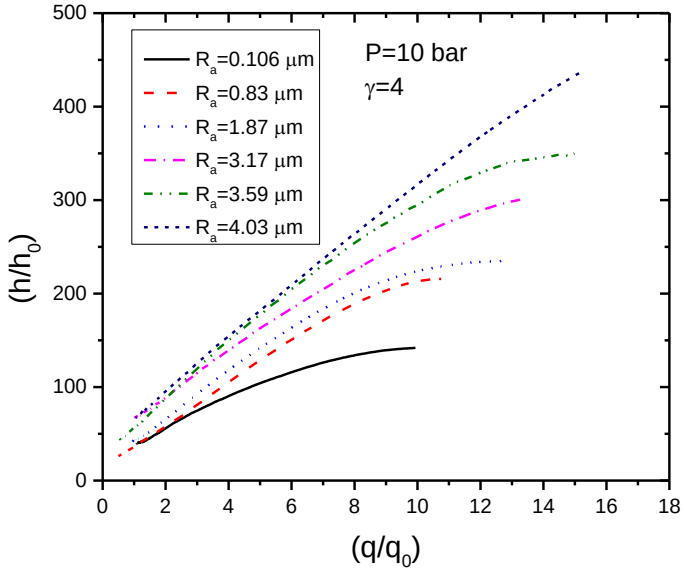

Figure B. 6(m) Variation in non-dimensional h_{ts} with non-dimensional q_{ts} for different surface roughness at P=10 bar, γ=4

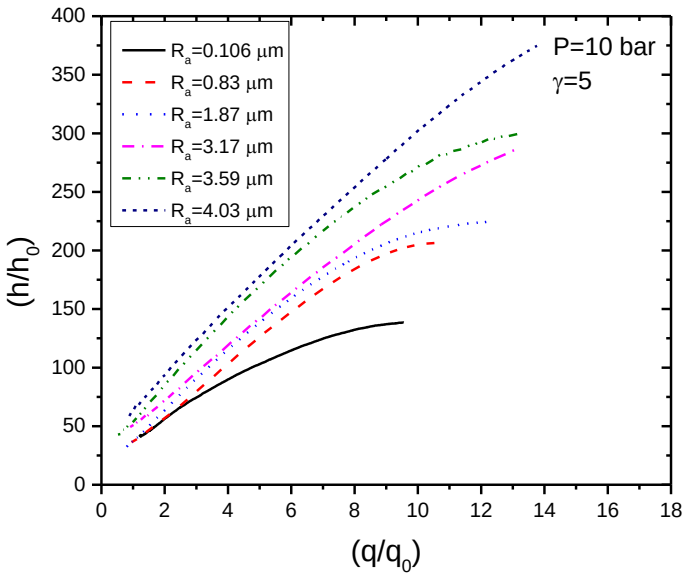

Figure B. 6(n) Variation in non-dimensional h_{ts} with non-dimensional q_{ts} for different surface roughness at P=1 bar, γ=4

B.4 TRANSIENT CRITICAL HEAT FLUX

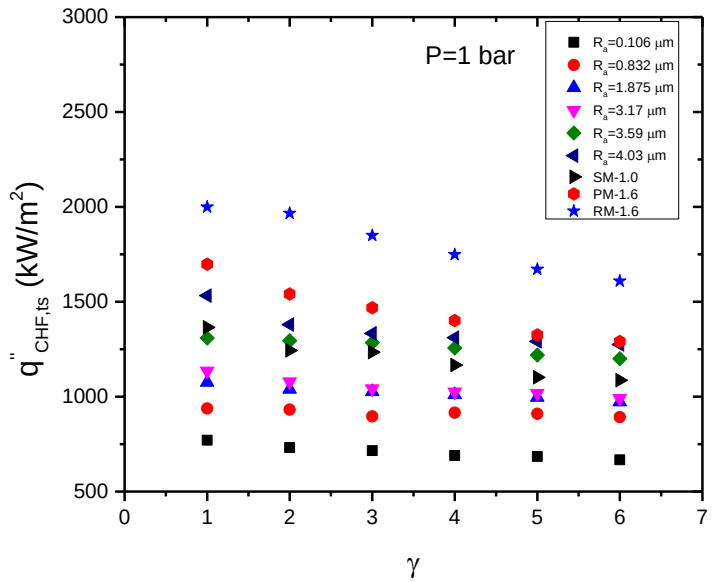

Figure B. 7(a) Effect of time constant on transient CHF of rough and microchannel geometries at 1 bar pressure

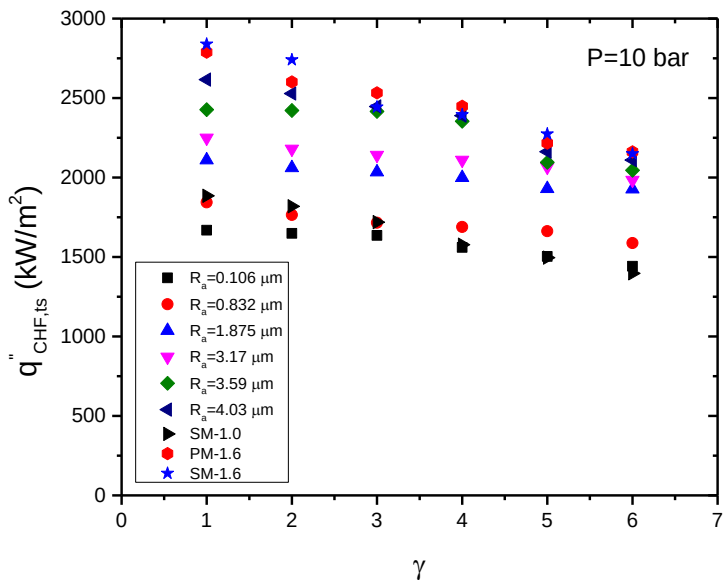

Figure B. 7(b) Effect of time constant on transient CHF of rough and microchannel geometries at 10 bar pressure

PUBLICATION

Journal

- Avdhoot Walunj, A. Sathyabhama. (2016). "Dynamic Pool Boiling Heat Transfer Due to Exponentially Increasing Heat Input-A Review." *Procedia Technology*, 25, 1137–1145.
- Avdhoot Walunj, A. Sathyabhama. (2018). "Comparative Study of Pool Boiling Heat Transfer from Various Microchannel Geometries." *Applied Thermal Engineering*, 128, 672–683.
- Avdhoot Walunj, A. Sathyabhama. (2018). "Transient CHF enhancement in high pressure pool boiling on rough surface." *Chemical Engineering Processing*, 127, 145–158.
- Avdhoot Walunj, A. Sathyabhama. (2018). "Bubble Dynamics and Enhanced Heat Transfer during High Pressure Pool Boiling on Rough Surface." *Journal of Thermophysics and Heat transfer*, 33, 1-13.
- Avdhoot Walunj, A. Sathyabhama. (2018). "Influence of Surface Roughness on Pool Boiling Heat Transfer." *Materials Science and Engineering*, 402, 1-11.
- Avdhoot Walunj, A. Sathyabhama, Effect of Surface Roughness on Pool Boiling Heat Transfer Due To Exponential Step Heat Input, *Jr. of Enhanced Heat Transfer*. (Revision submitted)
- Avdhoot Walunj, A. Sathyabhama. "A CHF Model for Pool Boiling on Rough Surface under Exponential Heat Supply." *Thermal Science and Engineering Progress* (Under review).
- Avdhoot Walunj, A. Sathyabhama. "Experimental Investigation on Transient Pool Boiling Heat Transfer from Rough Surface and Heat Transfer Correlations." *Jr. of Heat and Technology* (Under review).

Conference

- Avdhoot Walunj, A. Sathyabhama, Effect of Surface Roughness on Pool Boiling Heat Transfer Due To Exponential Step Heat Input, 24th National and 2nd International ISHMT-ASTFE Heat and Mass Transfer Conference (IHMTC-2017).
- Avdhoot Walunj, A. Sathyabhama, Transient Pool Boiling Heat Transfer Due To Exponential Step Heat Input, 24th National and 2nd International ISHMT-ASTFE Heat and Mass Transfer Conference (IHMTC-2017).
- Avdhoot Walunj, A. Sathyabhama, Bubble Dynamics in Pool Boiling on Rough Surface Under Exponential Heat Supply, Proceeding of 3rd Thermal and Fluids Engineering Conference (TFEC), TFEC-2018-21676, 329-337.
- Avdhoot Walunj, A. Sathyabhama, Influence of Surface Roughness on Pool Boiling Heat Transfer, 2nd International Conference on Advances in Mechanical Engineering at S.R.M. Institute of Science and Tech., Chennai.
- Avdhoot Walunj, A. Sathyabhama, Effect of Surface Roughness on Pool Boiling Characteristics under Variable Heat Supply, 12th International Conference on Thermal Engineering: Theory and Applications, PDPU, Gandhinagar. (accepted)

BIO-DATA

	Mr. AVDHOOT ASHOK WALUNJ	**Email:** aawalunj@gmail.com **Mob. No.:** 9403188542

❖ **Current Position:**
Assistant Professor of Mechanical Engineering, Dept. of Farm Machinery and Power Engineering, A. S. College of Agril. Engg. & Tech., Rahuri. (Govt. of Maharashtra)

EDUCATION				
Examination	**Board/University Institute**	**Year of Passing**	**Percentage/ SGPA**	**Grade**
M.E. (Heat Power)	Savitribai Phule Pune University	2014	7.58	First Class
B.E. (Mechanical)	Savitribai Phule Pune University	2012	65.5	First class
H.S.C.	Pune Board	2008	78.89	Distinction
S.S.C.	Pune Board	2006	87.2	Distinction

EXPERIENCE	
Assistant Professor	SRES College of Engineering, Kopargaon from 17th June,14 to 15th June, 2015.
ACADEMIC PROJECTS	
M.E.	Performance of Inclined Narrow Plate-fin Heat Sink under Free Convection Heat Transfer
B.E.	Experimental Analysis of Tribological Behaviour of TiCN, Tin and Hardchrome coatings.
COURSES TAUGHT	
	Basic Mechanical Engineering, Thermodynamics, Applied Thermodynamics, Heat Transfer

GRANT/AWARD
• First Prize for Best Student Mechanical Engineering Student Association (MESA) Activity, 2010. • Grant received through International Travel Support from Science and Engineering Research Board (SERB), DST, 2018.
PROGRAM/WORKSHOP/SEMINAR ATTENDED
• Nano composites Materials- A research Horizon at University of Pune • Bio-fluid Dynamics and Bio-heat Transfer at NITK, Surathkal. • Recent Advances and Challenges in Solar Thermal Systems at NITK, Surathkal. • Recent Trends in Solar and Wind Energy at MNIT, Bhopal. • Hands on exercise in COMSOL Multiphysics at Park Plaza Bangalore. • Transfer function based on GF to solve IHCP problem at NITK, Surathkal.
MEMBERSHIP
• Life member of 'Indian Society Technical Education' (ISTE). • Member of 'Indian Society For Heat And Mass Transfer' (ISHMT). • Member of 'International Association of Engineers (IAENG)', Hong Kong. • Member of 'International Association of Educators and Researchers' (IAER), UK.

SOFTWARE PROFICIENCY			
1	ANSYS 14.0	3	AutoCAD
2	COMSOL Solver	4	MATLAB

PERSONAL DETAILS	
Name	Mr. Walunj Avdhoot Ashok
Address	A/P: Pimpalgaon Konzira, Tal: Sangamner, Dist: A'nagar.
Date of Birth	2nd Dec.,1990
Gender	Male
Marital Status	Unmarried
Languages	English, Hindi, Marathi.
Blood Group	A +ve

Declaration: I hereby declared that information furnished above is true to best of my knowledge.

Date: 01/01/2019

Place: NITK Avdhoot Walunj